

**LOW VOLTAGE ACTUATION OF
ELECTROSTATIC
MICROELECTROMECHANICAL
SYSTEMS ACTUATORS USING
FERROELECTRIC NEGATIVE
CAPACITANCE**

A THESIS

submitted by

RAGHURAM TATTAMANGALAM RAMAN
(ROLL NO. 121704004)

for the

AWARD OF THE DEGREE

of

DOCTOR OF PHILOSOPHY



INDIAN INSTITUTE
OF TECHNOLOGY
PALAKKAD

Department of Electrical Engineering

August 2022

Raghuram Tattamangalam Raman: Low VOLTAGE ACTUATION OF ELECTROSTATIC
MICROELECTROMECHANICAL SYSTEMS ACTUATORS USING FERROELECTRIC NEGATIVE
CAPACITANCE

©Indian Institute of Technology Palakkad

August 2022

CERTIFICATE

This is to certify that the thesis titled **Low Voltage Actuation of Electrostatic Microelectromechanical Systems Actuators Using Ferroelectric Negative Capacitance**, submitted by *Raghuram Tattamangalam Raman (Roll No. 121704004)* for the award of the degree of *Doctor of Philosophy* of *Indian Institute of Technology Palakkad*, is a record of bonafide work carried out by him under my guidance and supervision at the *Department of Electrical Engineering, Indian Institute of Technology Palakkad*. To the best of my knowledge and belief, the work presented in this thesis is original and has not been submitted, either in part or full, for the award of any other degree, diploma, fellowship, associateship or similar title of any university or institution.



Dr. Arvind Ajoy

DECLARATION

I hereby declare that the work reported in this thesis is original and was carried out by me. Further, this thesis has not formed the basis, neither has it been submitted for the award of any degree, diploma, fellowship, associateship or similar title of any university or institution.

Palakkad,

August 2022



Raghuram Tattamangalam Raman

(Roll No. 121704004)

To my Appa (Father) Late T.E. Raman and Amma (Mother) N. Rajalakshmi.
No words will ever express how much you two mean to me. Thank you for
everything you have given to me.

ABSTRACT

Microelectromechanical Systems (MEMS) based on electrostatic actuation are an integral part of today's electronics. The electrostatic MEMS actuator, in its generic form, consists of a movable electrode and a fixed electrode, separated by an air-gap. An input voltage is applied between the movable and fixed electrodes. The actuator responds to the applied voltage by inducing a displacement in the movable electrode. These actuators offer several advantages such as low power consumption, low-cost, fast response and ease of fabrication. Electrostatic MEMS actuators, however, suffer from an instability called pull-in, wherein the movable electrode snaps onto the fixed electrode beyond a certain applied voltage. Moreover, these actuators demand high operating voltages. A novel idea proposed to mitigate this large voltage requirement is to employ a "hybrid actuator". This envisages a ferroelectric capacitor exhibiting negative capacitance, connected in series with the MEMS actuator.

In this thesis, we describe the modeling of the hybrid actuator using: (i) a SPICE (Simulation Program with Integrated Circuit Emphasis) based framework and (ii) an energy landscape based framework. Using the proposed frameworks, we depict the low-voltage operation of the hybrid actuator for both static and dynamic (step) inputs. We predict a reduction in the energy consumption during dynamic pull-in in the hybrid actuator as compared to the standalone actuator, even in the presence of damping. Our framework also allows straightforward inclusion of adhesion between the contacting surfaces. Using the proposed frameworks, we show that the pull-in voltage is unaffected and the pull-out voltage is reduced in the hybrid actuator, due to adhesion.

The pull-in instability restricts the maximum distance traveled by the movable electrode before it is pulled-in, to a fraction of the air-gap. In this thesis, we propose the elimination of pull-in instability accompanied by low-voltage operation, in the

hybrid actuator by adding a non-linear spring (with cubic non-linearity) to it. Based on the value of the cubic spring constant, we show that the hybrid actuator can work in three distinct modes: (i) monostable (ii) bistable and (iii) always-stable. We also estimate the threshold values of the cubic spring constant that demarcate the aforementioned modes. We show that the pull-in free and low-voltage operation can be achieved when the hybrid actuator operates in the always-stable mode.

The proposed modeling frameworks can aid in the design and analysis of negative capacitance based low-voltage electrostatic MEMS actuators.

Keywords: Electrostatic MEMS actuators, ferroelectric negative capacitance, SPICE modeling, energy landscape, pull-in, travel range extension

PUBLICATIONS

JOURNAL

- [1] Raghuram Tattamangalam Raman, Arvind Ajoy, and Revathy Padmanabhan. "Analysis of Electrostatic MEMS Using Energy-Charge Landscape." In: *IEEE Trans. Electron Devices* 67.10 (2020), pp. 4413–4420. DOI: [10.1109/TED.2020.3018700](https://doi.org/10.1109/TED.2020.3018700).
- [2] Raghuram Tattamangalam Raman and Arvind Ajoy. "SPICE-Based Multiphysics Model to Analyze the Dynamics of Ferroelectric Negative-Capacitance - Electrostatic MEMS Hybrid Actuators." In: *IEEE Trans. Electron Devices* 67.11 (2020), pp. 5174–5181. DOI: [10.1109/TED.2020.3019991](https://doi.org/10.1109/TED.2020.3019991).
- [3] Raghuram Tattamangalam Raman, Jeffin Shibu, Revathy Padmanabhan, and Arvind Ajoy. "Analysis of Ferroelectric Negative Capacitance-Hybrid MEMS Actuator Using Energy-Displacement Landscape." In: *IEEE Trans. Electron Devices* 69.6 (2022), pp. 3359–3366. DOI: [10.1109/TED.2022.3164633](https://doi.org/10.1109/TED.2022.3164633).
- [4] Raghuram Tattamangalam Raman, Revathy Padmanabhan, and Arvind Ajoy. "Stable Deflection in Ferroelectric Negative-Capacitance Hybrid MEMS Actuator with Cubic Non-Linear Spring." In: *IEEE Trans. Electron Devices* 69.9 (2022), pp. 5162–5169. DOI: [10.1109/TED.2022.3190258](https://doi.org/10.1109/TED.2022.3190258).

CONFERENCE

- [1] Raghuram Tattamangalam Raman, Arvind Ajoy, and Revathy Padmanabhan. "Analysis of Ferroelectric Negative Capacitance - Hybrid MEMS Actuator Using Energy Landscape." In: *Virtual MRS (Materials Research*

Society) Spring Meeting & Exhibit. 2021, pp. 497–498. URL: <https://www.mrs.org/docs/default-source/meetings-events/spring-meetings/2021/abstract-book.pdf>.

PATENT

- [1] Raghuram Tattamangalam Raman, Revathy Padmanabhan, and Arvind Ajoy. "Method of Eliminating Pull-in Instability and Hybrid MEMS Actuator Incorporating the Method." Pat. 398690. Patent granted by the Indian Patent Office on 07 Jun. 2022.

ACKNOWLEDGMENTS

This thesis in its final form would not have been possible but for the indulgent and kind hearted help from numerous experts and excellent research facilities at Indian Institute of Technology Palakkad. I would like to take this opportunity to thank everyone who has helped me in realizing this thesis and also those who have helped in shaping me professionally and personally.

Firstly, I would like to express my sincere gratitude to my Ph.D. advisor, Dr. Arvind Ajoy, Associate Professor, Department of Electrical Engineering, Indian Institute of Technology Palakkad, for accepting me as his student and for giving me an opportunity to do Ph.D. with him. I sincerely thank him for his constant guidance, support and encouragement throughout the years. He has been a great source of inspiration to me. I have learnt a lot from him, starting from his ability to choose a research problem, to explore new paths and ideas and to remain undaunted by failures. Dr. Arvind has been an excellent mentor in all respects, allowing me to thoroughly enjoy my research journey at Indian Institute of Technology Palakkad. I am deeply inspired by his motto of having fun through academic activities, experiments and research pursuits and it is something that I look up to, in my future endeavors.

I also take this opportunity to thank my collaborator, Dr. Revathy Padmanabhan, Assistant Professor, Department of Electrical Engineering, Indian Institute of Technology Palakkad for her help and support. I thank her for the absorbing technical discussions, joint publications and numerous feedbacks on my works. I sincerely thank her for helping me in identifying a graphical approach to understand the behavior of MEMS actuators.

I am also thankful to the members of my Doctoral Committee for their support. I thank the Chairman, Dr. Sreenath V. and the members of the committee, Dr. Arvind Ajoy, Dr. Revathy Padmanabhan, Dr. Swaroop Sahoo and Dr. Debarati Chatterjee

from Indian Institute of Technology Palakkad and Prof. S. Kasiviswanathan from Indian Institute of Technology Madras, for their useful comments and suggestions that helped me to improve my work. I also thank Prof. K. L. Sebastian, former Dean Research at Indian Institute of Technology Palakkad, for his valuable suggestions during his tenure at the institution. I thank Prof. Sebastian for motivating me to learn and use Mathematica as a tool for the analytical calculations.

Throughout the years, I was fortunate to get opportunities to present my work in front of various experts and receive their valuable feedback. I thank Prof. G. K. Ananthasuresh and Prof. Navakanta Bhat from Indian Institute of Science, Bangalore and Prof. Deleep R Nair, Prof. S. Karmalkar and Prof. Amitava Das-Gupta from Indian Institute of Technology Madras for their useful comments and suggestions. My sincere thanks to Prof. Ananthasuresh who was kind enough to interact with me over email during my initial days of research and share his code on the dynamic response of MEMS actuators, that helped me to understand the concept. I also thank Dr. Sukomal Dey and Dr. Subrahmanyam Mula, Indian Institute of Technology Palakkad, for their suggestions on my work.

I thank Dr. Sovan Lal Das, Dean, Academics and Dr. Uma Divakaran, Associate Dean, Academics Post-graduate, for their help with the coordination of various activities related to research. I also thank the administrative staff Mr. Arun Krishnan and Ms. Darsana Nair V. for their help. I thank Mr. Biju K. V., Technical Officer and Mr. Sumesh K. S., Junior Technical Superintendent, for their help with the installation of different software tools that enabled uninterrupted work, especially, working from home, during the Covid-19 pandemic times.

The best part of working at Indian Institute of Technology Palakkad is that you enjoy the company of so many talented undergraduate students and research scholars. I thank Jeffin Shibu, final year undergraduate student, Department of Electrical Engineering, Indian Institute of Technology Palakkad for his collaboration and help. I am extremely thankful to him for the numerous discussions we have had on different topics related to my research. I also thank my department colleagues Rekha S. S., Renjith S., Anuja M., Mejo A. J., Ananthu S., Kumudini G., Sreejyothi S., Madhav Ramesh, Priyankka G. R., and former colleague Prasanna

Venkatesan R., for their useful suggestions during my presentations at the journal club meetings. I also thank my colleague Diljith T. and former colleague Sachin Krishnan T. V., for helping me out with the basics of Linux commands and LaTeX. I also thank Siji S. S., for helping me with the operation of my computer system when I was working from home. I express my thanks to my dear friends Deepu Benson, Sreejith K. P., Benzy V. K., for the engaging discussions at the cafeteria on a plethora of topics and for sharing the light-hearted moments during the course of my research.

I thank the Indian Institute of Technology Palakkad for providing me the necessary facilities to carry out my research. I also thank the Ministry of Human Resource Development (MHRD), Govt. of India, for the financial support through the Half-time Research Assistantship (HTRA) fellowship. I am extremely thankful to all those faculty with whom I did my Teaching Assistantship (TA). The interactions with the undergraduate students during the laboratory sessions as a part of my TA really helped me to improve my teaching skills. I have spent the last five years of my life at the institution and I have had the pleasure of meeting some incredibly talented individuals from different walks of life. I carry wonderful memories with me that will be cherished forever.

I consider it as a luck to have an institution like Indian Institute of Technology Palakkad in my hometown and thus, to enjoy the luxury of being a day scholar. I thank my friends at my native village Krishnadas R., Aneesh C. and Srinivasan P. R., whose cheerful company has been of great help in balancing the professional and personal aspects of my life. I also thank my brother Rajaram T. R. and sister-in-law Viji S., for supporting me with my choice to pursue research. Finally, I would like to thank my beloved mother for her unconditional love, support and encouragement. She has been my pillar of support and motivation throughout my life. I am eternally grateful to my mother and my (late) father for their love for me. Thank you!

CONTENTS

Acronyms	xxix
1 Introduction	1
1.1 Electrostatic MEMS actuation	2
1.2 Motivation and Scope	2
1.3 Organization of the thesis	7
2 Background	11
2.1 Review of statics and dynamics of an electrostatic MEMS actuator	11
2.1.1 Static pull-in	14
2.1.2 Dynamic pull-in	16
2.1.3 Pull-out or release	17
2.2 Ferroelectric negative capacitance	18
2.2.1 Principle of ferroelectric negative capacitance	18
2.2.2 Review of salient experimental proofs for ferroelectric negative capacitance	23
2.3 Review of hybrid MEMS actuator	27
3 Numerical modeling of hybrid actuator	33
3.1 Modeling the hybrid actuator in SPICE	35
3.2 Simulation results and discussion	38
3.2.1 Static response of the actuator	38
3.2.2 Dynamic response of the actuator	40
3.2.3 Impact of ferroelectric damping on the transient response during pull-in	43
3.2.4 Implication on power and energy consumption during dynamic pull-in	45
3.2.5 Effect of MEMS damping on energy consumption during dynamic pull-in	47

3.3	Summary	48
4	Charge based description of standalone and hybrid MEMS actuators	51
4.1	Hamiltonian of the standalone actuator	52
4.2	Analysis of standalone actuator using energy-charge landscape	53
4.2.1	Static pull-in	53
4.2.2	Dynamic pull-in	56
4.2.3	Pull-out	57
4.3	Analysis of hybrid actuator using energy-charge landscape	60
4.4	Estimation of parameters of standalone actuator	63
4.5	Summary	65
5	Analysis of hybrid MEMS actuator using energy-displacement landscape	67
5.1	Hamiltonian of the hybrid actuator	69
5.2	Analysis of the hybrid actuator	70
5.2.1	Static pull-in	71
5.2.2	Dynamic pull-in	71
5.2.3	Pull-out	73
5.3	Effect of adhesion	74
5.4	Summary	79
6	Stable deflection in hybrid MEMS actuator with cubic non-linear spring	81
6.1	Review of pull-in in electrostatic MEMS	83
6.2	Hamiltonian of the hybrid actuator	87
6.3	Analysis of the hybrid actuator	88
6.3.1	Hybrid actuator with a linear spring ($k_3 = 0$)	88
6.3.2	Hybrid actuator with a cubic non-linear spring ($k_3 \neq 0$)	89
6.4	Summary	97
7	Conclusion	101
7.1	Scope for future works	102
A	Appendix	105
A.1	SPICE model of standalone electrostatic MEMS actuator	105
A.1.1	Actuator module	106
A.1.2	Suspension module	107

A.1.3	Adhesion module	108
A.1.4	EOM solver module	109
A.1.5	Anchor module	110
A.2	SPICE netlist of hybrid MEMS actuator	110
	Bibliography	115

LIST OF FIGURES

Figure 1.1	Micro Electro Mechanical Systems (MEMS) devices based on electrostatic actuation	1
Figure 1.2	Schematic representation and 1-DOF model of the standalone MEMS actuator	3
Figure 1.3	Typical dynamic response of the standalone actuator	4
Figure 1.4	Schematic representation and typical static characteristics of the hybrid actuator	5
Figure 2.1	Schematic representation and 1-DOF model of the standalone MEMS actuator	12
Figure 2.2	A capacitive shunt Radio Frequency (RF) MEMS switch	13
Figure 2.3	Static characteristics of the standalone MEMS actuator	15
Figure 2.4	Dynamic characteristics of the standalone MEMS actuator	17
Figure 2.5	Polarization-electric field hysteresis loop and free energy-electric field characteristics of ferroelectric	19
Figure 2.6	Change in the free energy landscape of the ferroelectric due to applied electric field	20
Figure 2.7	Negative capacitance in an isolated ferroelectric capacitor . .	21
Figure 2.8	Energy landscapes in a ferroelectric-dielectric stack	22
Figure 2.9	Steep-slope switching in Negative Capacitance Field Effect Transistor (NCFET)	23
Figure 2.10	Experimental setup and results from Khan et al. [31] demonstrating transient negative capacitance	24
Figure 2.11	Experimental setup and results from Hoffmann et al. [43] illustrating the extraction of the S-shaped polarization-electric field curve, a signature of ferroelectric negative capacitance effect	25

Figure 2.12	Experimental setup and results from Khan et al. [44] depicting capacitance enhancement in a ferroelectric-dielectric stack	26
Figure 2.13	Hybrid MEMS actuator, formed by connecting a ferroelectric capacitor exhibiting negative capacitance, in series with the standalone MEMS actuator	29
Figure 3.1	Schematic representation and 1-DOF model of the hybrid actuator	35
Figure 3.2	Simulation Program with Integrated Circuit Emphasis (SPICE) model of the hybrid actuator	37
Figure 3.3	Static characteristics of the hybrid actuator	39
Figure 3.4	Voltage amplification in hybrid actuator	40
Figure 3.5	Dynamic characteristics of the hybrid actuator	41
Figure 3.6	Effect of ferroelectric thickness on dynamic pull-in voltage and pull-out voltage	42
Figure 3.7	Effect of variation in air-gap and spring constant on the dynamic pull-in voltage in standalone and hybrid actuators	43
Figure 3.8	Dynamic pull-in time analysis of hybrid actuator	44
Figure 3.9	Instantaneous power consumption during dynamic pull-in	45
Figure 3.10	Effect of ferroelectric damping constant on the energy consumption during dynamic pull-in in the hybrid actuator	46
Figure 4.1	Total energy of the electrostatic actuator plotted as a function of charge and current	53
Figure 4.2	Potential energy-charge and equilibrium charge-voltage characteristics of the standalone actuator	54
Figure 4.3	Dynamic pull-in in standalone actuator using energy-charge landscape	55
Figure 4.4	Illustration of pull-out phenomenon using potential energy-charge plot	58
Figure 4.5	Illustration of pull-out phenomenon using phase-portrait	59
Figure 4.6	Analysis of static and dynamic pull-in in hybrid actuator	60

Figure 4.7	Analysis of pull-out in hybrid actuator	62
Figure 4.8	Impact of damping in standalone actuator based on the charge based description	63
Figure 5.1	Potential energy-displacement plot depicting static pull-in .	71
Figure 5.2	Analysis of dynamic pull-in using potential energy-displacement and phase-portrait plots	72
Figure 5.3	Analysis of pull-out using phase-portrait	73
Figure 5.4	Effect of adhesion on static pull-in in the hybrid actuator .	75
Figure 5.5	Numerical simulation of the static characteristics of the hybrid actuator without and with adhesion forces	76
Figure 5.6	Analysis of pull-out in the presence of adhesion	77
Figure 5.7	Variation in the pull-out voltage with respect to the change in the effective gap at contact	78
Figure 5.8	Phase-portrait depicting the increase in the pull-out voltage due to reduced ferroelectric thickness	79
Figure 6.1	Schematic representation of the standalone actuator and equivalent circuit representation of the hybrid actuator . .	83
Figure 6.2	Static characteristics of various MEMS configurations	85
Figure 6.3	Analysis of the static response of the hybrid actuator with linear spring	89
Figure 6.4	Static characteristics of the hybrid actuator for different values of the cubic non-linear spring constant	90
Figure 6.5	Modes of operation in the hybrid actuator based on the cubic non-linear spring constant	91
Figure 6.6	Static characteristics of the hybrid actuator depicting the bistable mode of operation	93
Figure 6.7	Static characteristics of the hybrid actuator obtained using the energy-landscape method and numerical simulation, depicting the bistable mode of operation	95
Figure 6.8	Static characteristics of the hybrid actuator depicting the always-stable mode of operation	96

Figure 6.9	Static characteristics of the hybrid actuator obtained using the energy-landscape method and numerical simulation, depicting the always-stable mode of operation	97
Figure 6.10	Capacitance ratio in MEMS varactor using standalone MEMS with linear spring and hybrid MEMS with cubic non-linear spring (operating in always-stable mode)	98
Figure A.1	SPICE model of a standalone electrostatic MEMS actuator implemented in circuit simulator	106
Figure A.2	SPICE sub-circuit implementation of the actuator module . .	107
Figure A.3	SPICE sub-circuit implementation of the suspension module	108
Figure A.4	SPICE sub-circuit implementation of the adhesion module . .	108
Figure A.5	SPICE sub-circuit implementation of the EOM solver module	109
Figure A.6	SPICE sub-circuit implementation of the anchor module . . .	110

LIST OF TABLES

Table 2.1	Parameters of the standalone MEMS actuator considered in this work	14
Table 2.2	Pull-in and pull-out of a standalone MEMS (clamped-clamped beam) actuator. Values correspond to parameters listed in Table 2.1.	18
Table 2.3	Parameters of the ferroelectric capacitor	30
Table 2.4	Comparison between standalone actuator and hybrid actuator. Note that the operating voltage is reduced in the hybrid actuator, as compared to the standalone actuator.	31
Table 3.1	Parameters of the hybrid actuator used in this work. This consolidates the parameters of the MEMS actuator from Table 2.1 and the parameters of the ferroelectric from Table 2.3. . .	36

Table 3.2	Effect of MEMS damping ratio ζ on the energy consumed during dynamic pull-in.	47
Table 4.1	Pull-in and pull-out of an electrostatic MEMS actuator based on energy-charge landscape	59
Table 5.1	Summary of analysis of the hybrid actuator	74
Table 6.1	Comparison of various MEMS configurations	87

LIST OF SYMBOLS

MEMS Actuator

ϵ_0	Permittivity of free space
A_M	Actuation area
c	Damping coefficient
C_d	Down-state capacitance
C_M	Capacitance of the MEMS actuator
C_u	Up-state capacitance
D	Density
E	Young's modulus
f_0	Resonant frequency
g_0	Air-gap
H_M	Hamiltonian of the MEMS actuator
h_s	Stopper height
k	Linear spring constant
k_1	Linear spring constant
k_3	Cubic spring constant
L	Length of the MEMS beam
l_s	Length of the support in clamped-clamped MEMS actuator
m	Mass

T	Thickness of the MEMS beam
V_M	Voltage drop across the MEMS actuator
V_{DPI}	Dynamic pull-in voltage of the standalone actuator
V_{PO}	Pull-out voltage of the standalone actuator
V_{SPI}	Static pull-in voltage of the standalone actuator
W	Width of the MEMS beam
w_s	Width of the support in clamped-clamped MEMS actuator
x	Displacement of the movable electrode
X_{DPI}	Dynamic pull-in displacement of the standalone actuator
X_{SPI}	Travel range of the standalone actuator
Ferroelectric	
α_F	Ferroelectric anisotropy coefficient
β_F	Ferroelectric anisotropy coefficient
γ_F	Ferroelectric anisotropy coefficient
ρ	Ferroelectric damping constant
A_F	Area of the ferroelectric
C_F	Capacitance of the ferroelectric
E_c	Coercive electric field
P	Polarization of the ferroelectric
P_r	Remanent polarization
t_F	Thickness of the ferroelectric
V_F	Voltage drop across the ferroelectric capacitor

Hybrid Actuator

H_H	Hamiltonian of the hybrid actuator
V_H	Voltage drop across the hybrid actuator
V_{HDPI}	Dynamic pull-in voltage of the hybrid actuator
V_{HPO}	Pull-out voltage of the hybrid actuator
V_{HSPI}	Static pull-in voltage of the hybrid actuator
V_{in}	Input voltage to the hybrid actuator
X_{HDPI}	Dynamic pull-in displacement of the hybrid actuator
X_{HSPI}	Travel range of the hybrid actuator

Other symbols

\dot{q}	Current
\dot{x}	Velocity
C_D	Capacitance of the dielectric
q	Charge
t	Time
t_{inp}	Rise time of the applied input voltage
t_{sys}	System rise time

ABBREVIATIONS

MEMS	Micro Electro Mechanical Systems
IC	Integrated Circuit
RF	Radio Frequency
IRDS	International Roadmap for Devices and Systems
CMOS	Complementary Metal Oxide Semiconductor
MOSFET	Metal Oxide Semiconductor Field Effect Transistor
SPICE	Simulation Program with Integrated Circuit Emphasis
LK	Landau-Khalatnikov
CPW	Coplanar Waveguide
FET	Field Effect Transistor
NCFET	Negative Capacitance Field Effect Transistor
VCVS	Voltage Controlled Voltage Source

INTRODUCTION

Micro Electro Mechanical Systems ([MEMS](#)) integrate micro devices that combine electrical and mechanical components. They can range in size from micrometers to millimeters. They are fabricated using micromachining techniques, based on Integrated Circuit ([IC](#)) batch processing [1, 2]. Broadly, [MEMS](#) devices are classified into two – sensors and actuators. A sensor transforms a change of a physical quantity into an electrical signal that can be measured (for example, a [MEMS](#) pressure sensor). An actuator, on the other hand, converts an input energy into a motion of a microstructure (for example, a [MEMS](#) switch). Due to continuing advancements in research and technology, [MEMS](#) based sensors and actuators play a crucial role in a wide range of present-day applications.

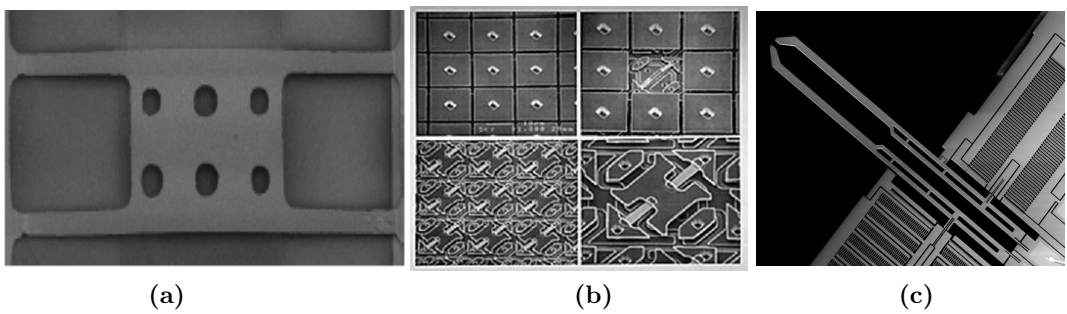


Figure 1.1: [MEMS](#) devices based on electrostatic actuation. (a) [RF MEMS](#) switch [3]. These switches are emerging as basic building blocks in communication systems like mobile phones and satellite communication. (b) Digital micromirror device [4]. These are used in video projectors and optics. (c) Microgripper [5]. These are used in applications such as micro-assembly, biology and tissue engineering.

1.1 ELECTROSTATIC MEMS ACTUATION

There are different actuation methods available for **MEMS** actuators such as electrostatic actuation, piezoelectric actuation, electromagnetic actuation and electrothermal actuation. Electrostatic actuation is the most commonly used method in **MEMS** due to low power consumption, low cost, fast response and ease of fabrication [1, 6]. Electrostatic **MEMS** actuators employ Coulombic force of attraction between a movable electrode and a fixed electrode due to an applied voltage, to induce a displacement in the movable electrode. Electrostatic **MEMS** actuators are an integral part of today's electronics, forming the backbone of a wide range of devices such as Radio Frequency (**RF**) switches [7], digital micromirror devices [8, 9], micromirror switches, microgrippers, micromotors [10] and so on. Figure 1.1 shows some of the typical **MEMS** devices based on electrostatic actuation [3–5]. The International Roadmap for Devices and Systems (**IRDS**) describes the significance of many such devices in applications ranging from consumer to automotive to medical electronics [11].

1.2 MOTIVATION AND SCOPE

Overview of electrostatic MEMS actuators

To investigate the behavior of the electrostatic actuator, we consider a clamped-clamped standalone actuator driven by an input voltage V_M , whose schematic representation is shown in Figure 1.2(a). This structure is similar to the **RF MEMS** switch shown in Figure 1.1(a). We model this actuator using a single degree of freedom (1-DOF) lumped parameter model, based on a spring-mass-damper system, as depicted in Figure 1.2(b). This model is simple but efficient for a first-cut design and analysis of the **MEMS** actuators [1]. It is useful for evaluating the static and dynamic electromechanical behavior of the **MEMS** actuators with sufficient accuracy [12]. The response of the electrostatic actuator to slowly varying input

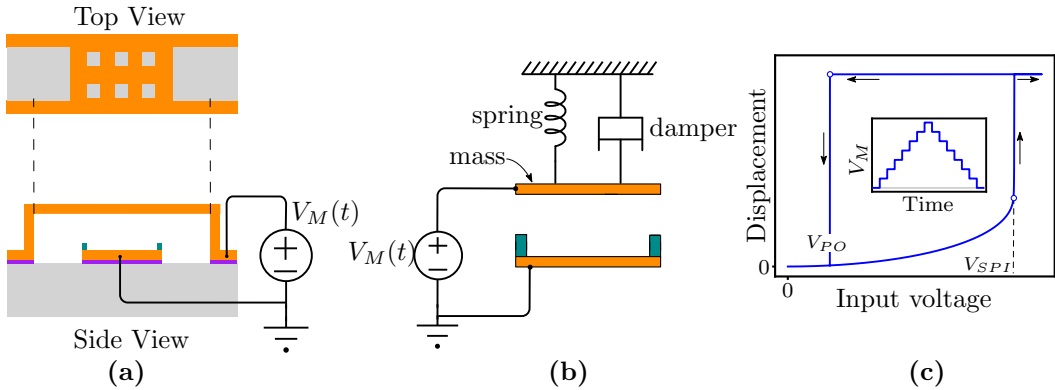


Figure 1.2: (a) Schematic representation of a clamped-clamped standalone MEMS actuator. (b) Single degree of freedom (1-DOF) model of the actuator. (c) Typical static characteristic of the standalone actuator depicting the displacement of the movable electrode as a function of applied input voltage. Inset shows the slowly varying input voltage as a function of time.

is called as static response. The typical static characteristic (displacement of the movable electrode as a function of the applied voltage) of the standalone MEMS actuator is shown in Figure 1.2(c). As the input voltage is increased, beyond a particular voltage called the static pull-in voltage V_{SPI} , the movable electrode snaps down onto the fixed electrode. This condition is called static pull-in. Pull-in occurs when the spring restoring force can no longer compensate the electrostatic force of attraction. After achieving pull-in, as the input voltage is reduced to a particular voltage called the pull-out voltage V_{PO} , the movable electrode gets detached from the bottom. This condition is called pull-out. Details of the actuator, 1-DOF model and static characteristics are explained later in Chapter 2.

Electrostatic MEMS actuators are widely used in switching applications [7]. It is, hence, important to study the transient behavior. This involves the analysis of the dynamic response (response to step input) of the hybrid actuators. Note that the response of electrostatic MEMS actuators to voltage excitation is different for static and dynamic inputs. For instance, consider the standalone actuator excited with a step input with amplitude V_M , as shown in Figure 1.3(a). The typical dynamic characteristic (applied step input and displacement of the movable electrode as a function of time) of the standalone actuator is shown in Figure 1.3(b). The response

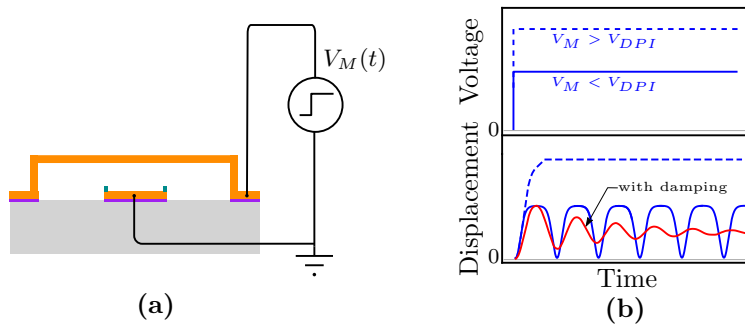


Figure 1.3: (a) Schematic representation of the standalone actuator with step input. (b) Typical dynamic characteristics of the standalone actuator, depicting the step input and displacement as a function of time. Note that dynamic pull-in occurs when the amplitude of the step input V_M exceeds the dynamic pull-in voltage V_{DPI} .

of the actuator, in the absence of damping, is oscillatory, when the amplitude of the step input is less than the dynamic pull-in voltage V_{DPI} . In the presence of damping, these oscillations die out and the actuator settles at the static equilibrium displacement, corresponding to the magnitude of the applied step input. When the amplitude of the step input exceeds V_{DPI} , the top electrode snaps down, resulting in dynamic pull-in. Typically, the dynamic pull-in voltage V_{DPI} is less than the static pull-in voltage V_{SPI} [1]. Details of the dynamic characteristics are explained later in Chapter 2.

While the electrostatic **MEMS** actuators offer several advantages, they demand high operating voltages, ranging from few tens to hundreds of volts [7]. This is typically much larger than the supply voltages used in modern Complementary Metal Oxide Semiconductor (**CMOS**) integrated circuits. Hence, it is necessary to develop novel ideas and strategies to realize low-voltage **MEMS** actuators.

Additional on-chip voltage sources and drive electronics are used in present-day **MEMS-CMOS** integrated circuits to meet the high operating voltage requirement of the electrostatic **MEMS** actuators [13, 14]. Efforts to reduce the operating voltage of the **MEMS** actuators involve innovative designs, such as scaling down the structural parameters, such as the air gap below 10 nm [15]. However, reliable fabrication and operation of **MEMS** structures with extremely small air gaps are very challenging due to stiction [16]. Stiction in **MEMS** actuators is a failure mode wherein the top

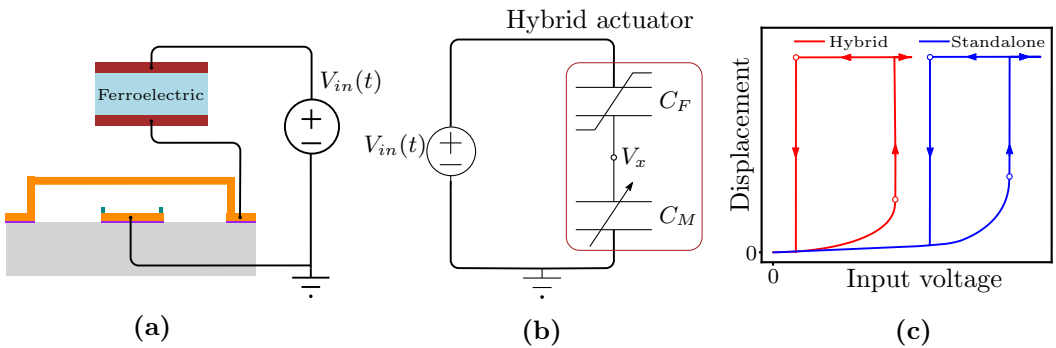


Figure 1.4: (a) Schematic representation of the hybrid actuator. (b) Equivalent circuit representation of the hybrid actuator. Voltage amplification due to negative capacitance of the ferroelectric results in $V_x > V_{in}$. (c) Typical static characteristics of the standalone and hybrid actuators. Note that the operating voltage is reduced in the hybrid actuator.

and bottom electrodes of the actuator stick together. This unintentional adhesion occurs when the restoring forces are unable to overcome the surface forces.

A novel idea to mitigate the demand for a high operating voltage in an electrostatic **MEMS** actuator was proposed by Masuduzzaman and Alam [17], by connecting a ferroelectric capacitor exhibiting negative capacitance, in series with the **MEMS** actuator, thus forming a **hybrid MEMS actuator**. Figure 1.4(a) shows the schematic representation of the hybrid actuator driven by an input voltage V_{in} . The corresponding equivalent circuit representation is shown in Figure 1.4(b). Here, C_F and C_M denote the capacitance of the ferroelectric and the variable capacitance of the **MEMS** actuator, respectively. The intermediate node voltage is denoted as V_x . In the hybrid actuator, the ferroelectric is operating in its negative capacitance regime. Over the past decade, the existence of negative capacitance in ferroelectric and its utility for different applications have been widely explored. Details of the ferroelectric negative capacitance are explained later in Chapter 2. Now, with the ferroelectric operating in the negative capacitance regime, we have, from Figure 1.4(b), for an applied input voltage V_{in} ,

$$V_x = V_{in} \cdot \frac{|C_F|}{|C_F| - C_M} \Rightarrow V_x > V_{in} \quad (1.1)$$

Thus, the negative capacitance of the ferroelectric results in a voltage amplification phenomenon [18], leading to $V_x > V_{in}$. This results in a reduction in the

operating voltage in the hybrid actuator, as compared to the standalone actuator [17]. Figure 1.4(c) compares our calculations for the static response of the standalone and hybrid actuators [19]. Note that the static operating voltage is predicted to be reduced in the hybrid actuator, as compared to the standalone actuator.

Motivation

The response of the hybrid actuator to slowly varying static inputs was predicted analytically in Ref. [17]. However, the dynamic response of the hybrid actuator, by coupling the differential equations governing the MEMS actuator and the ferroelectric, has not been analyzed in the literature. Hence, we identify that it is important to investigate the dynamic response of the hybrid actuator.

Another challenge faced by the electrostatic MEMS actuator is its limited operation range due to the *pull-in* instability. Beyond the pull-in voltage, the movable electrode snaps down onto the fixed electrode [1]. As a result, the maximum distance traveled by the movable electrode before it snaps down (termed as travel range), is limited to a fraction of the air-gap between the two electrodes. Therefore, the entire range in the air-gap is not available for the stable operation of the electrostatic MEMS actuator. Extending the travel range is useful for various analog positioning applications, for example, MEMS varactors. Several configurations have been proposed in the literature [20–22] to extend the travel range or eliminate the pull-in instability. However, in these configurations, the improved stability is achieved at the cost of increased supply voltage, as compared to the actuation voltage of the standalone MEMS actuator. Therefore, it is important to investigate the possibility of eliminating pull-in, while operating at a lower voltage as compared to the standalone MEMS actuator.

Research objectives

To investigate the dynamic response of the hybrid actuator: In this thesis, we analyze the dynamic response (and also static response) of the hybrid actuator. We propose

numerical and graphical frameworks to model the hybrid actuator. We use a 1-DOF (single degree of freedom) model for the voltage driven, parallel plate, electrostatic [MEMS](#) actuator and couple it with the physics of the ferroelectric negative capacitance, governed by the 1-D Landau-Khalatnikov ([LK](#)) equation, to model the hybrid actuator. We use the proposed numerical and graphical frameworks to investigate the response of the hybrid actuator to both static (slowly varying) and dynamic (step) inputs.

To obtain low-voltage and pull-in free operation in the hybrid actuator: We also propose the elimination of pull-in instability accompanied with low-voltage operation in the hybrid actuator by adding a cubic non-linear spring to it. We illustrate the improvement in the stability of the hybrid actuator by using the proposed numerical and graphical frameworks.

1.3 ORGANIZATION OF THE THESIS

The work presented in this thesis describes the modeling of hybrid [MEMS](#) actuators and investigates their response to static and dynamic (step) inputs. Each chapter begins with a review of the relevant literature. The [Appendix](#) provided at the end of the thesis gives additional details regarding the proposed modeling framework.

We begin by providing a background, in Chapter [2](#), into topics and terminologies, that will be of assistance in understanding the work presented in the remaining chapters. We present an overview of the electrostatic [MEMS](#) actuator using a 1-DOF (single degree of freedom) model and explain the concept of pull-in and pull-out for static and dynamic conditions. We also describe the concept of ferroelectric negative capacitance. Then, we review the hybrid actuator, explaining its design and operating principle.

Chapter [3](#) deals with the numerical modeling of the hybrid actuator using Simulation Program with Integrated Circuit Emphasis ([SPICE](#)), implemented in a circuit simulator. Our approach couples the non-linear dynamics of both the ferroelectric capacitor and the [MEMS](#) actuator. We illustrate the low-voltage operation of the hybrid actuator for both static and dynamic (step) inputs. We use the trade off

between the pull-in time and actuation voltage to predict low-voltage operation of the hybrid actuator without compromising on the pull-in time. We also show that the energy consumed by the hybrid actuator is less than that in the standalone actuator, even in the presence of damping.

In Chapter 4, we use energy landscape to analyze the pull-in and pull-out phenomena. In the hybrid actuator, since both the ferroelectric and the MEMS actuator are in series, they share the same charge. Hence, in this chapter, we develop a framework to analyze the hybrid actuator, using charge as the common variable. We propose a graphical approach to analyze the hybrid actuator using its energy-charge landscape. This technique involves coordinate transformation from displacement to charge, thereby formulating the Hamiltonian of the actuator in terms of charge. The response of the actuator to static and dynamic (step) inputs is studied graphically, using its energy-charge and phase-portrait (charge vs. current) plots. For the standalone actuator, we also derive the analytical expressions for the voltage and charge, under static and dynamic conditions. Further, we propose a procedure to estimate various parameters of the standalone actuator, based on the proposed energy method. The mapping function derived in this chapter can also be used to analyze the hybrid actuator using its energy-displacement landscape, as explained in Chapter 5.

In Chapter 5, we propose an energy-displacement framework to analyze the statics and dynamics of the hybrid actuator using the mapping function described in Chapter 4. We make use of the graphical energy-displacement and phase-portrait (displacement vs. velocity) plots to estimate the pull-in and pull-out voltages in the hybrid actuator. The results obtained using the proposed approach are in good agreement with the numerical simulations in Chapter 3 and with the analytical results in Ref. [17]. The proposed framework also enables straightforward inclusion of adhesion between the contacting surfaces, modeled using van der Waals force. We show that the pull-in voltage is not affected, while the pull-out voltage is reduced due to adhesion.

In Chapter 6, we propose pull-in free, low-voltage operation by using the hybrid actuator with a cubic non-linear spring. We use the physics-based framework

based on the energy landscape, detailed in Chapter 5, to illustrate the stability improvement. We predict that, for an applied voltage, based on the value of the cubic spring constant, the actuator can operate in three distinct modes: (a) monostable, (b) bistable and (c) always-stable. We also estimate the threshold values of the cubic spring constant that demarcate the three modes of operation. By proper design of the cubic spring constant, we predict that the hybrid actuator working in the always-stable mode, eliminates pull-in and operates at a lower voltage, as compared to the standalone actuator. The results obtained are in agreement with the numerical simulations.

Finally, in Chapter 7, we summarize our results and provide directions for future work.

2

BACKGROUND

This chapter provides some background information related to the working of standalone MEMS actuators and hybrid MEMS actuators. It also describes the basic principle of ferroelectric negative capacitance. Though the MEMS actuator is a 3-dimensional structure, we use a 1-DOF (single degree of freedom) lumped-parameter model that neglects the transverse deflection of the beam along its length. More accurate analysis can be done if a distributed parameter model [1] of the beam is used. The lumped parameter model, however, is useful for evaluating coupled-domain behavior as in the case of an electrostatic MEMS. It can be easily used for a first-cut analysis of the system to obtain the basic understanding of the statics and dynamics [1]. Further, the reported error in the actuation voltage, calculated using a lumped parameter model, is within 10% [12]. We first review the statics and dynamics of the standalone actuator, followed by the basics of ferroelectric negative capacitance. The hybrid actuator, formed by connecting the ferroelectric capacitor in series with the MEMS actuator, is also described in this chapter.

2.1 REVIEW OF STATICS AND DYNAMICS OF AN ELECTROSTATIC MEMS ACTUATOR

Electrostatic MEMS actuators are very popular and are widely used because of their inherent low power consumption [1]. The actuator, in its generic form, consists of a movable electrode and a fixed electrode, separated by an air-gap. By the application of a voltage between the electrodes, an attractive electrostatic force is generated between the two electrodes, which results in a mechanical displacement of the movable electrode. Thus, the two electrodes form a deformable capacitor. Based on their geometry, there are different types of electrostatic actuators such as

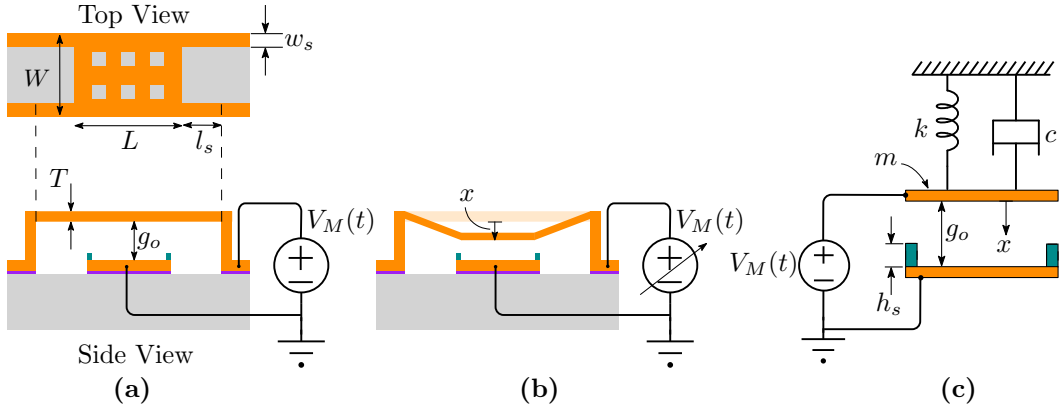


Figure 2.1: (a) Schematic representation of a clamped-clamped standalone MEMS actuator. (b) Deflection of the movable electrode in response to an applied voltage. (c) Single degree of freedom (1-DOF) model of the standalone actuator.

cantilever (fixed-free) beams, clamped-clamped (fixed-fixed) beams, comb-drives and torsional actuators [1].

We consider a clamped-clamped (fixed-fixed) beam as a prototype of the standalone MEMS actuator, based on Ref. [3]. The schematic representation is shown in Figure 2.1(a). The side view shows a fixed bottom electrode and a movable top electrode, with an air-gap g_o between them. Fixed-fixed support/flexure beams [3, 7] of length l_s and width w_s are used to support the top electrode, as shown in the top view. The length, width and thickness of the movable electrode are labeled as L, W and T , respectively. Holes are introduced in the top electrode to improve the switching dynamics by varying the damping [3]. Due to an applied voltage, the top electrode moves down, as shown in Figure 2.1(b). The dynamical variable x denotes the midpoint deflection of the movable top electrode in the clamped-clamped structure. We use a single degree-of-freedom (1-DOF) model, as depicted in Figure 2.1(c), to model this clamped-clamped beam. This is a lumped parameter model that approximates the MEMS actuator as a variable parallel plate capacitor. The actuator is excited by an input voltage $V_M(t)$, where t denotes time. The inertia, energy dissipation, and stiffness of the device are modeled using an effective mass m , a viscous damper with damping coefficient c , and a spring of spring constant k , respectively. The displacement of the top electrode, denoted by x , is limited by means of a pair of stoppers of height h_s , as shown in Figure 2.1(c).

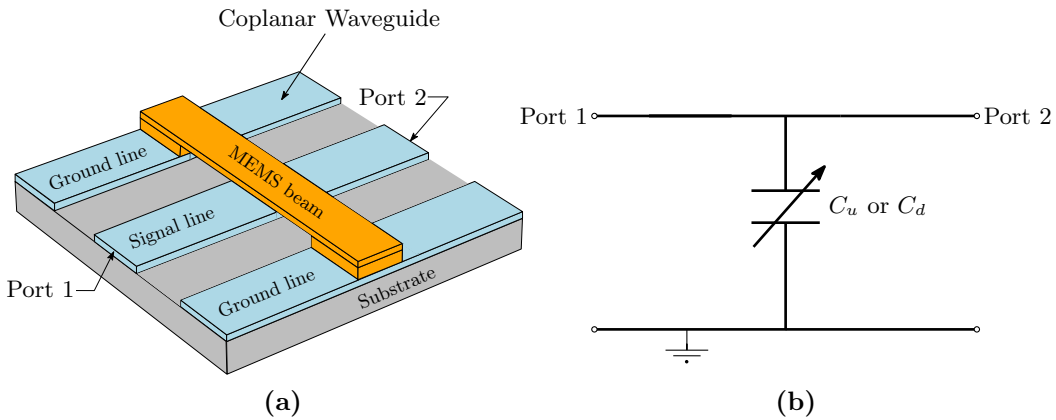


Figure 2.2: (a) A capacitive shunt RF MEMS switch. (b) Equivalent circuit of the switch offering an up-state capacitance C_u and a down-state capacitance C_d , based on the applied voltage.

The stoppers are made of insulating material and hence, prevent electrical short between the top and bottom electrodes [23–25]. These stoppers also minimize the area of contact when the top electrode snaps down on to the bottom electrode and thus reduce the effect of surface forces. The effect of surface forces is neglected in this chapter and is studied later in Chapter 5. Damping coefficient c is set to zero for the ease of analysis and to enable comparison with the theoretical results, wherever applicable. We consider the case of non-zero damping later in Chapter 3. Based on Refs. [3, 7], the values of the MEMS actuator parameters are listed in Table 2.1 and are fairly typical for electrostatic MEMS actuators.

Such clamped-clamped MEMS actuators are widely used in capacitive shunt RF MEMS switches [7]. For instance, a MEMS switch is integrated in a Coplanar Waveguide (CPW), as shown in Figure 2.2(a). The anchors of the actuator beam are connected to the CPW ground planes. The switch is, thus, placed in shunt between the transmission line and ground, as illustrated in Figure 2.2(b). The switch, offers two capacitances – an up-state capacitance $C_u = \frac{\epsilon_0 A_M}{g}$, when no voltage is applied and a down-state capacitance $C_d = \frac{\epsilon_0 A_M}{h_s}$, for $V_M > V_{SPI}$. Note that C_d is greater than C_u . Thus, with no actuation voltage, the capacitance is small (C_u) and it does not affect the impedance of the signal line. Therefore, the switch is in the on state, thereby causing the RF signal at port 1 to pass through the line to reach port 2. When $V_M > V_{SPI}$ is applied, the capacitance is higher (C_d) and this affects the

Table 2.1: Parameters of the standalone MEMS actuator considered in this work

Parameter	Value
Beam material	Gold (Au) [3]
Length of the beam, L	140 μm
Width of the beam, W	120 μm
Thickness of the beam, T	0.5 μm
Actuation area, A_M	$1.44 \times 10^{-8} \text{ m}^2$
Young's modulus, E	78 GPa
Density, D	19280 kg/m^3
Mass, $m = 0.35 \times D \times \text{volume}$	$5.6 \times 10^{-11} \text{ kg}$ [7]
Width of the support, w_s	20 μm
Length of the support, l_s	80 μm
Spring constant, $k = 4Ew_s(\frac{T}{l_s})^3$	1.52 N/m [7]
Initial air-gap, g_0	2 μm
Stopper height, h_s	0.15 μm
System rise time, t_{sys}	13.28 μs
Permittivity of free space, ϵ_0	$8.854 \times 10^{-12} \text{ F/m}$

impedance of the signal line, thereby blocking the transmission of signal from port 1 to port 2. Now, the switch is said to be in off state.

2.1.1 Static pull-in

The static response of the electrostatic MEMS actuator is characterized by applying a slow varying input $V_M(t)$. The input voltage is considered to be *slow* if its rise time, t_{inp} , is significantly greater than the system rise time, t_{sys} of the MEMS actuator. Empirically, $t_{sys} = 0.35/f_0$, where the resonant frequency $f_0 = \frac{1}{2\pi}\sqrt{k/m}$ [26]. Thus, when $t_{inp} \gg t_{sys}$, the actuator remains in quasi-static equilibrium. As the

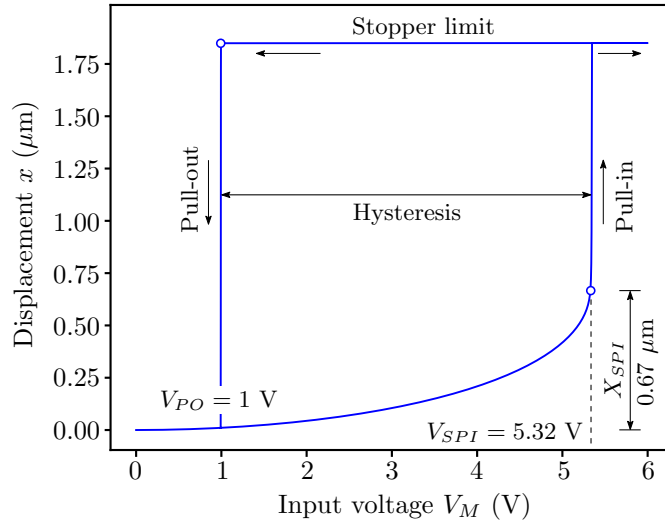


Figure 2.3: Static displacement-voltage characteristics of the standalone MEMS actuator.

The static pull-in and pull-out voltages are 5.32 V and 1 V, respectively. The travel range is 0.67 μm .

input voltage is increased, beyond a certain voltage, called the static pull-in voltage V_{SPI} , the movable electrode snaps down on to the fixed electrode. This condition is called static pull-in [1]. Consequently, the maximum distance traveled by the movable electrode, before it snaps down, is called the travel range X_{SPI} . At static equilibrium, the restoring spring force, F_{spring} balances the attractive electrostatic force, F_{elec} . That is, at static equilibrium, we have,

$$F_{spring} = F_{elec} \quad (2.1a)$$

$$kx = \frac{1}{2} \frac{\epsilon_0 A_M V_M^2}{(g_o - x)^2} \quad (2.1b)$$

where, ϵ_0 is the permittivity of free space and A_M is the area of actuation. Note that the spring force is linear and the electrostatic force is non-linear in x . As a result, beyond the static pull-in voltage, the electrostatic force exceeds the spring force and thus, the balance between the two forces is lost. Therefore, the top electrode snaps down, resulting in static pull-in. The static pull-in voltage V_{SPI} and the travel range X_{SPI} are given by [1]

$$V_{SPI} = \sqrt{\frac{8kg_o^3}{27\epsilon_0 A_M}} \quad (2.2a)$$

$$X_{SPI} = \frac{g_o}{3} \quad (2.2b)$$

Using the values of the **MEMS** parameters listed in Table 2.1, the static displacement-voltage characteristics are obtained numerically, as shown in Figure 2.3, by applying a slowly varying input (with $t_{inp} = 80$ ms $\gg t_{sys}$). The numerical simulation is based on the 1-DOF model of the standalone **MEMS** actuator and is implemented using **SPICE**, based on Ref. [27]. Detailed implementation of the standalone actuator using **SPICE** is described in [Appendix](#), at the end of the thesis. As depicted in Figure 2.3, we obtain a static pull-in voltage of 5.32 V and a travel range of 0.67 μm for the standalone **MEMS** actuator. The results obtained from the numerical simulation are in agreement with the analytical predictions based on Eq. (2.2).

2.1.2 Dynamic pull-in

The dynamic response of the actuator is characterized by applying a step-input of amplitude V_M . For a step input (with $t_{inp} \ll t_{sys}$), the actuator is driven away from equilibrium [26]. In the absence of damping, the response of the actuator is oscillatory, for voltages less than V_{DPI} , called the dynamic pull-in voltage. The maximum value of this oscillatory displacement of the electrode is referred to as the dynamic pull-in displacement, X_{DPI} and is obtained when $V_M = V_{DPI}$ [1]. For $V_M > V_{DPI}$, the top electrode snaps down to hit the bottom stoppers, resulting in dynamic pull-in. The dynamic pull-in voltage V_{DPI} and dynamic pull-in displacement X_{DPI} are given by [1]

$$V_{DPI} = \sqrt{\frac{kg_o^3}{4\epsilon_o A_M}} \quad (2.3a)$$

$$X_{DPI} = \frac{g_o}{2} \quad (2.3b)$$

Figure 2.4 depicts the dynamic response of the standalone actuator to a step input (with $t_{inp} = 1$ ps $\ll t_{sys}$), obtained numerically. We use the **SPICE** model of the standalone actuator, based on Ref. [27] for the numerical simulations. We obtain a dynamic pull-in voltage of 4.88 V and a corresponding dynamic pull-in displacement of 1 μm , as shown in Figure 2.4(a). The results obtained from the numerical simulations are in agreement with the analytical predictions based on Eq.

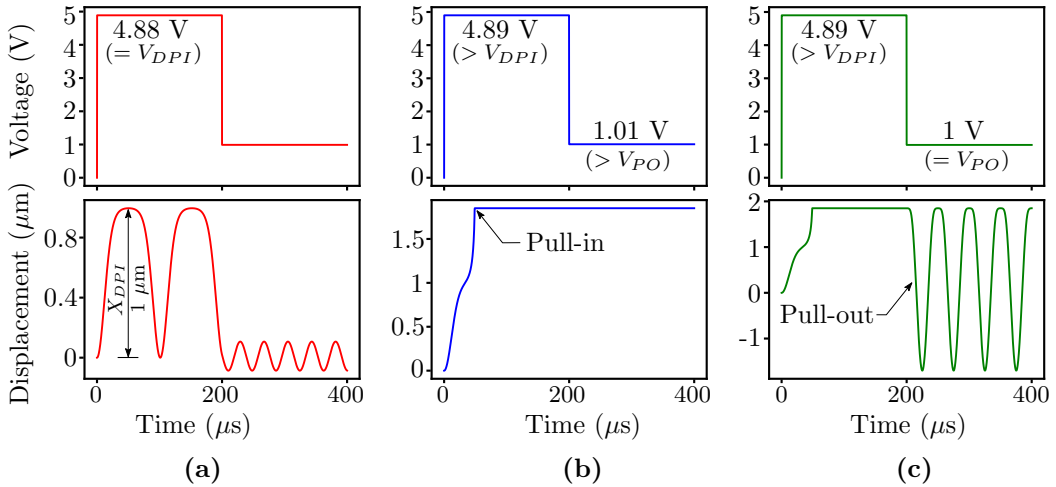


Figure 2.4: Dynamic characteristics of the standalone MEMS actuator. (a) Actuator response before dynamic pull-in with dynamic pull-in voltage of 4.88 V and pull-in displacement of 1 μm. (b) Actuator response after dynamic pull-in and without pull-out. (c) Actuator response after dynamic pull-in and with pull-out. The pull-out voltage is 1 V.

(2.3). When V_M exceeds V_{DPI} , dynamic pull-in occurs, as shown in Figure 2.4(b). With an increase in damping constant c , the dynamic pull-in voltage increases from V_{DPI} and approaches the static pull-in voltage V_{SPI} [28]. The impact of damping on the standalone MEMS actuator is discussed in the next chapter.

2.1.3 Pull-out or release

After achieving pull-in (static or dynamic), as the input voltage is reduced to a specific value, called the pull-out voltage V_{PO} , the pull-in condition is lost and thus, the movable top electrode gets detached from the fixed bottom electrode. This condition is called pull-out or release phenomenon [1]. The pull-out voltage is given by [1]

$$V_{PO} = \sqrt{\frac{2kh_s^2(g_o - h_s)}{\epsilon_0 A_M}} \quad (2.4)$$

Figure 2.3 shows the pull-out in the static characteristics, occurring at $V_{PO} = 1$ V. This is in agreement with the analytical value, given by Eq. (2.4). Pull-out is also illustrated in the dynamic characteristics in Figure 2.4. Pull-out does not occur

Table 2.2: Pull-in and pull-out of a standalone MEMS (clamped-clamped beam) actuator.
Values correspond to parameters listed in Table 2.1.

Parameter	Expression [1]	Value (Analytical/Numerical)
Static pull-in voltage, V_{SPI}	$\sqrt{8kg_o^3/27\epsilon_o A_M}$	5.32 V
Travel range, X_{SPI}	$g_o/3$	0.67 μm
Dynamic pull-in voltage, V_{DPI}	$\sqrt{kg_o^3/4\epsilon_o A_M}$	4.88 V
Dynamic pull-in displacement, X_{DPI}	$g_o/2$	1 μm
Pull-out voltage, V_{PO}	$\sqrt{\frac{2 k h_s^2 (g_o - h_s)}{\epsilon_o A_M}}$	1 V

until the step input is reduced to $V_{PO} = 1$ V, as depicted in Figures 2.4(b),(c). Note the absence of pull-out in Figure 2.4(b) when the step input is 1.01 V and the occurrence of pull-out in Figure 2.4(c) when the step input is 1 V. After pull-out, the response of the actuator is oscillatory in the absence of damping, as shown in Figure 2.4(c). In the presence of damping, after pull-out, the oscillations die out and the actuator settles at an equilibrium displacement, corresponding to the applied voltage. Thus, to summarize, pull-out occurs whenever the input is reduced to a value less than or equal to V_{PO} .

Table 2.2 gives a summary of the pull-in and pull-out of the standalone MEMS actuator. The values mentioned correspond to the numerical simulation results obtained using SPICE, based on Ref. [27] and are in agreement with the analytical expressions.

2.2 FERROELECTRIC NEGATIVE CAPACITANCE

2.2.1 Principle of ferroelectric negative capacitance

A ferroelectric material is a non-centrosymmetric material having spontaneous polarization which can be reversed by the application of an electric field [29].

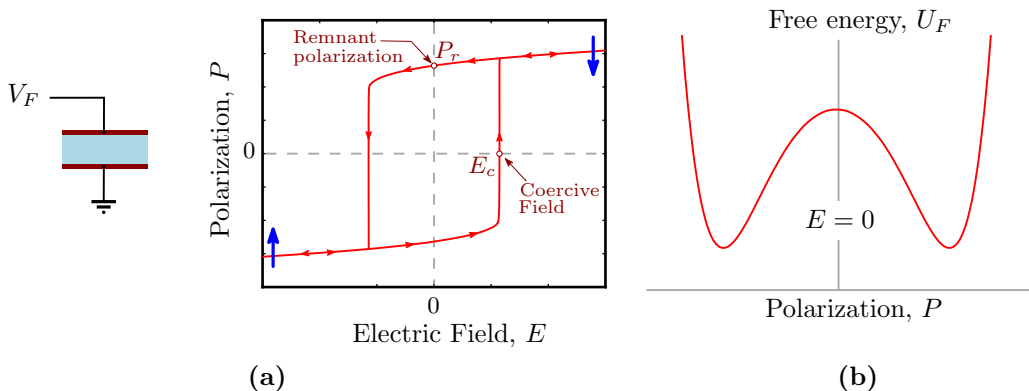


Figure 2.5: (a) Polarization-electric field hysteresis loop of the ferroelectric, depicting coercive field E_c and remanent polarization P_r . (b) Free energy-electric field plot for zero applied electric field. The energy minima represent the stable polarization states.

The polarization P - electric field E hysteresis loop of a typical ferroelectric is shown in Figure 2.5(a). The ferroelectric switches between the two stable states (denoted by up and down arrows in Figure 2.5(a)), when the applied electric field exceeds the coercive field E_c . The value of the polarization when the applied electric field is zero is termed as the remanent polarization P_r . The ferroelectric is also characterized by its free energy U_F versus polarization P plot as shown in Figure 2.5(b), plotted for zero applied electric field. The two energy minima in the free energy landscape correspond to the two stable polarization states of the ferroelectric. The applied electric field changes the free energy landscape as depicted in Figure 2.6. Different polarization values (marked 1 to 6) are denoted in the plot to show the transition. When the applied electric field is zero, the stable polarization state is at the minima on the left side in the free energy-electric field plot. This corresponds to a polarization value, denoted as 1 in the $P - E$ plot. The increase in electric field results in the titling of the energy landscape and now the stable polarization is at a value denoted as 2 in the $P - E$ plot. When the electric field exceeds the coercive field, the stable polarization state makes a transition to the minima on the right side. This corresponds to a polarization value denoted as 3 in the $P - E$ plot. Conversely, when the electric field is reduced beyond the negative coercive field, the stable polarization makes a transition from the minima

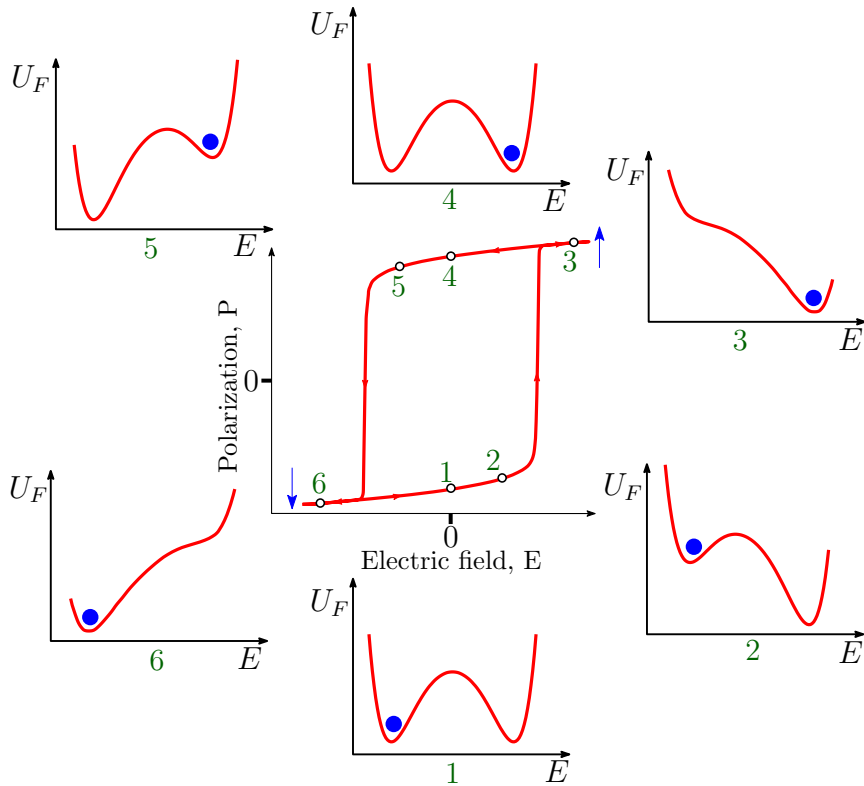


Figure 2.6: Change in the free energy U_F landscape of the ferroelectric due to the applied electric field E .

on the right side to the minima on the left side in the free energy-electric field plot. Correspondingly, the polarization value changes to 6, through 4 and 5, in the $P - E$ plot. Thus, when the applied field is changed, the stable polarization state makes a transition from one minima to the other in the energy landscape.

We assume the ferroelectric capacitor to behave as a single homogeneous domain. In the case where the ferroelectric material is inhomogeneous, the single domain assumption could describe an averaged response, using an effective value of the ferroelectric coefficients [30]. Literature ([31], [32], [33], [30, 34–36]) reports the use of the single domain assumption to describe experimental results with different ferroelectrics for thicknesses upto ~ 100 nm. The physics of the ferroelectric is governed by the time dependent LK equation as [18]

$$\rho \frac{dP}{dt} + \nabla_P U_F = 0 \quad (2.5)$$

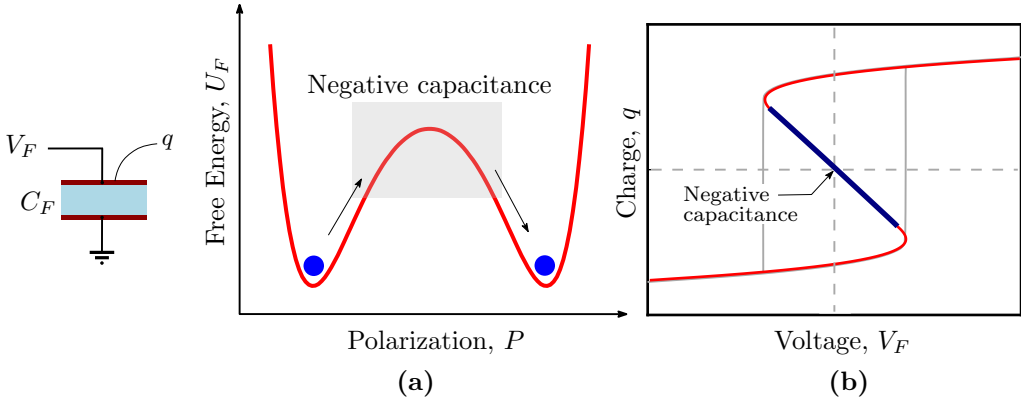


Figure 2.7: Negative capacitance in an isolated ferroelectric capacitor C_F . Negative capacitance regime is represented by the (a) maxima in the free energy landscape and (b) negative sloped region in the charge-voltage characteristics.

where U_F is the free energy and ρ is the ferroelectric damping constant. The free energy U_F is expressed in terms of the polarization P and electric field E as

$$U_F = \frac{1}{2} \alpha_F P^2 + \frac{1}{4} \beta_F P^4 + \frac{1}{6} \gamma_F P^6 - P \cdot E \quad (2.6)$$

Substituting Eq. (2.6) in Eq. (2.5), we get,

$$V_F(q, t) = -\alpha q + \beta q^3 + \gamma q^5 + R_F \frac{dq}{dt} \quad (2.7)$$

where V_F is the voltage across the ferroelectric, q is the charge and

$$\alpha = \frac{-\alpha_F t_F}{A_F}; \beta = \frac{\beta_F t_F}{A_F^3}; \gamma = \frac{\gamma_F t_F}{A_F^5}; R_F = \frac{\rho t_F}{A_F} \quad (2.8)$$

Here, α_F , β_F and γ_F are the ferroelectric anisotropy coefficients, t_F and A_F are the thickness and area of the ferroelectric, respectively. The ferroelectric traverses through a region of negative capacitance between its two stable polarization states [18]. This negative capacitance region is represented by the maxima in its energy landscape, as shown in Figure 2.7(a), for an isolated ferroelectric capacitor C_F . Correspondingly, this translates to a negative sloped region in its charge-voltage plot (and hence the name negative capacitance), as depicted in Figure 2.7(b).

Note that an isolated ferroelectric cannot be stabilized at the negative capacitance regime as it represents an unstable maxima in the energy landscape. However, if the ferroelectric capacitor operating in the negative capacitance regime is connected

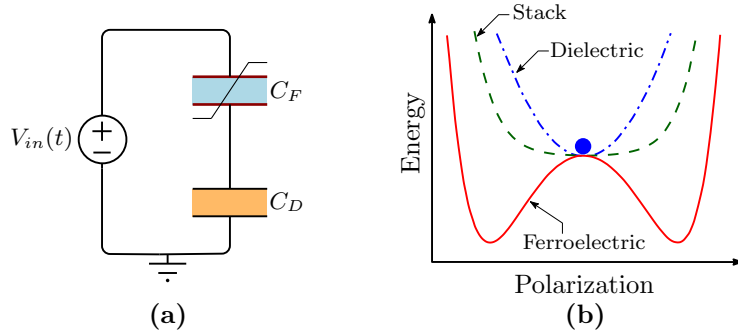


Figure 2.8: (a) A ferroelectric-dielectric stack formed by the series connection of a ferroelectric capacitor C_F and a dielectric C_D . (b) Energy landscapes of an isolated ferroelectric, a dielectric and a ferroelectric-dielectric stack.

in series with a dielectric (positive capacitor) to form a ferroelectric-dielectric stack (see Figure 2.8(a)), such that the overall capacitance is positive, then the combined system becomes stable. This is illustrated in Figure 2.8(b), where the energy landscapes of an isolated ferroelectric, a dielectric and the ferroelectric-dielectric stack are shown. Though the operating state is at the maxima (negative capacitance) in the energy landscape of the ferroelectric, it is at the minima in the energy landscape of the stack and thus, the ferroelectric-dielectric stack is stabilized at that operating state. In other words, the unstable negative capacitance of the ferroelectric is stabilized by the series positive capacitance of the dielectric, such that the combined system is stable.

The idea of using a ferroelectric for low-voltage operation in a Field Effect Transistor (FET) was proposed by Sayeef and Datta in Ref. [18]. They proposed that steep-slope switching characteristics with subthreshold swing $SS < 60$ mV/decade can be achieved by replacing the standard insulator in the MOSFET with a ferroelectric insulator of proper thickness. Figure 2.9(a) shows a schematic representation of a Negative Capacitance Field Effect Transistor (NCFET) [37]. Figure 2.9(b) compares the subthreshold swing SS in an NCFET and a standard MOSFET. The subthreshold swing SS is less than 60 mV/decade in the NCFET. The improvement in subthreshold swing in the NCFET is predicted due to an internal voltage amplification phenomenon caused by the ferroelectric negative capacitance. The voltage amplification phenomenon due to the negative capacitance effect is explained as follows.

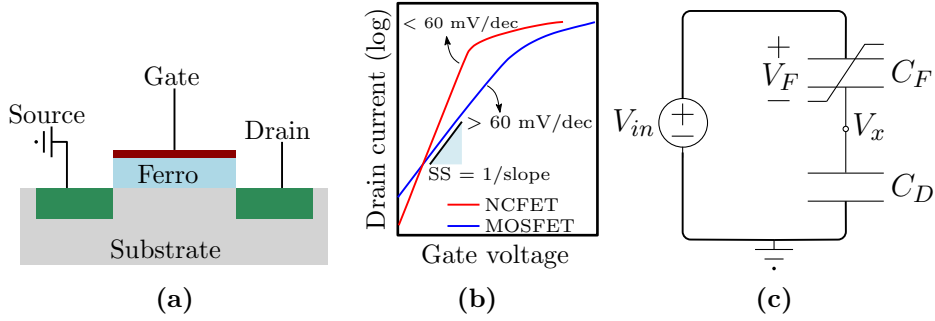


Figure 2.9: (a) Schematic representation of an NCFET [18, 37]. (b) Typical transfer characteristics of an NCFET and a MOSFET. Note that the Subthreshold swing (SS) is less than 60 mV/decade in the NCFET. (b) Equivalent circuit representation of the ferroelectric-dielectric stack. The voltage at the intermediate node V_x is greater than the input voltage V_{in} due to voltage amplification effect caused by the ferroelectric negative capacitance.

Consider the equivalent circuit representation of a ferroelectric-dielectric stack as shown in Figure 2.9(c). The ferroelectric capacitor C_F , operating in the negative capacitance regime, is connected in series with a positive capacitor C_D . The input voltage to the stack is denoted as V_{in} . Then, using Kirchhoff's voltage law, we have, the intermediate node voltage V_x as

$$V_x = V_{in} \cdot \frac{|C_F|}{|C_F| - C_D} \Rightarrow V_x > V_{in} \quad (2.9)$$

Thus, if the ferroelectric capacitor is properly designed, such that $|C_F|$ is greater than and close to C_D (capacitance matching), we get a significant voltage amplification at the intermediate node leading to $V_x > V_{in}$. In the case of a NCFET in Figure 2.9(a), C_D represents the semiconductor capacitance, as proposed in Ref. [18]. This voltage amplification phenomenon leads to steep-slope switching characteristics with subthreshold swing < 60 mV/decade. Refs. [38, 39] provide a detailed review of NCFET operation.

2.2.2 Review of salient experimental proofs for ferroelectric negative capacitance

Over the past decade, different signatures of negative capacitance have been experimentally reported. For instance, transient negative capacitance is demon-

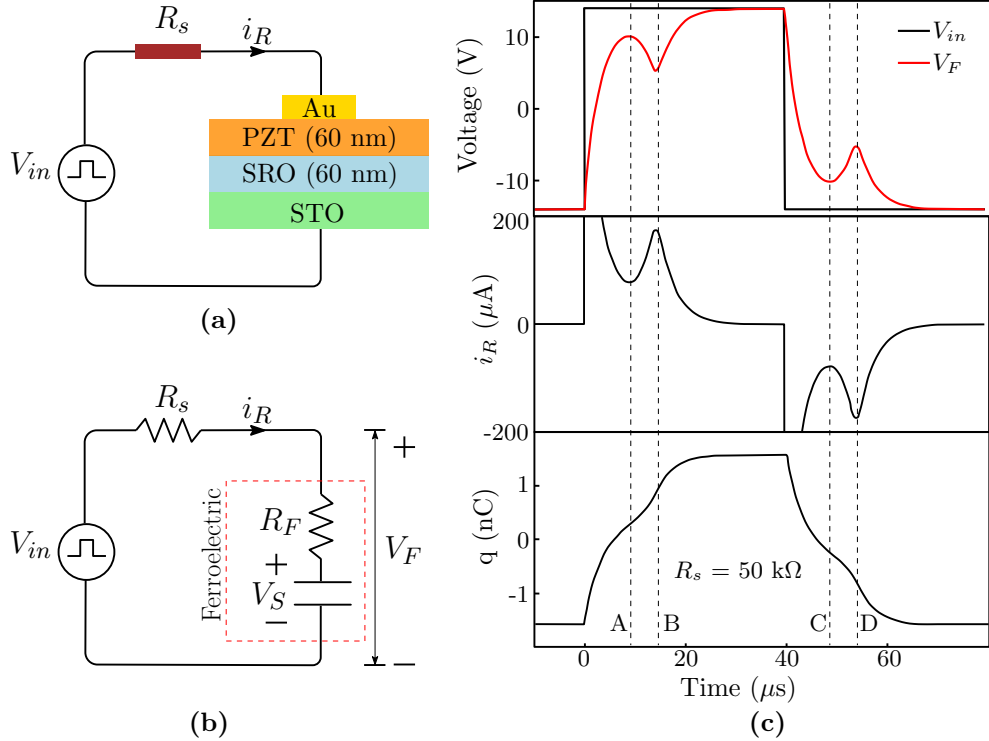


Figure 2.10: (a) Schematic diagram of the experimental setup in Ref. [31]. (b) Equivalent circuit representation. (c) Transient response reproduced from Ref. [31] showing negative capacitance during the time segments AB and CD, where dq/dV_F is negative.

strated in Khan et al. [31], by applying voltage across a series combination of ferroelectric capacitor and a resistor. The ferroelectric capacitor used is a 60 nm PZT ($\text{PbZr}_{0.2}\text{Ti}_{0.8}\text{O}_3$) grown on a metallic SrRuO_3 -buffered SrTiO_3 substrate, with gold (Au) as the top electrode. Figure 2.10(a) shows the schematic diagram of the experimental setup. The corresponding equivalent circuit representation is shown in Figure 2.10(b). The ferroelectric is modeled using the LK equation (see Eq. (2.7)) as a resistor in series with a capacitor. The resistor models the ferroelectric damping constant ρ and V_S denotes the voltage drop across the capacitor. The transient response reported in Ref. [31] is depicted in Figure 2.10(c). Note that during the time segment AB, changes in the voltage across the ferroelectric and the charge are having opposite signs. In other words, dq/dV_F is negative during time segment AB, indicating the occurrence of negative capacitance effect. The same happens during the time segment CD as well. Similar results for transient nega-

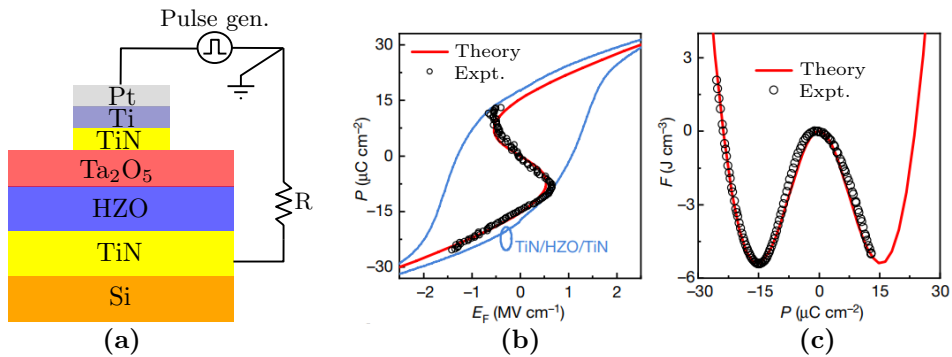


Figure 2.11: (a) Schematic diagram of the experimental setup in Ref. [43]. (b) Polarization-electric field plot reproduced from Ref. [43] capturing the S-shaped curve thereby confirming the negative capacitance effect. (c) Corresponding energy landscape plot depicting the direct relationship between negative capacitance and the double-well energy landscape. The negative capacitance effect is captured by the maxima in the energy landscape. Note that the experimental results are in good agreement with the theoretical predictions.

tive capacitance are reported for different ferroelectric materials such as polymer PVDF [40], HZO (Hafnium Zirconium Oxide) [41–43] using resistor-ferroelectric experimental setup. These results attest to the proposed idea that the ferroelectric traverses through the negative capacitance regime as it makes a transition from one stable polarization state to the other, as explained in section 2.2.1.

Hoffmann et al. [43] reports the extraction of the S-shaped polarization-electric field curve of a ferroelectric layer using electrical measurements. This enables the reconstruction of the energy landscape to confirm the direct relationship between the negative capacitance effect and the double-well energy landscape. The ferroelectric is integrated into a heterostructure forming a Metal-Ferroelectric-Insulator-Metal (MFIM) structure, as shown in Figure 2.11(a). Pulsed electrical measurement is done by applying short voltage pulses with increasing amplitude. The results reported in Ref. [43] are shown in Figure 2.11(b) and (c). The polarization-electric field plot shows the S-shaped curve indicating the presence of negative capacitance. The corresponding energy landscape is shown in Figure 2.11(c). Note that the negative capacitance effect is captured by the maxima in the energy landscape, as predicted by the Landau theory. The experimental results obtained are in good

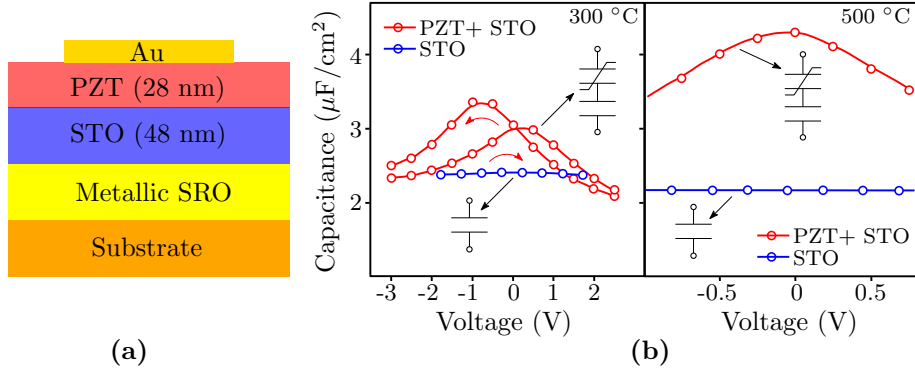


Figure 2.12: (a) Ferroelectric-dielectric stack in Ref. [44]. (b) Measured capacitances reproduced from Ref. [44], plotted as a function of voltage. Note that the capacitance of the stack is greater than the capacitance of the constituent STO dielectric, illustrating capacitance enhancement due to ferroelectric negative capacitance effect.

agreement with theoretical prediction based on the LK equation. Similar extraction of S-shaped polarization-electric field curve is also reported in Ref. [32] for silicon doped hafnium oxide (Si:HfO_2) ferroelectric material. These experiments, thus, confirm the theoretical predictions on negative capacitance based on the LK equation.

Khan et al. [44] shows steady-state negative capacitance effect through the capacitance enhancement seen in a ferroelectric-dielectric stack. When two positive capacitances are connected in series to form a stack, the equivalent capacitance of the stack will be positive (stable), but less than the individual capacitances. However, when a positive capacitance (dielectric) is connected in series to stabilize a negative capacitance (ferroelectric), the equivalent capacitance will be positive (stable) and larger than the individual capacitances. This phenomenon is called capacitance enhancement using ferroelectric negative capacitance [18]. In Ref. [44], a ferroelectric-dielectric stack is made as shown in Figure 2.12(a) using a 28 nm PZT ($\text{Pb}(\text{Zr}_{0.2}\text{Ti}_{0.8})\text{O}_3$) ferroelectric and a 48 nm STO (SrTiO_3) dielectric. The top metal and bottom metal electrodes are gold (Au) and SRO (SrRuO_3), respectively. The measured capacitance as a function of voltage is shown in Figure 2.12(b) for two different temperatures. The capacitance of the PZT-STO stack is greater than the capacitance of the constituent STO. This shows that the PZT is working as a

negative capacitor in the stack. Thus, this experiment confirms the capacitance enhancement due to ferroelectric negative capacitance. Literature also reports capacitance enhancement in a ferroelectric-dielectric stack for different ferroelectric materials such as BSTO ($\text{Ba}_{0.8}\text{Sr}_{0.2}\text{TiO}_3$) [45], BaTiO_3 [37] and PbTiO_3 [46]. The capacitance enhancement in a ferroelectric-dielectric heterostructure also leads to a steady-state charge boost, as reported in Ref. [47].

Negative capacitance effect has also been reported in different NCFETs with the ferroelectric capacitor connected externally to the transistor. For instance, Refs. [32, 48] report improved performance in a tunnel FET when a ferroelectric capacitor (PZT and Si:HfO₂) operating in negative capacitance regime is connected in series with the transistor. Ref. [49] demonstrates voltage amplification phenomenon by connecting a ferroelectric capacitor (epitaxial PZT films grown on metallic SRO buffered STO substrate with Ti/Au metal electrode) in series with a dielectric capacitor. Improved subthreshold swing is reported in Refs. [33, 50] wherein a Fin-FET is connected in series with a ferroelectric capacitor (BiFeO_3 and PZT). Similar improvement in subthreshold swing has also been reported in two-dimensional NCFET. For example, Ref. [51] shows significant reduction in the subthreshold swing when a PVDF (P(VDF_{0.75}-TrFE_{0.25})) ferroelectric capacitor is connected in series with a 2D FET with molybdenum disulfide (MoS_2) as the channel material. Improved performance has also been observed in a Metal Oxide Semiconductor Field Effect Transistor (MOSFET) with PVDF ferroelectric capacitor connected in series, as reported in Ref. [52].

2.3 REVIEW OF HYBRID MEMS ACTUATOR

As explained in Chapter 1, a novel technique to reduce the operating voltage in an electrostatic MEMS actuator is to form a hybrid MEMS actuator [17]. It consists of a ferroelectric capacitor, exhibiting negative capacitance, connected in series with the MEMS actuator, as shown in Figure 2.13(a). The equivalent circuit representation of the hybrid actuator is shown in Figure 2.13(b). The ferroelectric capacitor is denoted as C_F and the standalone MEMS actuator is modeled as a variable capacitor

C_M . The voltage drop across these capacitors are, respectively, denoted as V_F and V_M . The input to the hybrid actuator is denoted as V_{in} and the current through the circuit is i . Note that this equivalent circuit representation of the hybrid actuator is similar to the ferroelectric-dielectric stack, explained in section 2.2.1 (see Figure 2.8(a)). The difference is that the dielectric capacitor C_D is now replaced by a MEMS capacitor C_M . Thus, for an appropriately designed ferroelectric, the voltage across the MEMS actuator V_M will be greater than the input voltage V_{in} , due to the internal voltage amplification. This results in the reduction of the actuation voltage in the hybrid actuator.

At static equilibrium, we have the balance between the restoring spring force and the attractive electrostatic force. Thus, Eq. (2.1) can be re-written in terms of charge q (where $q = \int i dt$) as [17]

$$kx = \frac{q^2}{2\epsilon_0 A_M} \quad (2.10)$$

The voltage across the MEMS actuator V_M can be expressed as

$$V_M = \frac{q}{C_M} \quad (2.11)$$

where $C_M = \frac{\epsilon_0 A_M}{g_0 - x}$. Substituting the value of x from Eq. (2.10), we obtain

$$V_M = \alpha_M q - \beta_M q^3 \quad (2.12)$$

where $\alpha_M = \frac{g_0}{\epsilon_0 A_M}$ and $\beta_M = \frac{1}{2k(\epsilon_0 A_M)^2}$.

The ferroelectric capacitor is governed by the LK equation Eq. (2.6). We make a two-term approximation by neglecting the higher order term ($\gamma_F = 0$). This provides a simpler representation and is valid as the double-well energy landscape of the ferroelectric can be conveniently characterized by considering only the two terms involving α_F and β_F . Therefore, at static equilibrium, Eq. (2.7) reduces to

$$V_F = -\alpha q + \beta q^3 \quad (2.13)$$

where $\alpha = \frac{-\alpha_F t_F}{A_F}$ and $\beta = \frac{\beta_F t_F}{A_F^3}$. From Figure 2.13(b), the voltage across the hybrid actuator V_H (also equal to V_{in}) is the sum of the voltages across the ferroelectric capacitor and the MEMS capacitor. Therefore, we have,

$$V_H = V_F + V_M = (\alpha_M - \alpha)q - (\beta_M - \beta)q^3 = r_{\alpha_N} \alpha_M q - r_{\beta_N} \beta_M q^3 \quad (2.14)$$

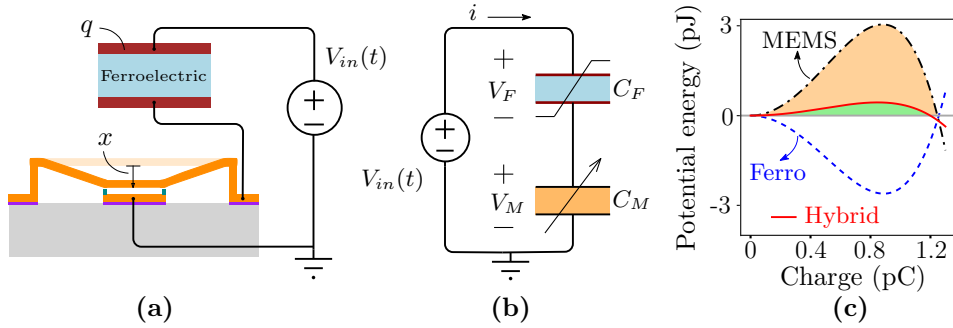


Figure 2.13: (a) Hybrid actuator formed by series connection of the ferroelectric capacitor C_F with the **MEMS** actuator. (b) Equivalent circuit representation. C_M represents the variable capacitance provided by the **MEMS** actuator. (c) Potential energy – charge landscape plotted for $V_{in} = 0$ V, depicting a lowered energy barrier (shaded green) in the hybrid actuator when compared to the **MEMS** actuator (shaded orange).

where

$$r_{\alpha N} = 1 - \frac{t_F A_M |\alpha_F| \epsilon_0}{g_0 A_F} \quad (2.15a)$$

$$r_{\beta N} = 1 - \left[(2 \beta_F k \epsilon_0^2) \left(\frac{t_F A_M^2}{A_F^3} \right) \right] \quad (2.15b)$$

Note that $r_{\alpha N}$ and $r_{\beta N}$ depend on the dimensions and material parameters of both the ferroelectric capacitor and the **MEMS** actuator.

The static pull-in voltage of the hybrid actuator V_{HSPI} and the travel range in the hybrid actuator X_{HSPI} are given by [17]

$$V_{HSPI} = r_{\alpha N} \sqrt{\frac{r_{\alpha N}}{r_{\beta N}} \cdot \frac{8 k g_0^3}{27 \epsilon_0 A_M}} = r_{\alpha N} \sqrt{\frac{r_{\alpha N}}{r_{\beta N}}} \cdot V_{SPI} \quad (2.16a)$$

$$X_{HSPI} = \frac{r_{\alpha N}}{r_{\beta N}} \cdot \frac{g_0}{3} = \frac{r_{\alpha N}}{r_{\beta N}} \cdot X_{SPI} \quad (2.16b)$$

where V_{SPI} and X_{SPI} are the static pull-in voltage and travel range of standalone **MEMS** actuator (see Eq. (2.2)). Therefore, from Eq. (2.16), we infer that the pull-in voltage in the hybrid actuator is reduced as compared to the standalone actuator, if the ferroelectric capacitor is designed such that $0 < (r_{\alpha N}, r_{\beta N}) < 1$. This condition is referred to as "effective **MEMS** mode" of operation in Ref. [17]. This condition also ensures that the hybrid actuator is stable, even though the ferroelectric capacitor is operating at the negative capacitance regime.

Table 2.3: Parameters of the ferroelectric capacitor

Parameter	Value
Ferroelectric material	HfO ₂ [38]
α_F	$-2.88 \times 10^9 \text{ m/F}$
β_F	$3.56 \times 10^{11} \text{ m}^5/\text{F/C}^2$
γ_F	$0 \text{ m}^9/\text{F/C}^4$
Ferroelectric thickness, t_F	45.24 nm
Ferroelectric area, A_F	9.87 μm^2

To design the ferroelectric capacitor for the hybrid actuator, we consider the standalone actuator discussed in section 2.1 and whose parameters are listed in Table 2.1. The effect of negative capacitance has been reported in different ferroelectric materials like PbZr_{0.2}Ti_{0.8}O₃ (PZT) [31], BiFeO₃ [33], Hafnium Zirconium Oxide (Hf_xZr_{1-x}O₂) [43, 47, 53–55], P(VDF-TrFE) [40, 56] etc. Owing to the compatibility with the existing CMOS process, Hafnium Oxide (HfO₂) based NCFETs are popular and have potential commercial significance [36]. In this work, we choose the parameters of Hafnium Oxide (HfO₂) as a typical ferroelectric, with coercive field $E_c = 1 \text{ MV/cm}$ and remanent polarization $P_r = 9 \mu\text{C/cm}^2$ [38]. Note that the essence of the analysis presented in this work does not depend on any particular choice of ferroelectric. The ferroelectric capacitor must be designed so as that the combination of the ferroelectric and MEMS capacitors is stable, satisfying the effective MEMS mode of operation [17].

We design the ferroelectric such that the hybrid actuator has a static pull-in voltage of $V_{HSPI} = 0.8 \text{ V}$ and pull-out voltage of $V_{HPO} = 0 \text{ V}$. Note that the standalone MEMS actuator has $V_{SPI} = 5.32 \text{ V}$ and $V_{PO} = 4.88 \text{ V}$ (see Table 2.2). Pull-out of the hybrid actuator at $V_{HPO} = 0 \text{ V}$ requires that the distance traveled by the movable electrode ($g_0 - h_s$) = $(r_{\alpha N}/r_{\beta N}) g_0$ [17]. Using the above equations and Eq. (2.16), we obtain the required thickness t_F and area A_F of the ferroelectric as $t_F = 45.24 \text{ nm}$ and $9.87 \mu\text{m}^2$. The parameters of the ferroelectric capacitor are

listed in Table 2.3. The comparison between the hybrid actuator and the standalone actuator is presented in Table 2.4. The ferroelectric negative capacitance effect is predicted to reduce the static pull-in voltage, pull-out voltage and travel range in the hybrid actuator, as compared to the standalone actuator.

The potential energy of the standalone actuator E_M and that of the ferroelectric capacitor E_F are given by [17]

$$E_M = \frac{1}{2}\alpha_M q^2 - \frac{1}{4}\beta_M q^4 - V_M q \quad (2.17a)$$

$$E_F = -\frac{1}{2}\alpha q^2 + \frac{1}{4}\beta q^4 - V_F q \quad (2.17b)$$

The potential energy of the hybrid actuator, $E_H = E_M + E_F$. We plot these potential energy-charge landscapes, for $V_{in} = 0$, as shown in Figure 2.13(c). Note that the energy barrier is lowered in the hybrid actuator when compared to that of the standalone MEMS actuator. This results in a lower pull-in voltage (corresponding to a lower energy barrier) in the hybrid actuator when compared to the standalone actuator.

Table 2.4: Comparison between standalone actuator and hybrid actuator. Note that the operating voltage is reduced in the hybrid actuator, as compared to the standalone actuator.

Parameter	Standalone actuator [1]	Hybrid actuator [17] (Analytical)
Static pull-in voltage	5.32 V	0.8 V
Travel range	0.67 μm	0.62 μm
Pull-out voltage	1 V	0 V

3

NUMERICAL MODELING OF HYBRID ACTUATOR

Electrostatic MEMS actuators are widely used in switching applications [7, 57]. It is hence important to study (1) the transient behavior and (2) the energy required to accomplish switching in these hybrid actuators. This involves analysis of the *dynamic response* (response to step input) of the hybrid actuators. Note that the response of electrostatic MEMS actuators to voltage excitation is different for static and dynamic inputs (see section 2.1). The former corresponds to the input voltage being varied slowly, so that the actuator is always in quasi-static equilibrium [1, 58]. The latter corresponds to the input voltage being varied suddenly, as in the case of a step voltage excitation [1, 28, 58, 59].

The *static response* (response to slowly varying input) of the hybrid actuator was analyzed in Refs. [17, 19, 60], where the operating voltage was analytically predicted to be lowered in the hybrid actuator as compared to the standalone MEMS actuator (see Section 2.3, Chapter 2). However, the analysis presented therein is valid only at static equilibrium. As a result, the *dynamic* response (response to step input) of the hybrid actuator was not studied.

It is challenging to determine the dynamics of the hybrid actuator for arbitrary voltage excitation, since the MEMS actuator [1] and ferroelectric capacitor [18] are both governed by non-linear differential equations. The dynamic response of the hybrid actuator, by coupling these differential equations, has not been analyzed in literature. Recent papers [61], [62], while investigating the impact of ferroelectric negative capacitance on the energy-delay characteristics, attempt to overcome this challenge by describing the hybrid system as a standalone MEMS actuator with modified parameters. However, they ignore the dependence of electrostatic force on displacement of the actuator while describing the force-balance equation of the system.

In this chapter, we propose a Simulation Program with Integrated Circuit Emphasis ([SPICE](#)) based multiphysics framework to model the hybrid actuators¹. We use [SPICE](#) [63] to numerically solve the coupled non-linear differential equations that describe the hybrid actuator system, thereby coupling the electromechanics of the actuator with the physics of ferroelectrics. Using this multiphysics framework, we

- investigate pull-in and pull-out voltages of the hybrid actuator to static and step input (dynamic) actuation
- study the trade-off between pull-in time and operating voltage of the hybrid actuator, and its implication on power and energy consumed from the source during the switching event
- analyze the effect of ferroelectric and [MEMS](#) damping on the dynamic response and energy consumed

We predict a significant reduction in the pull-in and pull-out voltages, and the energy consumed by the hybrid actuator as compared to the standalone [MEMS](#) actuator. We also predict that the dynamic pull-in time of the hybrid actuator is, however, larger than that of the standalone actuator. Nevertheless, we show that one can trade-off a small part of the reduction in actuation voltage to achieve identical pull-in times in the hybrid and standalone [MEMS](#) actuators, while still consuming substantially lower energy in the former as compared to the latter. The [SPICE](#) based approach leads to a model that is compatible with standard circuit simulators and can be easily used to evaluate the performance of [CMOS-MEMS](#) hybrid circuits for any kind (slow, fast, sinusoidal etc.) of voltage excitation.

¹ This work is published in Raghuram Tattamangalam Raman, Arvind Ajoy, "SPICE-Based Multiphysics Model to Analyze the Dynamics of Ferroelectric Negative-Capacitance-Electrostatic MEMS Hybrid Actuators," IEEE Trans. Electron Devices, vol. 67, no. 11, pp. 5174-5181, Nov. 2020, doi:10.1109/TED.2020.3019991.

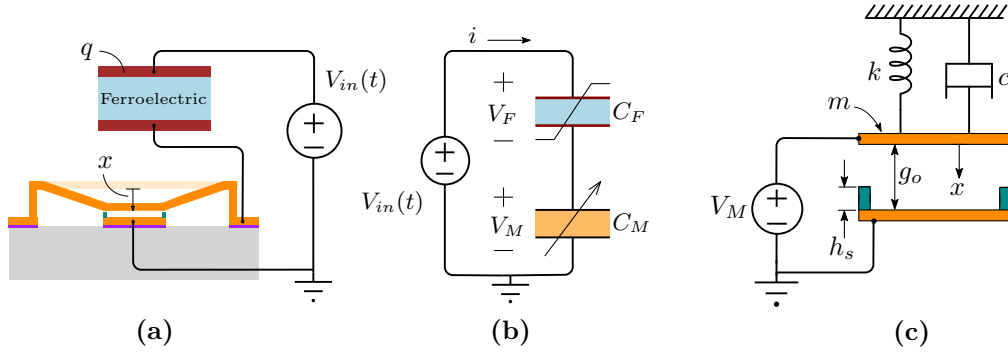


Figure 3.1: (a) Hybrid actuator formed by series connection of the ferroelectric capacitor C_F with the **MEMS** actuator. (b) Equivalent circuit representation. C_M represents the variable capacitance provided by the **MEMS** actuator. (c) 1-DOF model of the standalone **MEMS** actuator.

3.1 MODELING THE HYBRID ACTUATOR IN SPICE

For the hybrid actuator shown in Figures 3.1(a),(b), the input to the hybrid actuator is denoted as V_{in} , while the voltage drops across the ferroelectric and **MEMS** actuator are represented as V_F and V_M , respectively. Based on Section 2.1 in Chapter 2, the 1-DOF model of the **MEMS** actuator is shown in Figure 3.1(c). The parameters of the 1-DOF model have the same definitions as described in Section 2.1 in Chapter 2. The design of the hybrid actuator follows Section 2.3 in Chapter 2 to obtain a static pull-in voltage of 0.8 V and a pull-out voltage of 0 V. The parameters of the hybrid actuator are summarized in Table 3.1. The equation of motion governing the standalone actuator (see Figure 3.1(c)) is given by [1]

$$m \frac{d^2x}{dt^2} + c \frac{dx}{dt} + k x = \frac{\epsilon_0 A_M V_M^2}{2(g_o - x)^2} \quad (3.1)$$

where m is the mass, c is the damping coefficient, k is the spring constant, A_M is the actuation area, g_o is the air-gap, ϵ_0 is the permittivity of free space, V_M is the voltage across the **MEMS** actuator and the variable x denotes the displacement of the movable electrode. The standalone electrostatic **MEMS** actuator is modeled as a variable capacitor C_M , as shown in Figure 3.2(a). The sub-circuit based SPICE implementation of the standalone **MEMS** actuator follows Refs. [65],[27]. The SPICE model consists of different modules that are represented as sub-circuits in the

Table 3.1: Parameters of the hybrid actuator used in this work. This consolidates the parameters of the MEMS actuator from Table 2.1 and the parameters of the ferroelectric from Table 2.3.

Parameter	Value
Beam material	Gold (Au) [3]
Length of the beam, L	140 μm
Width of the beam, W	120 μm
Actuation area, A_M	$1.44 \times 10^{-8} \text{ m}^2$
Young's modulus, E	78 GPa
Density, D	19280 kg/m^3
Mass, $m = 0.35 \times D \times \text{volume}$	$5.6 \times 10^{-11} \text{ kg}$ [7]
Width of the support, w_S	20 μm
Length of the support, l_S	80 μm
Thickness, T	0.5 μm
Spring constant, $k = 4Ew_s(\frac{T}{l_s})^3$	1.52 N/m [7]
Initial air-gap, g_0	2 μm
Stopper height, h_s	0.15 μm
Area of contact, A_C	16 μm^2 [64]
Permittivity of free space, ϵ_0	$8.854 \times 10^{-12} \text{ F/m}$
Ferroelectric material	HfO ₂ [38]
α_F	$-2.88 \times 10^9 \text{ m/F}$
β_F	$3.56 \times 10^{11} \text{ m}^5/\text{F/C}^2$
γ_F	$0 \text{ m}^9/\text{F/C}^4$
Ferroelectric thickness, t_F	45.24 nm
Ferroelectric area, A_F	9.87 μm^2

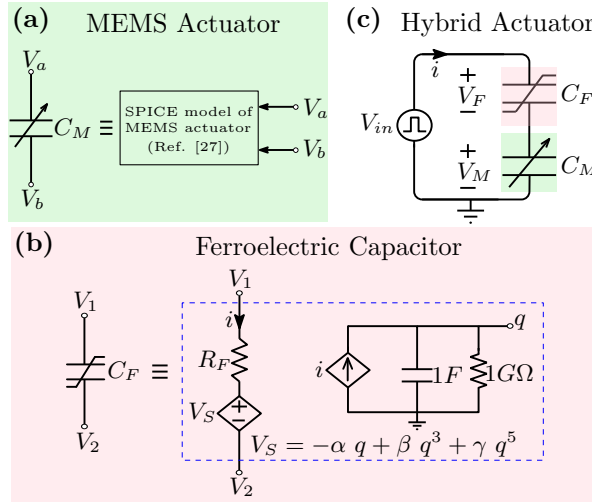


Figure 3.2: (a) Standalone electrostatic MEMS actuator modeled as a variable capacitor C_M . SPICE implementation follows Ref. [27]. (b) SPICE model of ferroelectric capacitor C_F . Charge q (represented as a voltage) is determined using an RC integrator. The voltage source V_S is implemented using an arbitrary behavioral voltage source in SPICE. (c) Equivalent circuit representation of hybrid actuator.

circuit simulator. The SPICE model of the standalone actuator solves the governing differential equation (Eq. (3.1)). The implementation of the SPICE model of the standalone actuator in the circuit simulator is detailed in the Appendix, at the end of the thesis.

The dynamics of the ferroelectric capacitor (single domain) is captured by the time dependent Landau-Khalatnikov (LK) equation [18, 31, 66] relating the voltage V_F across the ferroelectric to the charge q and is given by

$$V_F = -\alpha q + \beta q^3 + \gamma q^5 + R_F \frac{dq}{dt} \quad (3.2)$$

$$\alpha = -\frac{\alpha_F t_F}{A_F}; \beta = \frac{\beta_F t_F}{A_F^3}; \gamma = \frac{\gamma_F t_F}{A_F^5}; R_F = \frac{\rho t_F}{A_F} \quad (3.3)$$

where ρ is the ferroelectric damping constant; α_F , β_F and γ_F are ferroelectric anisotropy coefficients, t_F , A_F are respectively the thickness and area of the ferroelectric. The last term of Eq. (3.2) denotes the voltage drop across resistor R_F with dq/dt representing the current i through it. Thus, Eq. (3.2) is implemented as a Voltage Controlled Voltage Source (VCVS) in series with resistor R_F [66], leading to the SPICE model of the ferroelectric capacitor as shown in Figure 3.2(b). The charge

q (represented as a voltage) is estimated by integrating the current i through the capacitor [67].

We construct the SPICE model for the hybrid actuator by cascading the sub-circuit corresponding to the ferroelectric capacitor C_F with that of the standalone MEMS actuator C_M as shown in Figure 3.2(c). This solves the differential equations Eqs. (3.1, 3.2) simultaneously, by ensuring that an identical charge exists on the ferroelectric capacitor and the MEMS actuator. The SPICE netlist of the hybrid actuator is given in the Appendix, at the end of the thesis. We have also released the detailed implementation and netlist of the hybrid actuator online at IEEE DataPort [68].

3.2 SIMULATION RESULTS AND DISCUSSION

3.2.1 Static response of the actuator

This section verifies our model of the hybrid actuator by studying its static response, and explains the physics of voltage amplification due to the ferroelectric negative capacitance. The static response is obtained by applying a *slowly varying input* (with $t_{inp} = 80$ ms) to the actuator. The static pull-in and pull-out characteristics of the hybrid actuator are shown in Figure 3.3. The simulation results are in agreement with the analytical results given in Ref. [17], thus validating the hybrid actuator model. Note that the static pull-in and pull-out voltages are significantly reduced in the hybrid actuator, compared to the standalone actuator. This is due to the voltage amplification provided by the ferroelectric negative capacitance [17, 19, 60].

In order to better visualize the reduction in actuation voltage, we plot the different voltages in the hybrid actuator as a function of time in Figure 3.4(a). Although the input voltage V_{in} is positive, note that the voltage across the ferroelectric V_F is negative. Thus, the voltage across the MEMS, V_M is larger than the applied voltage V_{in} , as shown in Figure 3.4(a). This voltage amplification results in a significantly lower pull-in voltage in the hybrid MEMS actuator as compared to the standalone

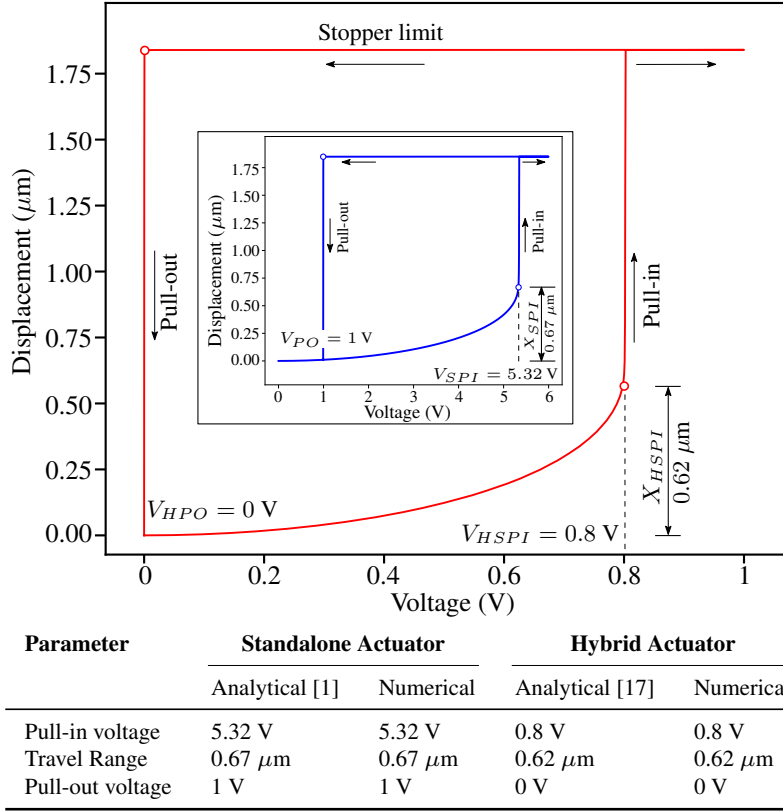


Figure 3.3: Static pull-in and pull-out characteristics of the hybrid actuator. The simulation results are in agreement with the analytical results given in Ref. [17], thus validating the hybrid actuator model. Inset shows the static characteristics of standalone actuator. Note that the static pull-in and pull-out voltages are reduced in the hybrid actuator due to the ferroelectric negative capacitance.

MEMS actuator. This phenomenon is similar to the voltage amplification in NCFETs [18], where the gate voltage is amplified, leading to steep-slope switching characteristics (sub-threshold swing < 60 mV/decade). Figure 3.4(b) shows the charge q , as a function of the input voltage V_{in} , and voltage across ferroelectric V_F , all extracted from our simulation. The charge is obtained at output of the $1F \parallel 1G\Omega$ integrator in Figure 3.2(b). Note that the slope of the $q - V_F$ plot is negative, confirming that the ferroelectric operates in the negative capacitance regime to achieve the above mentioned voltage amplification. Also note that the extracted $q - V_F$ characteristics exactly match with those obtained from the LK equation described in Eq. (3.2), confirming that the behavior of the ferroelectric has been captured correctly.

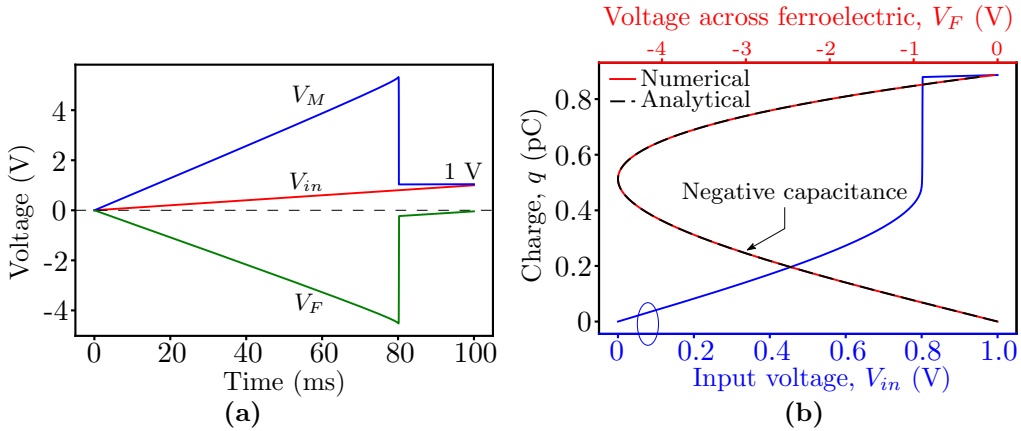


Figure 3.4: (a) Slow input voltage V_{in} , voltage across the **MEMS** V_M , and voltage across ferroelectric V_F plotted as a function of time. The ferroelectric negative capacitance causes amplification of the applied voltage V_{in} across the **MEMS**, thereby achieving pull-in at a much lower voltage compared to the standalone **MEMS** actuator. (b) Charge q plotted as a function of V_{in} and V_F , depicting the use of negative capacitance regime of the ferroelectric to achieve voltage amplification. The extracted $q - V_F$ characteristics exactly match with those obtained from the **LK** equation described in Eq. (3.2).

3.2.2 Dynamic response of the actuator

In this section, we study the dynamic response (response to step input) of the hybrid actuator. The dynamic response of the standalone actuator was described in Section 2.1 in Chapter 2. We had obtained a dynamic pull-in voltage V_{DPI} of 4.88 V and a dynamic pull-in displacement X_{DPI} of 1 μm (see Figure 2.4 and Table 2.2) for the standalone actuator. The dynamic response of the hybrid actuator (with $\rho = 0$) for a step input voltage (with $t_{inp} = 1 \text{ ps}$) is shown in Figure 3.5. The simulation results give a hybrid dynamic pull-in voltage V_{HDPI} of 0.69 V, hybrid dynamic pull-in displacement X_{HDPI} of 1.01 μm and a pull-out voltage V_{HPO} of 0 V. Our simulation method thus enables a view of the transient response (input vs. time, displacement vs. time) before and after pull-in, and before and after pull-out as shown in Figure 3.5. Compared to the standalone **MEMS** actuator, there is a significant reduction in the dynamic operating voltage of the hybrid actuator. As in the case of static response, this is because of the voltage amplification

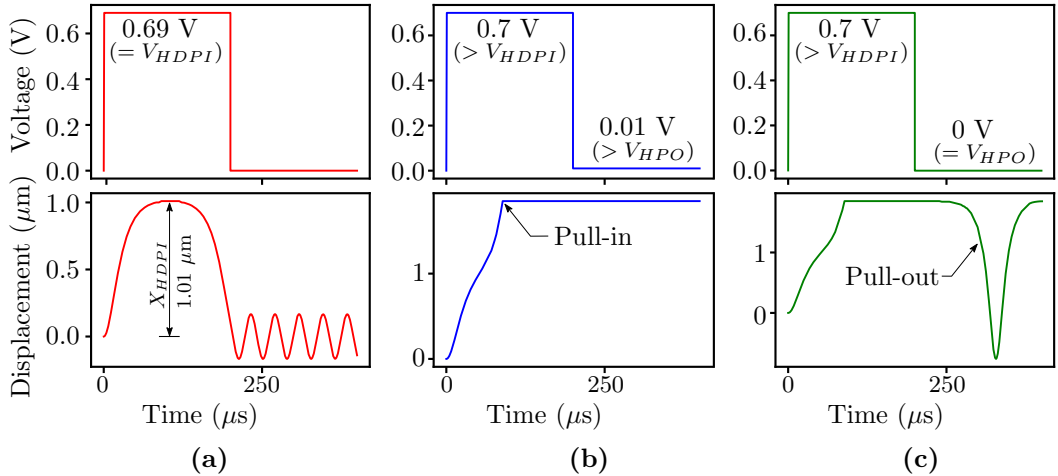


Figure 3.5: (a) Hybrid actuator response before dynamic pull-in, with a dynamic pull-in displacement $X_{HDPI} = 1.01 \mu\text{m}$. (b) Hybrid actuator response after dynamic pull-in and without pull-out. (c) Hybrid actuator response after dynamic pull-in and with pull-out. Note that the pull-in voltage is reduced to $V_{HDPI} = 0.69 \text{ V}$ and pull-out voltage is reduced to $V_{HPO} = 0 \text{ V}$.

due to the negative capacitance of the series ferroelectric capacitor. The sub-1V operation of the hybrid actuator, depicted in Figure 3.5 should drive research into devising techniques to integrate such hybrid actuators with modern low-voltage CMOS devices, eliminating the need for drive electronics or additional on-chip voltage up-converters. Note however that achieving a good match [69, 70] between the standalone MEMS capacitance C_M and ferroelectric capacitance C_F will be experimentally challenging, since both these capacitances are non-linear and bias dependent. Similar to NCFETs [71], the voltage amplification in the hybrid actuator requires $|C_F| \sim C_M$. However, variation in the ferroelectric thickness t_F changes C_F and this affects the operating voltage. Figure 3.6 shows the effect of t_F on V_{HDPI} and V_{HPO} . Increase in t_F reduces the dynamic operating voltage. This is due to the reduction in the ferroelectric capacitance, leading to an enhanced voltage amplification. A similar trend is observed for the gate voltage in NCFETs [66]. Both $r_{\alpha N}$ and $r_{\beta N}$ in Eq. (2.15) should be positive for “effective MEMS mode”

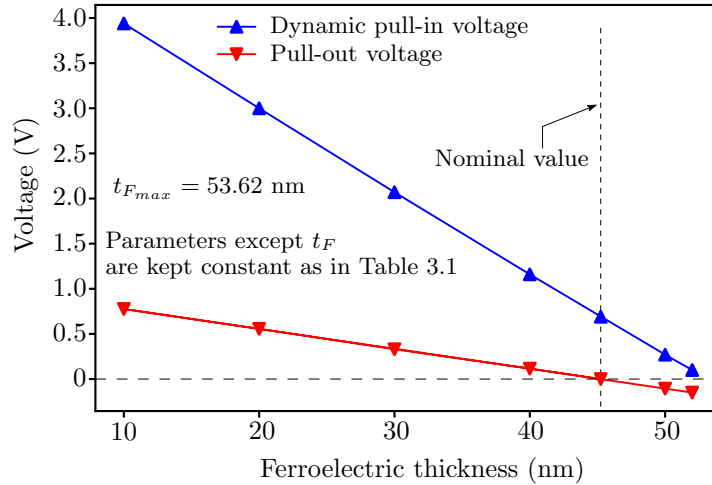


Figure 3.6: Effect of ferroelectric thickness t_F on the dynamic pull-in (V_{HDPI}) and pull-out (V_{HPO}) voltage of the hybrid actuator. Nominal value corresponds to the parameters in Table 3.1. The operating voltage decreases with increase in t_F .

of operation (see Section 2.3 in Chapter 2). Thus, the upper limit of t_F is bounded by $t_{F_{max}}$, given by

$$t_{F_{max}} = \min \left\{ \frac{g_o A_F}{A_M |\alpha_F| \epsilon_o}, \frac{A_F^3}{2\beta_F k(\epsilon_o A_M)^2} \right\} = 53.62 \text{ nm} \quad (3.4)$$

A proper choice of t_F is therefore necessary to ensure voltage amplification.

Note that V_{HPO} can be either positive or negative, as shown in Figure 3.6. Negative V_{HPO} allows for bipolar voltage actuation, which improves reliability [72] and is also used in memory applications [73]. However, this requires both positive and negative power supplies for operation. Tailoring t_F can ensure positive V_{HPO} , facilitating the use of single sub-1V voltage source for both pull-in and pull-out. For example, the hybrid actuator with $t_F = 50$ nm has a negative V_{HPO} (-0.106 V), which implies that a reduction of the applied voltage to 0 V will not result in pull-out. However, a small change in thickness to 40 nm (with $V_{HPO} = 0.115$ V) will ensure pull-out of the beam at 0 V.

The proposed SPICE model can be used to study the effect of variation in the MEMS parameters, for example, on the dynamic pull-in voltage V_{HDPI} . Variation in geometric and material properties are inevitable. For example, even with standardized fabrication technology, nearly 20% deviation in gap g_o is reported [74]. Similarly, deviation in spring constant k arises due to variation in geometric

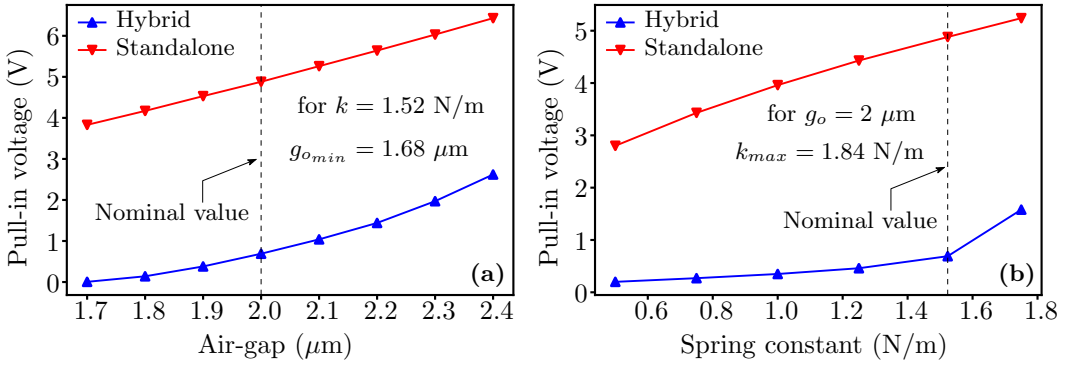


Figure 3.7: Effect of variation in air-gap g_o and spring constant k on the dynamic pull-in voltage in standalone and hybrid actuators. Nominal value corresponds to the parameters in Table 3.1. Pull-in voltage increases with increase in g_o and k . However, for each case, the pull-in voltage is lower in the hybrid actuator, as compared to the standalone actuator.

(length, width, thickness) and material (Young's modulus) properties [74]. Figures 3.7(a),(b) capture the effect of variation in g_o and k on the dynamic pull-in voltage. Since $r_{\alpha N}$ and $r_{\beta N}$ should both be positive for "effective MEMS mode" of operation [17] (see Section 2.3 in Chapter 2), there exists a minimum limit in g_o (minimum g_o is limited by $r_{\alpha N}$ as $r_{\alpha N} > 0$) and a maximum limit in k (maximum k is limited by $r_{\beta N}$ as $r_{\beta N} > 0$). They are given by,

$$g_{o_{min}} = (t_F A_M |\alpha_F| \epsilon_o) / A_F \equiv 1.68 \mu\text{m} \quad (3.5a)$$

$$k_{max} = A_F^3 / (2\beta_F t_F \epsilon_o^2 A_M^2) \equiv 1.84 \text{ N/m} \quad (3.5b)$$

V_{HDPi} increases with increase in g_o and k . However, for each case, the pull-in voltage is lower in the hybrid actuator, as compared to the standalone actuator.

3.2.3 Impact of ferroelectric damping on the transient response during pull-in

Thus far, we have neglected all forms of damping, both in the MEMS actuator and in the ferroelectric capacitor. In this section, we analyze the impact of ferroelectric damping constant ρ (see Figure 3.2(b)). Note that MEMS damping c is still assumed to be zero. The transient response during dynamic pull-in of the the hybrid actuator is shown in Figure 3.8, for different values of ferroelectric damping. The

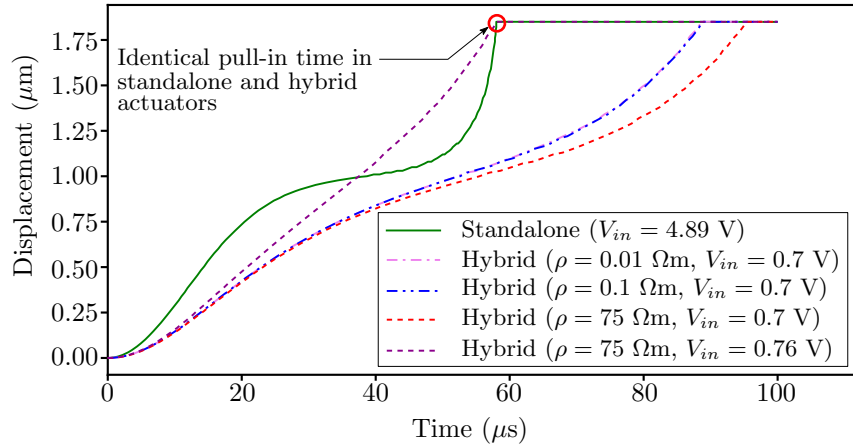


Figure 3.8: Dynamic pull-in time analysis of hybrid actuator (for different ρ) compared with that of the standalone MEMS actuator. The hybrid actuator is slower in comparison with the standalone MEMS actuator to achieve dynamic pull-in. There also exists a trade-off between the applied step voltage and the pull-in time, as depicted by the red and purple dashed lines.

ferroelectric damping, modeled by the resistance $R_F = \rho t_F / A_F$, plays an important role in the time response of the hybrid actuator. A large range of ρ [from 0.01 to 75 Ωm] is used in the simulation for a comprehensive prognosis. The release process is not plotted, since a displacement by a few nanometers is sufficient for the electrode to be considered as released. Since the pull-in voltage is a function of ρ , a step input voltage 10 mV greater than the dynamic pull-in voltage (corresponding to each value of ρ) is used for actuation to ensure pull-in.

It is observed that the hybrid actuator is slower in comparison with the standalone MEMS actuator. As ferroelectric damping increases, the pull-in voltage moves from the ideal dynamic pull-in voltage (without damping) to the static pull-in voltage value. This trend is similar to the effect of MEMS damping on dynamic pull-in voltage in standalone MEMS actuators [28, 75]. Also, note that there is a trade-off between the applied step input voltage and the pull-in time – a larger step input voltage will result in faster pull-in of the actuator. This suggests that, by applying a higher step voltage (which is still smaller than that of the standalone actuator), the pull-in time of the hybrid actuator can be made equal to the pull-in time of the standalone actuator. This ensures low-voltage operation of the hybrid actuator

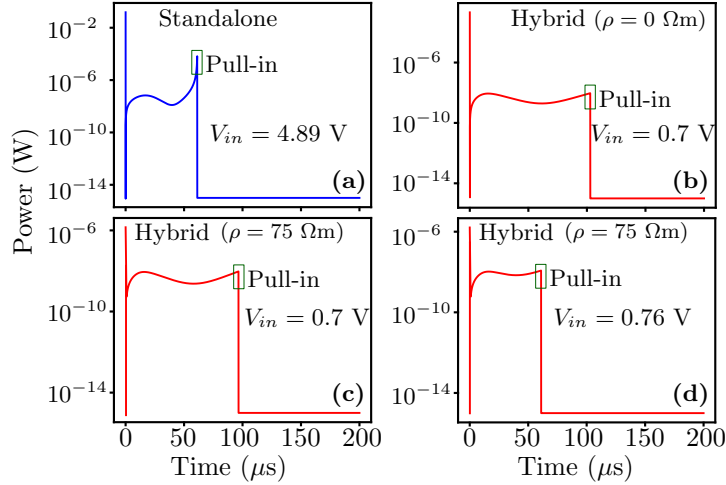


Figure 3.9: Instantaneous power consumption during dynamic pull-in in (a) standalone actuator for $V_{in} = 4.89$ V, (b) hybrid actuator ($\rho = 0 \Omega\text{m}$ and $V_{in} = 0.7$ V), (c) hybrid actuator with $\rho = 75 \Omega\text{m}$ with input $V_{in} = 0.7$ V and (d) hybrid actuator with $\rho = 75 \Omega\text{m}$ with input $V_{in} = 0.76$ V. The higher actuation voltage $V_{in} = 0.76$ V ensures identical pull-in time as compared to the standalone actuator. Compared to standalone MEMS actuator, the hybrid actuator shows significantly lower power consumption even when operated at $V_{in} = 0.76$ V.

without compromising on the pull-in time. For example, the hybrid actuator with $\rho = 75 \Omega\text{m}$ has the same pull-in time as the standalone MEMS actuator, when actuated with a step input voltage $V_{in} = 0.76$ V, as depicted in Figure 3.8.

3.2.4 Implication on power and energy consumption during dynamic pull-in

We estimate the instantaneous power consumed from the voltage source during dynamic pull-in as $V_{in}(t) \cdot i(t)$, for the standalone MEMS actuator and the hybrid MEMS actuator. As in the case of transient analysis, we apply a step voltage 10 mV larger than the dynamic pull-in voltage, in each case, to ensure pull-in. Figure 3.9 shows the power consumption in the standalone MEMS actuator and the hybrid MEMS actuator. Figures 3.9(a),(b) depict lower power consumption in the hybrid MEMS actuator (with $\rho = 0$ and $V_{in} = 0.7$ V) as compared to the standalone MEMS actuator. This is found to be true, even when the hybrid actuator operates at a higher voltage to achieve the same pull-in time as the standalone actuator. For

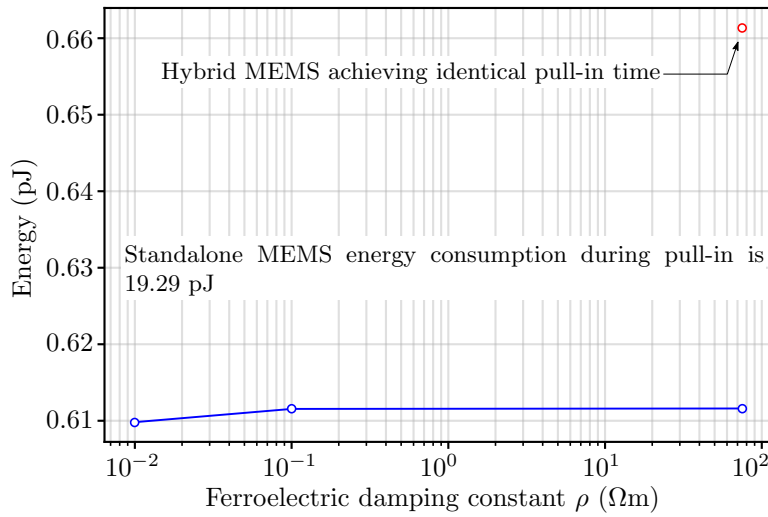


Figure 3.10: Effect of ferroelectric damping constant ρ on the energy consumption during dynamic pull-in in the hybrid actuator. Note that there is reduction in the energy consumption in comparison with the standalone **MEMS** actuator due to reduction in the dynamic pull-in voltage.

instance, Figures 3.9(c),(d) show the instantaneous power consumed in the hybrid **MEMS** with ferroelectric damping constant $\rho = 75 \Omega\text{m}$ for two inputs: $V_{\text{in}} = 0.7 \text{ V}$ and $V_{\text{in}} = 0.76 \text{ V}$. We find that, the hybrid **MEMS** actuator with $\rho = 75 \Omega\text{m}$ and $V_{\text{in}} = 0.76 \text{ V}$, having the same pull-in time as in standalone **MEMS** actuator, has significantly lower power consumption when compared with the standalone **MEMS** actuator. This favors the prospects of using such hybrid actuators in low-power, low-voltage applications.

We now calculate the energy consumed from the source, during dynamic pull-in, as the time integral of the instantaneous power $V_{\text{in}}(t) \cdot i(t)$ over the entire pull-in time [76]. Figure 3.10 shows the results of the above calculation. Again, ferroelectric damping constant ρ plays an important role. Note that the energy consumed for dynamic pull-in in the standalone **MEMS** actuator is 19.29 pJ. The energy consumed for dynamic pull-in in the hybrid actuator for different values of ρ varies between 0.6 – 0.7 pJ. For example, for $\rho = 75 \Omega\text{m}$, the energy consumed for pull-in is 0.61 pJ. This shows a $\sim 32 \times$ reduction in the energy consumption using the hybrid actuator. However, this reduction in energy comes at the cost of slower pull-in. In the previous section, we showed that the actuator can be operated using a

Table 3.2: Effect of MEMS damping ratio ζ on the energy consumed during dynamic pull-in.

ζ	Standalone Actuator		Hybrid Actuator ($\rho = 75 \Omega\text{m}$)
	With min. V_{in} for pull-in	With min. V_{in} for pull-in	With V_{in} for achieving identical pull-in time*
0	19.29 pJ	0.61 pJ	0.67 pJ
0.1	20.81 pJ	0.67 pJ	0.78 pJ
1	22.96 pJ	0.69 pJ	0.73 pJ
10	23.01 pJ	0.69 pJ	0.73 pJ

* same pull-in time as standalone actuator.

voltage higher than pull-in voltage to achieve a pull-in time identical to that of the standalone MEMS actuator. Figure 3.10 also shows the energy consumption when the hybrid actuator with $\rho = 75 \Omega\text{m}$ is actuated with a step voltage $V_{in} = 0.76 \text{ V}$ (to achieve identical pull-in time as standalone actuator). We find that the energy consumed is still $\sim 29 \times$ lower than the energy consumed in the standalone actuator, indicating a very favorable application of the trade-off between pull-in time and applied voltage. This trend is in agreement with the theoretical predictions in Ref. [61] (with $\rho = 0$) and Ref. [62] (with constant ferroelectric switching delay), where the hybrid actuator has lower switching energy than the standalone actuator at the same switching time.

3.2.5 Effect of MEMS damping on energy consumption during dynamic pull-in

Note that we have neglected the MEMS damping coefficient c in our analysis so far. We now estimate the energy consumed during switching taking into account the MEMS damping coefficient c (see Figure 3.1(c)). We again compare the energy consumed between the standalone actuator and the hybrid actuator with ferroelectric damping constant $\rho = 75 \Omega\text{m}$. We calculate the MEMS damping coefficient as $c = 2m\omega_o\zeta$, where $\omega_o = \sqrt{k/m}$ is the natural frequency and ζ is the damping

ratio of the mechanical **MEMS** beam structure. Based on Ref. [77], we use ζ value as 0.1, 1 and 10 in our simulations, corresponding to underdamped, critically damped and over damped conditions of the **MEMS**, respectively. The results are summarized in Table 3.2. As in the case of transient analysis, minimum input voltage V_{in} implies 10 mV larger than the dynamic pull-in voltage, in each case, to ensure pull-in. The energy consumed in the hybrid actuator is still significantly lower than that in the standalone actuator, with the inclusion of **MEMS** damping coefficient c . The above observations holds true even for the case when the hybrid actuator achieves identical pull-in time as the standalone **MEMS** actuator. For example, with $\zeta = 10$, we predict a $\sim 32 \times$ reduction in energy consumed. This shows that the trade-off between pull-in time and applied voltage in the hybrid actuator is still favorable, even in the presence of **MEMS** damping. Thus, compared to a standalone **MEMS** actuator, we find an overall benefit in the energy consumed for actuation in the hybrid actuator.

3.3 SUMMARY

We presented a **SPICE** based framework to model hybrid **MEMS** actuators and to analyze their static and dynamic (step input) responses. It is shown that both the static and dynamic pull-in and pull-out voltages of this hybrid actuator are significantly reduced due to the presence of the series ferroelectric capacitor exhibiting negative capacitance. During dynamic pull-in, there is considerable reduction in the power and energy consumed in the hybrid actuator as compared to the standalone **MEMS** actuator, accompanied however by an increase in pull-in time. Even so, by using a voltage higher than the pull-in voltage, we can achieve identical pull-in times for the hybrid and standalone actuators and still achieve reduction in the energy consumed in the hybrid actuator. This favorable application of the trade-off between pull-in time and applied voltage, resulting in an overall benefit in pull-in time and energy consumption, holds good in the presence of both ferroelectric and **MEMS** damping. This motivates the use of such actuators in low-power, low-voltage switching applications. This should also motivate research

into novel techniques to fabricate and integrate such hybrid actuators with modern CMOS devices. Finally, since the proposed model is SPICE based and thus circuit compatible, our approach can be used in combination with other low-voltage CMOS circuits to analyze various heterogeneous CMOS - MEMS systems.

4

CHARGE BASED DESCRIPTION OF STANDALONE AND HYBRID MEMS ACTUATORS

Although the numerical model described in Chapter 3 analyzes the static and dynamic response, it provides very limited physical insight into the response of the hybrid actuator. A convenient method to analyze pull-in instability in electrostatic MEMS is to use energy landscape [20, 78–81]. To analyze the hybrid actuator based on energy landscape, it is suitable to describe both the ferroelectric and the MEMS actuator in terms of a common entity. However, the MEMS actuator is described in terms of displacement (Eq. (3.1)) and the ferroelectric is described in terms of charge (Eq. (3.2)). In the hybrid actuator, since both the ferroelectric and the MEMS actuator are in series, they share the same charge. Hence, in this chapter, we develop a framework to analyze the hybrid actuator, using charge as the common variable. We first use a mapping function that transforms displacement into charge, to formulate the Hamiltonian of the standalone actuator in terms of charge¹. Then, the energy associated with the ferroelectric is added to the Hamiltonian of the standalone actuator, to obtain the Hamiltonian of the hybrid actuator, expressed in terms of charge. Thus, the response of the hybrid actuator to static and dynamic (step) inputs is analyzed graphically, using its energy-charge and phase-portrait (charge vs. current) plots. The mapping function derived in this chapter is also be used to analyze the hybrid actuator using its energy-displacement landscape, as explained later in Chapter 5. Although displacement is the conventional variable used to describe the electrostatic actuators, analysis in terms of charge offers some advantages. For instance, in the standalone actuator, we derive the analytical

¹ A part of this chapter is published in Raghuram Tattamangalam Raman, Arvind Ajoy, Revathy Padmanabhan, "Analysis of Electrostatic MEMS Using Energy-Charge Landscape," IEEE Trans. Electron Devices, vol. 67, no. 10, pp. 4413–4420, Oct. 2020, doi:10.1109/TED.2020.3018700.

expressions for the voltage and charge under static and dynamic conditions, based on charge. Further, we put forward a procedure to estimate various parameters of the standalone actuator, based on the proposed method.

4.1 HAMILTONIAN OF THE STANDALONE ACTUATOR

We consider the clamped-clamped beam as described in Section 2.1 in Chapter 2, whose parameters are listed in Table 2.1.

The Hamiltonian (total energy) H_M of the 1-DOF electrostatic MEMS actuator, driven by a voltage source, neglecting damping, is given by [79, 80]

$$H_M(x, \dot{x}, t) = \frac{1}{2} m \dot{x}^2 + \frac{1}{2} k x^2 - \frac{1}{2} \frac{\epsilon_0 A_M V_M^2(t)}{(g_o - x)} \quad (4.1)$$

The first term represents the kinetic energy with $\dot{x} = \frac{dx}{dt}$ denoting the velocity. The second and third terms represent the potential energy stored in the spring and in the capacitor formed by the top and bottom electrodes respectively. The negative sign in the third term is due to the energy lost by the voltage source in charging the parallel plate capacitor. Now, we employ a coordinate transformation from displacement to charge. Since the electrostatic MEMS actuator resembles a parallel-plate capacitor, the charge q on the electrode can be related to the displacement x of the electrode as

$$q = \frac{\epsilon_0 A_M V_M(t)}{(g_o - x)} \quad (4.2)$$

Therefore, H_M is obtained as a function of charge q as

$$H_M(q, \dot{q}, t) = \frac{1}{2} m \left(\frac{\epsilon_0 A_M V_M(t)}{q^2} \right)^2 \dot{q}^2 + U_M(q, t) \quad (4.3)$$

where $\dot{q} = \frac{dq}{dt}$ is the current. The first term represents the kinetic energy. The second term denotes the potential energy of the spring and the parallel plate variable capacitor, expressed in the charge coordinate as

$$U_M(q, t) = \frac{1}{2} k \left(g_o - \frac{\epsilon_0 A_M V_M(t)}{q} \right)^2 - \frac{q V_M(t)}{2} \quad (4.4)$$

Note that Eq. (4.3) describes the energy of the electrostatic MEMS actuator for *any* form of voltage actuation $V_M(t)$. We would like to reiterate that the expression for

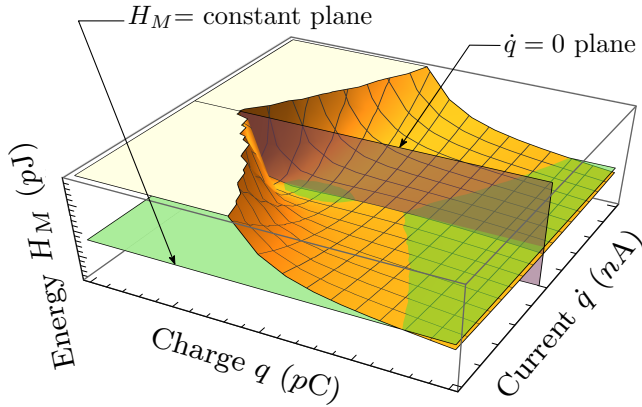


Figure 4.1: Total energy (H_M) plotted as a function of charge (q) and current (\dot{q}) for an input voltage V_M . Projection on the plane $\dot{q} = 0$ gives the potential energy-charge plot, as shown in Figure 4.2(a). Projection on the plane $H_M = \text{constant}$ gives the phase plane plot, as shown in Figure 4.3(d).

energy derived in Ref. [17] is valid *only* at points of static equilibrium, because, the mapping from displacement to charge used therein is obtained by equating the electrostatic force of attraction between the two electrodes and the mechanical spring restoring force, which is valid only at points of static equilibrium. On the other hand, the mapping Eq. (4.2), used to obtain Eq. (4.3), describes the charge-voltage relationship of a parallel plate capacitor, and is valid for *any* voltage $V_M(t)$.

4.2 ANALYSIS OF STANDALONE ACTUATOR USING ENERGY-CHARGE LANDSCAPE

4.2.1 Static pull-in

At any given time t , let the amplitude of the input voltage be V_M . The total energy (H_M) as a function of charge (q) and current (\dot{q}) for an input voltage V_M is plotted in Figure 4.1. In order to find the static equilibria of the system, the time derivatives

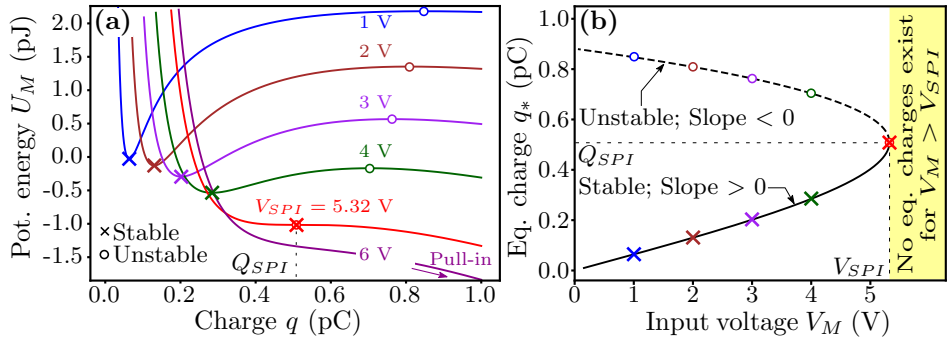


Figure 4.2: (a) Potential energy (U_M) - charge (q) plot for different input voltages. The stable and unstable equilibrium charges coincide at the static pull-in charge Q_{SPI} , where input voltage V_M equals static pull-in voltage V_{SPI} . (b) Equilibrium charge (q_*) - input voltage (V_M) plot. The stable (unstable) equilibrium charges lie on the plot where the slope is positive (negative). No equilibrium charges exist for $V_M > V_{SPI}$, resulting in static pull-in.

should be set to zero. Thus, the total energy H_M reduces to the potential energy U_M . In Figure 4.1, this corresponds to the projection of the total energy on the plane where $\dot{q} = 0$. By doing so, we obtain the potential energy (U_M) - charge (q) landscape for the applied voltage as shown in Figure 4.2(a). The static equilibria correspond to $dU_M/dq = 0$. For each applied voltage, there are two equilibrium charges: stable (local minima with $d^2U_M/dq^2 > 0$) and unstable (local maxima with $d^2U_M/dq^2 < 0$). The stable and unstable equilibrium charges are denoted by the cross (\times) and circle (\circ) markers respectively. For an input voltage V_M , the displacement of the top electrode settles at a position corresponding to the energetically favorable stable equilibrium charge. With increase in V_M , the stable and unstable equilibrium charges become more closely spaced in the energy-charge landscape, eventually coinciding with each other. Beyond the static pull-in voltage $V_{SPI} = 5.32$ V, there exists no stable equilibrium charge. We define the charge corresponding to this voltage as the static pull-in charge Q_{SPI} , as shown in Figure 4.2(a). Using Eq. (4.2), the charge $Q_{SPI} = 0.51$ pC corresponds to a travel range of $X_{SPI} = g_o/3 = 0.67$ μm (see Figure 2.3 in Chapter 2). Thus, beyond V_{SPI} , the top electrode snaps down onto the bottom electrode.

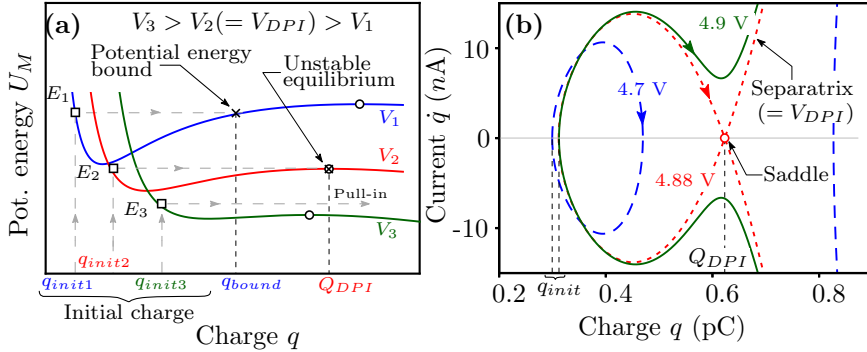


Figure 4.3: (a) Illustration of dynamic pull-in using potential energy (U_M) - charge (q) plot. Dynamic pull-in does not occur when initial energy is less than the energy at unstable equilibrium ($V_M < V_{DPI}$). When step-input amplitude $V_M = V_{DPI}$, initial energy equals the energy at unstable equilibrium. Dynamic pull-in occurs for $V_M > V_{DPI}$. (b) Phase portrait for three different step inputs. For $V_M < V_{DPI}$, the closed trajectory implies oscillatory response of the actuator. The voltage corresponding to the separatrix is V_{DPI} . The separatrix goes through a saddle point which corresponds to Q_{DPI} . Any step-input with $V_M > V_{DPI}$ results in an open trajectory, hence leading to dynamic pull-in.

The slope of the potential energy with respect to charge is

$$\frac{dU_M}{dq} = k(\epsilon_0 A_M)^2 V_M \left[\frac{f(q) - V_M}{q^3} \right] \quad (4.5)$$

$$\text{with } f(q) = \left[\frac{g_0}{\epsilon_0 A_M} \right] q - \left[\frac{1}{2k(\epsilon_0 A_M)^2} \right] q^3 \quad (4.6)$$

At static equilibrium, $dU_M/dq = 0$. Thus, we obtain the input voltage V_M as a function of the equilibrium charge q_* as

$$V_M = \left[\frac{g_0}{\epsilon_0 A_M} \right] q_* - \left[\frac{1}{2k(\epsilon_0 A_M)^2} \right] q_*^3 \equiv f(q_*) \quad (4.7)$$

as shown in Figure 4.2(b). To investigate the stability of the equilibrium charge q_* , we obtain

$$\frac{d^2U_M}{dq^2} \Big|_{q=q_*} = \frac{k(\epsilon_0 A_M)^2 V_M}{q_*^3} f'(q_*) \quad (4.8)$$

where $f'(q_*) = \frac{df(q)}{dq} \Big|_{q=q_*}$, is the reciprocal of the slope of the plot in Figure 4.2(b). Thus, from Eq. (4.8), we conclude that the equilibrium charge q_* is stable (unstable) when $f'(q_*)$ is positive (negative). The stable and unstable equilibrium charges coincide at $q_* = Q_{SPI}$ when $V_M = V_{SPI}$.

Using Eq. (4.7) and imposing $d^2U_M/dq^2 = 0$ at pull-in, since pull-in represents an inflection point, we obtain

$$V_{SPI} = \sqrt{\frac{8 k g_o^3}{27 \epsilon_o A_M}} ; Q_{SPI} = \sqrt{\frac{2 \epsilon_o k g_o A_M}{3}} \quad (4.9)$$

4.2.2 Dynamic pull-in

For dynamic pull-in, the transient effects due to the applied step-input of amplitude V_M should be considered. The initial conditions $x(0^+) = 0$ and $\dot{x}(0^+) = 0$ are translated to the charge coordinate as $q(0^+) = q_{init} = (\epsilon_0 A_M V_M)/g_o$ and $\dot{q}(0^+) = 0$, respectively using Eq. (4.2). Note that the electrostatic MEMS actuator gets charged to q_{init} instantaneously at $t = 0$. This is similar to the case of charging a capacitor in a circuit without any resistance (see for example Ref. [82]). As $\ddot{q}(0^+) = 0$, the total energy reduces to the potential energy and therefore, the initial energy is calculated from Eq. (4.4) with $q = q_{init}$. Figure 4.3(a) explains the concept of dynamic pull-in using the *potential energy (U_M) - charge (q) profile*. When a step-input of amplitude V_1 is applied at $t = 0$, the initial energy obtained is denoted as E_1 . The charge on the actuator causes a non-zero acceleration at $t = 0$. As a result, the top electrode starts moving, converting potential energy into kinetic energy. However, the displacement of the top electrode is limited by the potential energy bound in the potential energy-charge landscape, as shown in Figure 4.3(a). This results in an oscillatory response of the actuator in the charge coordinate, similar to the oscillatory response in the displacement coordinate. The oscillations are now between the initial charge q_{init1} and the corresponding charge q_{bound} as depicted in Figure 4.3(a). When the amplitude of the step-input is increased to V_2 , the initial energy E_2 equals the energy at the unstable equilibrium and this input corresponds to the dynamic pull-in voltage V_{DPI} . We define the unstable equilibrium charge corresponding to V_{DPI} as the dynamic pull-in charge Q_{DPI} . Any further increase in amplitude of the step voltage will result in the initial energy being greater than the energy at the unstable equilibrium. Hence, this will result in dynamic pull-in as depicted for a step-input of amplitude V_3 , in Figure

[4.3\(a\)](#). Thus, V_{DPI} and Q_{DPI} are derived using the condition that, at dynamic pull-in voltage, the initial energy is equal to the energy at dynamic pull-in charge; that is, when $V_M = V_{DPI}$, we have $U_M(q = q_{init}) = U_M(q = Q_{DPI})$. Using this and the fact that Q_{DPI} is also an equilibrium charge with $dU_M/dq = 0$ at Q_{DPI} , we obtain,

$$V_{DPI} = \sqrt{\frac{k g_o^3}{4 \epsilon_o A_M}} ; Q_{DPI} = \sqrt{\epsilon_o k g_o A_M} \quad (4.10)$$

Dynamic pull-in can also be visualized using the phase portrait. The phase plane is obtained from the 3D plot shown in Figure [4.1\(a\)](#), by taking the projection on the plane where total energy is *constant*. This constant is fixed by the initial energy. Each trajectory in the phase plane shows the evolution of a set of initial conditions (q and \dot{q}), with time, for an applied step input. The collection of such trajectories for different applied voltages is called the phase portrait as shown in Figure [4.3\(b\)](#). For an applied step-input of amplitude 4.7 V, the closed trajectory in the phase portrait implies oscillatory response of the actuator. The dynamic pull-in voltage $V_{DPI} = 4.88$ V manifests in the form of a separatrix that separates the behaviour before pull-in and after pull-in. The separatrix goes through a saddle point which corresponds to Q_{DPI} . Using Eq. [\(4.2\)](#), the charge $Q_{DPI} = 0.62$ pC corresponds to a dynamic pull-in displacement of $X_{DPI} = g_o/2 = 1$ μm (see Figure [2.4\(a\)](#) in Chapter [2](#)). Any step-input with amplitude greater than V_{DPI} ($V_M = 4.9$ V) will result in dynamic pull-in, as depicted by the open trajectory in the phase portrait.

4.2.3 Pull-out

After achieving pull-in (static or dynamic), the top electrode has moved a distance of $x_{PO} = g_o - h_s$. In the charge coordinate, using Eq. [\(4.2\)](#), this corresponds to a charge $q_{final} = \epsilon_o A_M V_M / h_s$. The pull-out phenomenon can be understood using the potential energy (U_M) - charge (q) plot as illustrated in Figure [4.4](#). The top electrode remains attached to the bottom electrode as long as there exists an energy barrier ($dU_M/dq < 0$) at charge q_{final1} for an applied voltage V_1 . At the pull-out voltage V_{PO} , the energy barrier disappears ($dU_M/dq = 0$). That is, for $V_2 = V_{PO}$, we have $q_{final2} = Q_{PO} = \epsilon_o A_M V_{PO} / h_s$. Any applied voltage less

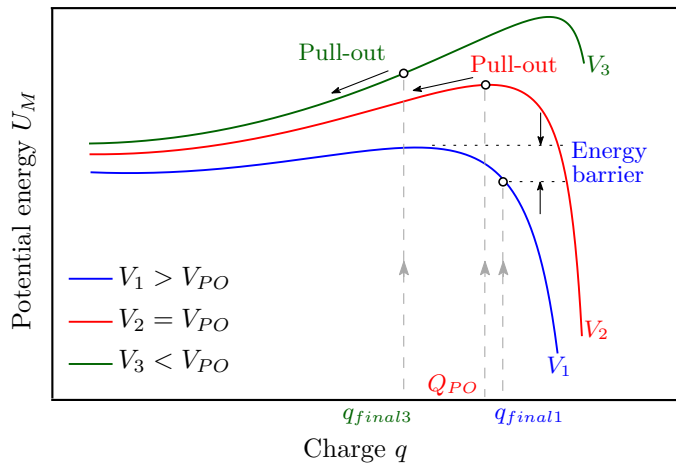


Figure 4.4: Illustration of pull-out phenomenon using potential energy (U_M) - charge (q) plot. For input voltage $V_1 > V_{PO}$, the presence of energy barrier at q_{final1} prevents pull-out. For input voltage $V_2 = V_{PO}$, the energy barrier just disappears at $q_{final2} = Q_{PO}$, resulting in pull-out. For input voltage $V_3 < V_{PO}$, the absence of energy barrier at q_{final3} results in pull-out.

than V_{PO} also results in pull-out ($dU_M/dq > 0$ at q_{final3}), as illustrated in Figure 4.4. Since the slope of the potential energy-charge profile is zero at Q_{PO} for applied voltage $V_M = V_{PO}$, from Eq. (4.5), setting $\frac{dU_M}{dq} = 0$ with $q = Q_{PO}$, we derive

$$V_{PO} = \sqrt{\frac{2 k h_s^2 (g_o - h_s)}{\epsilon_o A_M}} \quad (4.11)$$

Pull-out can also be visualized using the phase portrait as shown in Figures 4.5(a),(b). Release of the top electrode is not achieved when the step-input is reduced to 1.01 V as q_{final1} lies on the open trajectory. When the input is further reduced to $V_{PO} = 1$ V, the corresponding charge $q_{final}(V_M = V_{PO}) = Q_{PO}$ lies on the closed trajectory and hence the top electrode gets released. The closed trajectory illustrates the sustained oscillatory response of the top electrode, after release, in the absence of damping.

Note that the voltage expressions derived above for static pull-in, dynamic pull-in and pull-out using the energy-charge landscape are identical with those derived from the energy-displacement landscape (see Table 2.2) [1, 58]. Whether the input voltage is varied slowly as in the case of static input, or the input voltage is varied suddenly as in the case of dynamic input, the pull-out voltage is the same.

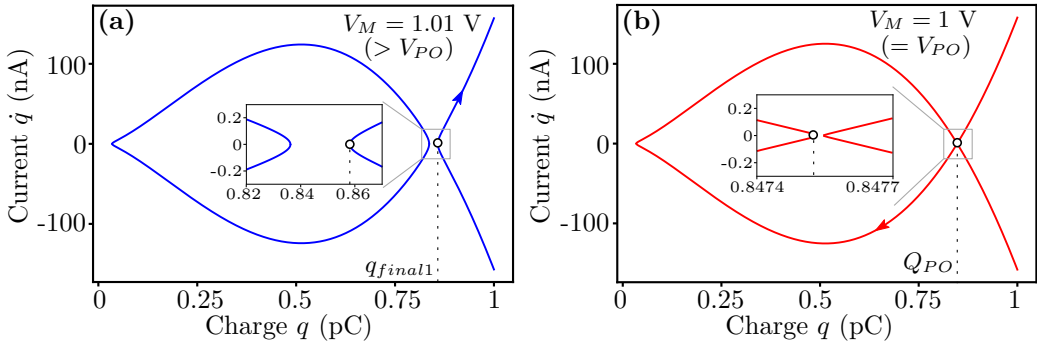


Figure 4.5: Illustration of pull-out phenomenon using phase-portrait. Phase portrait for step-input with amplitude (a) 1.01 V and (b) 1 V. Release of the top electrode is not achieved when the step-input is reduced to 1.01 V as q_{final1} lies on the open trajectory. When the input is reduced to $V_{PO} = 1$ V, the corresponding charge Q_{PO} lies on the closed trajectory and hence the top electrode gets released.

This is because the actuator remains at $x = g_o - h_s$ until the input voltage V_M is reduced to V_{PO} , be it slowly or suddenly, leading to disappearance of the energy barrier. Thus it is the disappearance of the energy barrier that decides the pull-out rather than the manner by which the input voltage is varied. Contrast this with the situation during pull-in: the electrostatic MEMS actuator can pull-in either if the system does not see a barrier or the system has sufficient energy to surmount the barrier. The former case happens for slowly varying input V_M (static pull-in) or step excitation (dynamic pull-in) with $V_M > V_{SPI}$. The latter case happens only for step excitation with $V_M > V_{DPI}$ and $V_M < V_{SPI}$ (that is, $V_{DPI} < V_M < V_{SPI}$). Hence, it is the nature of the energy landscape that brings out the above described

Table 4.1: Pull-in and pull-out of an electrostatic MEMS actuator based on energy-charge landscape

Condition	Voltage	Charge
Static pull-in	$V_{SPI} = \sqrt{(8 k g_o^3)/(27 \epsilon_o A_M)}$	$Q_{SPI} = \sqrt{2 \epsilon_o k g_o A_M / 3}$
Dynamic pull-in	$V_{DPI} = \sqrt{(k g_o^3)/(4 \epsilon_o A_M)}$	$Q_{DPI} = \sqrt{\epsilon_o k g_o A_M}$
Pull-out	$V_{PO} = \sqrt{(2 k h_s^2 (g_o - h_s)) / (\epsilon_o A_M)}$	$Q_{PO} = \epsilon_o A_M V_{PO} / h_s$

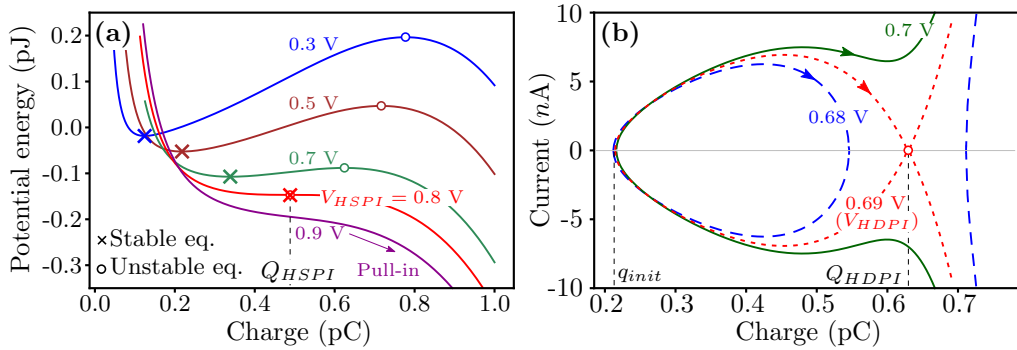


Figure 4.6: (a) Analysis of static pull-in in hybrid actuator using potential energy-charge plot. The stable and unstable equilibrium charges coincide at the static pull-in charge Q_{HSPI} , where input voltage V_{in} equals static pull-in voltage V_{HSPI} . (b) Analysis of dynamic pull-in in hybrid actuator using phase-portrait. Any step input with amplitude greater than dynamic pull-in voltage V_{HDPI} results in an open trajectory, leading to dynamic pull-in.

contrast between pull-in and pull-out. The expressions for the voltage and charge, derived using the proposed framework, are summarized in Table 4.1.

4.3 ANALYSIS OF HYBRID ACTUATOR USING ENERGY-CHARGE LANDSCAPE

Consider the hybrid actuator, whose schematic and equivalent circuit representation are shown in Figures 3.1(a),(b) in Chapter 3. The parameters of the hybrid actuator are listed in Table 3.1 in Chapter 3. The energy associated with the ferroelectric capacitor (neglecting the ferroelectric damping) is given by [17]

$$U_F(q) = -\frac{1}{2} \alpha q^2 + \frac{1}{4} \beta q^4 + \frac{1}{6} \gamma q^6 - V_F q \quad (4.12)$$

Since both the ferroelectric and the MEMS actuator are in series in the hybrid actuator, they share the same charge. Therefore, we obtain the Hamiltonian of the hybrid actuator H_H , expressed in terms of charge as

$$H_H(q, \dot{q}, t) = U_F(q) + \underbrace{H_M(q, \dot{q}, t)}_{\text{Eq. (4.3)}} \quad (4.13)$$

where $V_M = V_{in} - V_F$ and $V_F = -\alpha q + \beta q^3 + \gamma q^5$. By making use of Eq. (4.13), the hybrid actuator can be analyzed using its energy-charge landscape and phase-portrait (charge vs. current), similar to the aforementioned analysis of the standalone actuator in Section 4.2.

For instance, the static pull-in is examined using the potential energy-charge plot, as shown in Figure 4.6(a). Note that the potential energy-charge relation is obtained by setting $\dot{q} = 0$ in Eq. (4.13). From the plot, we obtain a static pull-in voltage $V_{HSP1} = 0.8$ V and a static pull-in charge $Q_{HSP1} = 0.49$ pC. The charge Q_{HSP1} now corresponds to a travel range of 0.62 μm (see Figure 3.3).

Likewise, dynamic pull-in is analyzed using the phase-portrait, as shown in Figure 4.6(b). Here, the initial charge q_{init} , corresponding to $x = 0$, is obtained by solving the modified mapping function as

$$q_{init} = \frac{\epsilon_0 A_M V_M}{g_o} = \frac{\epsilon_0 A_M (V_{in} - V_F)}{g_o} \quad (4.14a)$$

$$V_F = -\alpha q_{init} + \beta q_{init}^3 + \gamma q_{init}^5 \quad (4.14b)$$

We plot the phase portrait by noting that total energy is conserved. Thus, for any step voltage V_{in} applied at $t = 0$, the total energy E_{total} can be obtained by setting $q = q_{init}$, $\dot{q} = 0$ (corresponding to the initial conditions) in Eq. (4.13). We then solve the implicit algebraic equation $H_H(q, \dot{q}) = E_{total}$ to obtain \dot{q} for different values of q . The trajectory $\dot{q}(q)$ shows the evolution of the system for a specific applied step input, in the charge-current phase plane. From the phase-portrait plot, we obtain a dynamic pull-in voltage $V_{HDPI} = 0.69$ V and a dynamic pull-in charge $Q_{HDPI} = 0.63$ pC. This charge now corresponds to a dynamic pull-in displacement of 1.01 μm (see Figure 3.5(a)).

The results obtained using the proposed energy landscape approach are thus in good agreement with the numerical SPICE simulations in Chapter 3.

Pull-out can also be analyzed using the phase-portrait, as depicted in Figure 4.7. Here, the charge q_{final} , corresponding to $x = g_o - h_s$, is obtained by solving the modified mapping function as

$$q_{final} = \frac{\epsilon_0 A_M V_M}{h_s} = \frac{\epsilon_0 A_M (V_{in} - V_F)}{h_s} \quad (4.15a)$$

$$V_F = -\alpha q_{final} + \beta q_{final}^3 + \gamma q_{final}^5 \quad (4.15b)$$

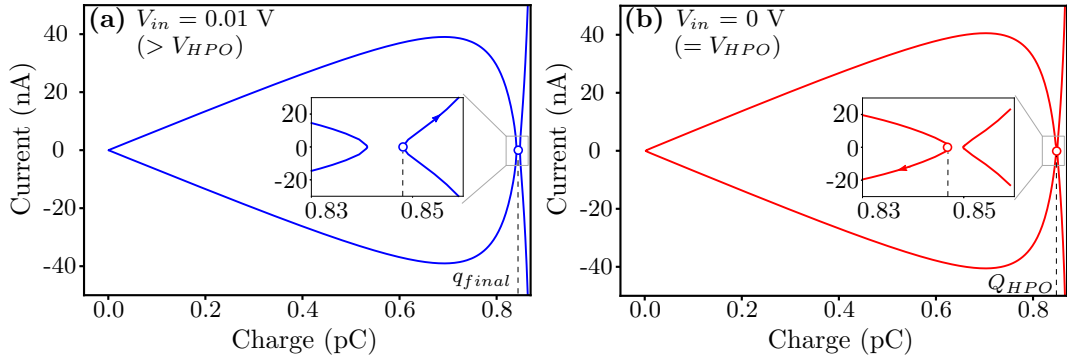


Figure 4.7: Analysis of pull-out in hybrid actuator (a) Phase-portrait for $V_{in} = 0.01$ V. The charge q_{final} lies on the open trajectory, indicating the absence of pull-out. (b) Phase-portrait for $V_{in} = 0$ V. The charge Q_{HPO} lies on the closed trajectory, indicating the occurrence of pull-out.

The total energy E_{total} is obtained by setting $q = q_{final}$, $\dot{q} = 0$ in Eq. (4.13). Again, we solve the implicit algebraic equation $H_H(q, \dot{q}) = E_{total}$ to obtain \dot{q} for different values of q , thereby obtaining the phase-portrait plots. Pull-out occurs when the input voltage is reduced to $V_{HPO} = 0$ V as $q_{final} = Q_{HPO}$ lies on the closed trajectory, as depicted in Figure 4.7(b). The result obtained is in agreement with the numerical SPICE simulation result in Chapter 3 (see Figures 3.3 and 3.5(c)).

Displacement is the conventional variable used for the analysis of electrostatic MEMS actuators. Analysis based in displacement is convenient to include effects such as adhesion, that are directly described in terms of displacement. Hence, it is sometimes more convenient to describe the hybrid actuator, in terms of displacement of the movable electrode. The mapping function derived in this chapter can be used to obtain the Hamiltonian of the hybrid actuator, in terms of displacement, as explained in Chapter 5. Nevertheless, the charge based description offers some advantages. For example, the parameters of the standalone actuator can be estimated based on an electrical measurement technique using the proposed energy-charge landscape. This is detailed in the next section.

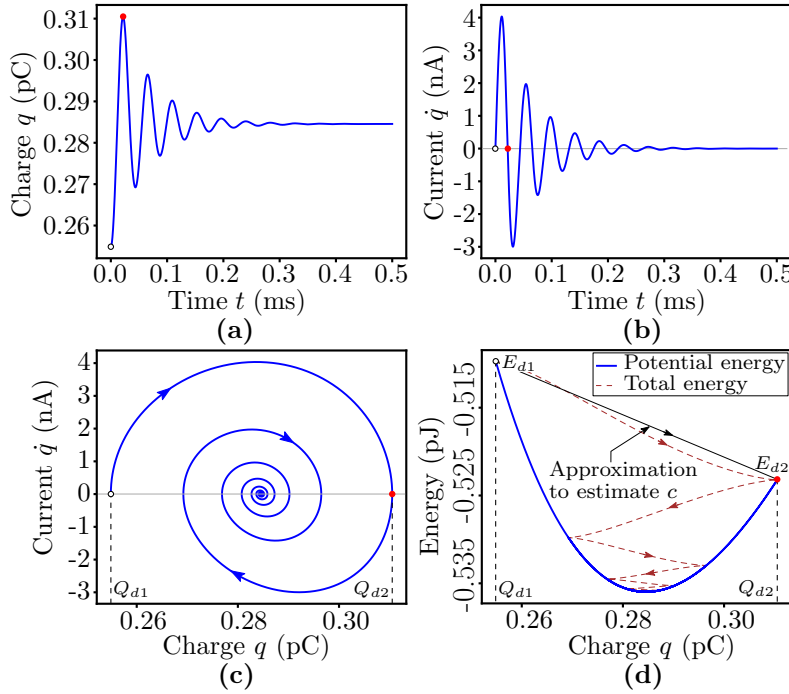


Figure 4.8: Plots for step input actuation with $V_M = 4$ V and $\zeta = 0.1$. (a),(b) Transient response of the charge and current. (c) Phase portrait depicting the decaying oscillations of the charge and current. (d) Potential energy - charge plot, along with the time evolution of the total energy. Damping coefficient c is estimated based on the approximation in Ref. [83]. The estimated value of c is 2.3×10^{-6} Ns/m (exact value of c is 1.8×10^{-6} Ns/m).

4.4 ESTIMATION OF PARAMETERS OF STANDALONE ACTUATOR

In this section, we propose the estimation of various parameters of the standalone actuator based on the energy-charge landscape. We first examine the impact of damping by including the damping coefficient c in the 1-DOF model in Figure 2.1(c). Here, c represents an effective value accounting for various damping mechanisms in MEMS [1]. We calculate the damping coefficient as $c = 2m\omega_0\zeta$, where $\omega_0 = \sqrt{k/m}$ is the natural frequency and ζ is the damping ratio of the mechanical beam structure [1]. The dynamic pull-in voltage is influenced by damping [75]. With increase in damping, the dynamic pull-in voltage approaches V_{SPI} . The dynamic response, before pull-in, decays with time and the actuator settles

at the static equilibrium displacement corresponding to the magnitude of the applied step input. The transient response in the charge coordinate also shows a similar behaviour. For example, Figures 4.8(a),(b) show the transient charge $q(t)$ and current $\dot{q}(t)$ plotted for $\zeta = 0.1$ and $V_M = 4$ V. These plots have been obtained by numerically solving the MEMS dynamics in the charge coordinate. The corresponding phase portrait is plotted in Figure 4.8(c), where the trajectory is an inward spiral (unlike the closed trajectory for the undamped case in Figure 4.3(b)). Using Eq. (4.3) and Eq. (4.4), we also plot the total energy and the potential energy, as a function of charge, as shown in Figure 4.8(d). The total energy of the system evolves with time, as depicted by its trajectory and finally, the system settles at the static equilibrium charge.

Electrical measurement techniques for estimation of various MEMS parameters are common and are widely reported in literature [84–88]. We now propose a procedure to estimate various parameters using the energy-charge landscape, based on electrical measurements. For instance, an electrical measurement set-up (such as, in Ref. [84]) could be used to measure the transient current $\dot{q}(t)$, for a step-input excitation with V_M less than the pull-in voltage. The transient charge $q(t)$ can then be obtained by integrating $\dot{q}(t)$. With the help of the transient response and energy plots, we can estimate parameters such as displacement, velocity, air-gap, spring constant and damping coefficient. Velocity is estimated as $\dot{x}(t) = \epsilon_0 A_M V_M(t) \dot{q}(t) / q^2(t)$. Displacement $x(t)$ can be obtained by integrating $\dot{x}(t)$. Note that the final steady state value of the charge in the transient response in Figure 4.8(a), corresponds to the stable equilibrium charge of the static response. This allows us to estimate air-gap g_o and spring constant k from the equilibrium charge-voltage relationship, given by Eq. (4.7). Let the stable equilibrium (steady state) charges be denoted as Q_a and Q_b for two different step inputs of amplitude V_a and V_b respectively (V_a, V_b less than the dynamic pull-in voltage). Using Eq. (4.7), we propose the estimation of g_o and k as

$$g_o = \frac{A_M \epsilon_0 (V_b Q_a^3 - V_a Q_b^3)}{Q_a Q_b (Q_a^2 - Q_b^2)}; k = \frac{Q_a Q_b (Q_a^2 - Q_b^2)}{2 A_M^2 \epsilon_0^2 (Q_a V_b - Q_b V_a)} \quad (4.16)$$

Any point on the potential energy plot in Figure 4.8(d) corresponds to zero kinetic energy, implying $\dot{q} = 0$, according to Eq. (4.3). Thus, we can obtain the potential

energies E_{d1} and E_{d2} in Figure 4.8(d), corresponding to the two consecutive charges Q_{d1} and Q_{d2} on the phase portrait, where $q = 0$ (see Figure 4.8(c)). The energy dissipated during this time interval can be calculated as $\Delta E_d = E_{d1} - E_{d2}$. From the estimated $x(t)$ and $\dot{x}(t)$, the distance travelled during this time interval, x_d , and the average velocity for traversing this distance, v_{avg} , can also be calculated. Based on Ref. [83], we propose to estimate an approximate value of the damping coefficient as $c \approx \Delta E_d / (x_d v_{avg})$. Based on our simulation, we find this approximation to give a reasonable estimate of c (within 50% of the actual value) for ζ in the range 0 to 0.55. Note that the value of mass m is not needed to determine E_{d1} and E_{d2} . The above described technique could be an alternative to the other methods available [89] for the measurement of these parameters.

4.5 SUMMARY

We have presented a framework to analyze the statics and dynamics of the hybrid actuator from its energy-charge landscape. The proposed method employs coordinate transformation from the conventional displacement coordinate to the charge coordinate. This coordinate transformation is used in the Hamiltonian formalism to obtain the energy-charge relationship. The results obtained from the proposed energy landscape method are in good agreement with the numerical SPICE simulations. For the standalone actuator, we have derived the expression for the voltage and charge under static and dynamic conditions. The proposed framework also allows estimation of the parameters of the standalone actuator based on an electrical measurement technique.

5

ANALYSIS OF HYBRID MEMS ACTUATOR USING ENERGY-DISPLACEMENT LANDSCAPE

In this chapter, we propose an energy-displacement based framework to analyze the statics and dynamics of a hybrid MEMS actuator. The ferroelectric capacitor is governed by the nonlinear Landau-Khalatnikov (LK) equation [17], which relates the voltage across the ferroelectric to its charge. The MEMS actuator, on the other hand, is governed by a nonlinear differential equation [1], expressed in terms of displacement of the movable electrode. It is convenient to describe both the ferroelectric and the MEMS actuator in terms of a common entity. For instance, the response of the hybrid actuator to slowly varying (quasi-static) inputs was analytically studied in Refs. [17, 19] using charge as the common variable. They solve the algebraic equations that describe the balance between the electrostatic attraction and spring restoring forces at equilibrium. Our earlier work in Chapter 4 analyzes both the static and dynamic response of standalone MEMS actuators based on their energy-charge landscape. This technique can, in principle, be extended to analyze the hybrid actuator as well, as explained in Section 4.3 in Chapter 4.

However, for many applications, displacement is a more natural coordinate used to analyze MEMS actuators [1]. Analysis based on displacement is convenient to include effects such as adhesion [64, 90, 91] and a non-linear spring [20], that are directly described in terms of displacement. We had developed a numerical model in Chapter 3 to analyze both the statics and dynamics of the hybrid actuator, based on displacement. The numerical model solves the nonlinear, coupled, differential equations using the inbuilt solvers of a circuit simulator. The numerical approach,

though, provides very limited physical insight into the response of the hybrid actuator.

In this chapter, we develop a physics-based graphical framework, using displacement as the dynamical variable, that facilitates a systematic analysis of the statics and dynamics of the hybrid actuator¹. We employ a coordinate transformation from the charge to the displacement of the movable electrode, in order to describe the ferroelectric in terms of displacement. This allows us to express the Hamiltonian (energy) of the hybrid **MEMS** actuator in terms of displacement. We then use graphical energy-displacement and phase portrait (velocity vs. displacement) plots to investigate static pull-in, dynamic pull-in and pull-out phenomena of the hybrid **MEMS** actuator. Using these, we illustrate the low-voltage operation of the hybrid actuator to static and step inputs, as compared to the standalone **MEMS** actuator. The results obtained are in agreement with the analytical predictions and numerical simulations.

The usefulness of describing the Hamiltonian in terms of displacement is illustrated by studying the effect of adhesion in the hybrid actuator. Adhesion plays a major role when the top electrode comes in contact with the bottom surface. We include the effect of adhesion between contacting surfaces, by adding a term corresponding to the van der Waals force [64, 90, 91] into the Hamiltonian of the system. We show that adhesion reduces the pull-out voltage but does not affect the pull-in voltage. We demonstrate how the actuator can be redesigned so that the reduction in pull-out voltage (due to adhesion) can be compensated. We show that this redesign causes an increase in the pull-in voltage; nevertheless, the new pull-in voltage is predicted to still be considerably lower than the pull-in voltage of the standalone **MEMS** actuator. The proposed framework could serve as a quick design and analysis tool to predict the pull-in and pull-out behavior of the hybrid actuator as it uses only graphical plots for the analysis.

¹ This work is published in Raghuram Tattamangalam Raman, Jeffin Shibu, Revathy Padmanabhan and Arvind Ajoy, "Analysis of Ferroelectric Negative Capacitance- Hybrid MEMS Actuator Using Energy–Displacement Landscape," IEEE Trans. Electron Devices, vol. 69, no. 06, pp. 3359-3366, Jun. 2022, doi: 10.1109/TED.2022.3164633.

5.1 HAMILTONIAN OF THE HYBRID ACTUATOR

We consider the hybrid actuator as shown in Figures 3.1(a),(b) and the 1-DOF model of the MEMS actuator as shown in Figure 3.1(c), in Chapter 3. The Hamiltonian (total energy) H_M of the standalone electrostatic MEMS actuator (see Figure 3.1(c)), in the absence of damping, is given by

$$H_M(x, \dot{x}, t) = \underbrace{\frac{1}{2} m \dot{x}^2}_{\text{Kinetic energy}} + \underbrace{\frac{1}{2} k x^2 - \frac{1}{2} \frac{\epsilon_0 A_M V_M^2(t)}{(g_o - x)}}_{\text{Potential energy}} \quad (5.1)$$

where x and $\dot{x} = \frac{dx}{dt}$ represent the displacement and velocity, m denotes the mass, k denotes the spring constant, g_o represents the air-gap, A_M denotes the actuation area and ϵ_0 represents the permittivity of free space. Note that damping does not affect pull-out and static pull-in. However, with an increase in damping constant c , the dynamic pull-in voltage increases from V_{DPI} and approaches the static pull-in voltage V_{SPI} [28]. Hence the analysis presented in this chapter (with $c = 0$) provides an estimate of the lowest possible dynamical pull-in voltage.

With the single domain assumption, the Landau-Khalatnikov (LK) equation [17, 18, 31] relates the voltage across the ferroelectric capacitor V_F to the charge q (where $q = \int i dt$) as

$$V_F = -\alpha q + \beta q^3 + \gamma q^5 \quad (5.2)$$

$$\alpha = -\frac{\alpha_F t_F}{A_F}, \beta = \frac{\beta_F t_F}{A_F^3}, \gamma = \frac{\gamma_F t_F}{A_F^5} \quad (5.3)$$

where α_F , β_F and γ_F are ferroelectric anisotropy coefficients, t_F and A_F are the thickness and area of the ferroelectric respectively. Note that we neglect the ferroelectric damping constant ρ in this chapter. The energy associated with the ferroelectric capacitor is given by

$$U_F(q) = -\frac{1}{2} \alpha q^2 + \frac{1}{4} \beta q^4 + \frac{1}{6} \gamma q^6 - V_F q \quad (5.4)$$

Note that the Eq. (5.4) is written in terms of charge q , whereas Eq. (5.1) is described in terms of displacement x . In this chapter, we use displacement of

the movable electrode as the common dynamical variable to describe both the **MEMS** actuator and the ferroelectric capacitor. Both the ferroelectric capacitor and the **MEMS** actuator share the same charge q , since they are connected in series. Based on our earlier work on electrostatic **MEMS** actuators in Chapter 4, we relate the charge q to the displacement x of the movable electrode, using the mapping function

$$q = \frac{\epsilon_0 A_M V_M(t)}{(g_o - x)} \quad (5.5)$$

This mapping function is based on the charge-voltage relationship of a parallel plate capacitor. Using Eq. (5.2) and applying Kirchhoff's voltage law in Figure 3.1(b), Eq. (5.5) can be rearranged to obtain

$$q^5 \left[\frac{\epsilon_0 A_M \gamma}{g_o - x} \right] + q^3 \left[\frac{\epsilon_0 A_M \beta}{g_o - x} \right] + q \left[1 - \frac{\epsilon_0 A_M \alpha}{g_o - x} \right] - \frac{\epsilon_0 A_M V_{in}(t)}{g_o - x} = 0 \quad (5.6)$$

We solve the above equation (discarding the complex roots), to obtain the charge q as a function of the applied voltage and displacement. This charge is then substituted in Eq. (5.2) and Eq. (5.4) to obtain the energy associated with the ferroelectric U_F , in terms of displacement. We can thus write the Hamiltonian of the hybrid actuator as

$$H_H(x, \dot{x}, t) = U_F(x) + H_M(x, \dot{x}, t) \quad (5.7)$$

where both the ferroelectric and **MEMS** actuator are described in terms of the displacement of the **MEMS** actuator. We will see later in Section 5.3 that writing the Hamiltonian of the hybrid actuator in terms of x allows us to include the effect of adhesion in a straightforward manner.

5.2 ANALYSIS OF THE HYBRID ACTUATOR

From the Hamiltonian $H_H(x, \dot{x}, t)$ in Eq. (5.7), we obtain the potential energy-displacement relation by setting $\dot{x} = 0$. The hybrid actuator is analyzed using using the potential energy-displacement and phase-portrait (velocity-displacement) plots as explained in the following sections.

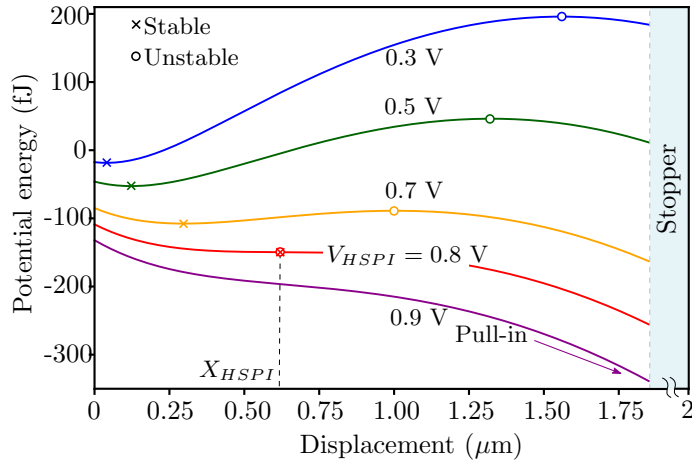


Figure 5.1: Potential energy-displacement plot depicting static pull-in. Stable and unstable equilibrium displacements coincide at static pull-in voltage, $V_{HSPI} = 0.8$ V, with travel range $X_{HSPI} = 0.62$ μm .

5.2.1 Static pull-in

The potential energy-displacement plot of the hybrid actuator shown in Figure 5.1 explains static pull-in. For an applied voltage less than the static pull-in voltage, there are two equilibrium displacements: stable (denoted by \times) and unstable (denoted by \circ). These equilibrium displacements coincide when the input voltage equals the static pull-in voltage of the hybrid actuator, $V_{HSPI} = 0.8$ V. Correspondingly, the travel range of the hybrid actuator, $X_{HSPI} = 0.62$ μm . Beyond V_{HSPI} , the absence of any stable equilibrium displacement results in static pull-in, as depicted in Figure 5.1. The results obtained using the proposed framework exactly match with the analytical predictions in Chapter 2 based on Ref. [17] (see Table 2.4) and with the numerical simulations in Chapter 3 (see Figure 3.3).

5.2.2 Dynamic pull-in

Figure 5.2(a) depicts dynamic pull-in in the hybrid actuator using potential energy-displacement plots. Note that the initial energy (energy at $x = 0$) equals the energy at point of the unstable equilibrium for an applied step voltage of 0.69 V. This

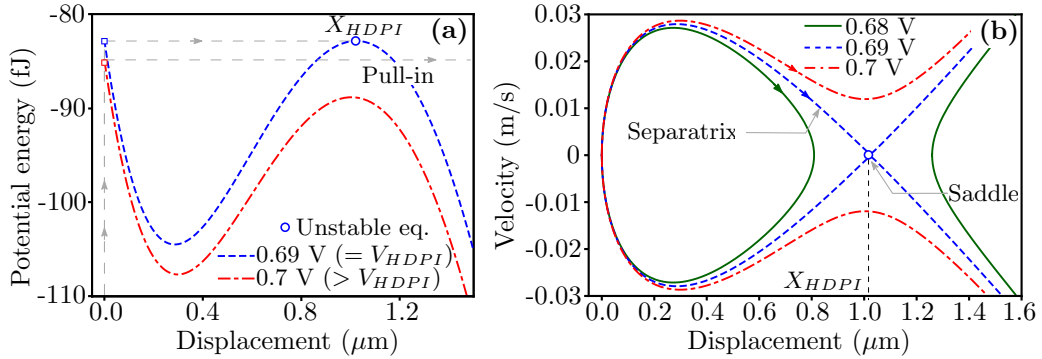


Figure 5.2: Analysis of dynamic pull-in using (a) potential energy-displacement plot. Initial energy at $x = 0$ equals the energy at the point of unstable equilibrium when the step input equals the dynamic pull-in voltage, $V_{\text{HDPI}} = 0.69 \text{ V}$. Any step input greater than V_{HDPI} results in dynamic pull-in and (b) phase-portrait: the trajectory becomes open when dynamic pull-in occurs.

corresponds to the dynamic pull-in voltage of the hybrid actuator, V_{HDPI} . Correspondingly, the dynamic pull-in displacement, $X_{\text{HDPI}} = 1.01 \mu\text{m}$, as depicted in Figure 5.2(a). Any step input greater than V_{HDPI} will result in dynamic pull-in because the initial energy is greater than the energy at the point of unstable equilibrium, as illustrated in Figure 5.2(a).

Dynamic pull-in can also be visualized using a phase-portrait (velocity-displacement plot). We plot the phase portrait by noting that total energy is conserved. Thus, for any step voltage V_{in} applied at $t = 0$, the total energy E_{total} can be obtained by setting $x = 0$, $\dot{x} = 0$ (corresponding to the initial conditions) in Eq. (5.7). We then solve the implicit algebraic equation $H_H(x, \dot{x}) = E_{\text{total}}$ to obtain \dot{x} for different values of x . The trajectory $\dot{x}(x)$ shows the evolution of the system for a specific applied step input, in the displacement-velocity phase plane. Note that time t does not appear explicitly in Eq. (5.7) for a step input, provided $t > 0^+$. The collection of trajectories for different applied voltages forms the phase-portrait. See Figure 5.2(b). For step input less than V_{HDPI} , the trajectory is closed, indicating an oscillatory response. The phase-portrait shows a separatrix for a step input voltage of $V_{\text{HDPI}} = 0.69 \text{ V}$. The separatrix runs through a saddle point that corresponds to the dynamic pull-in displacement, $X_{\text{HDPI}} = 1.01 \mu\text{m}$. Any step input greater than

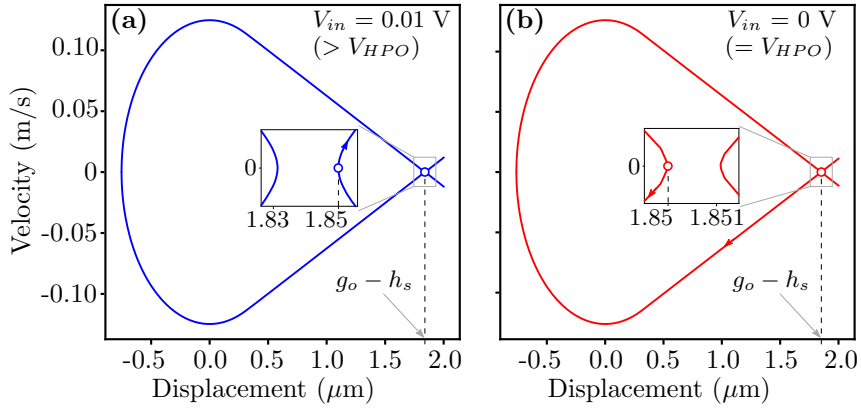


Figure 5.3: Analysis of pull-out using phase-portrait. (a) Pull-out does not occur for input greater than the pull-out voltage, V_{HPO} , as displacement $g_o - h_s$ lies on the open trajectory. (b) Pull-out occurs when input equals $V_{HPO} = 0 \text{ V}$ as $g_o - h_s$ lies on the closed trajectory.

V_{HDPI} results in dynamic pull-in, which is characterized by the open trajectory in the phase-portrait.

The results from the graphical approach (Figures 5.2(a), (b)) are in good agreement with the numerical simulations in Chapter 3 (see Figure 3.5). Note that there are no analytical results for dynamic pull-in of the hybrid actuator.

5.2.3 Pull-out

The pull-out of the hybrid actuator can be visualized using the phase-portrait as shown in Figures 5.3(a), (b). Note that the actuator has already achieved pull-in, after traveling a displacement of $x = g_o - h_s$, where g_o is the air-gap and h_s is the stopper height. Thus, for pull-out analysis, the initial displacement is at $x = g_o - h_s$, as opposed to the initial displacement of $x = 0$, for the dynamic pull-in analysis. The hybrid actuator does not pull-out when the input is reduced upto 0.01 V as the displacement $g_o - h_s$ lies on the open trajectory. However, when the input voltage is further reduced to 0 V, the displacement $g_o - h_s$ lies on the closed trajectory, indicating pull-out. The closed trajectory represents sustained oscillations, after pull-out, in the absence of damping. Hence, the pull-out voltage of the hybrid actuator $V_{HPO} = 0 \text{ V}$. The estimated pull-out voltage of the hybrid

Table 5.1: Summary of analysis of the hybrid actuator

Parameter	Energy-displacement	Numerical (Chapter 3)	Analytical (Ref. [17])
Static pull-in voltage, V_{HSPI}	0.8 V	0.8 V	0.8 V
Travel range, X_{HSPI}	0.62 μm	0.62 μm	0.62 μm
Dynamic pull-in voltage, V_{HDPI}	0.69 V	0.69 V	N.A.
Dynamic pull-in displacement, X_{HDPI}	1.01 μm	1.01 μm	N.A.
Pull-out voltage, V_{HPO}	0 V	0 V	0 V

actuator matches with the analytical prediction in Chapter 2 based on Ref. [17] (see Table 2.4) and with the numerical simulation in Chapter 3 (see Figure 3.3).

Table 5.1 gives the summary of the analysis of the hybrid actuator using different methods.

5.3 EFFECT OF ADHESION

In this section, we analyze the pull-in and pull-out phenomena in the presence of adhesion (stiction force) between the contacting surfaces. When the beam is actuated so that the top electrode comes in contact with the stopper, adhesion plays an important role. As the Hamiltonian of the hybrid actuator is expressed in terms of displacement, our framework can directly include adhesion. The proposed graphical approach based on energy landscape gives physical insight into understanding the effect of adhesion. We model the adhesion between the contacting surfaces using the van der Waals force [64, 90–92], based on the Lennard-Jones potential and given by

$$F_{LJ}(x) = \frac{A_H A_C}{6\pi} \left(\frac{1}{\delta^3(x)} - \frac{\Lambda^6}{\delta^9(x)} \right) \quad (5.8)$$

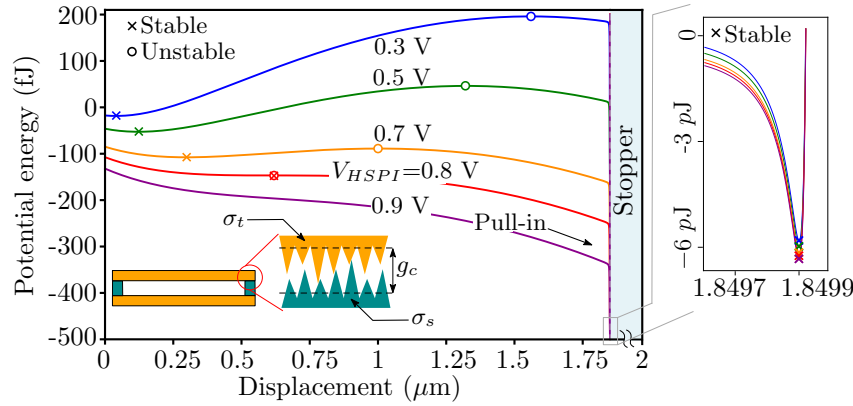


Figure 5.4: Effect of adhesion in the hybrid actuator. (a) Analysis of static pull-in using energy-displacement plot. The static pull-in voltage ($= 0.8 \text{ V}$) is not affected by adhesion. The plot near the contact is shown enlarged depicting the effect of adhesion. The inset in the main plot shows the effective gap at contact g_c due to surface roughness (σ_t, σ_s of the top electrode and stopper respectively), when the top electrode hits the stopper.

where $\delta(x) = g_o - h_s - x$ is the gap between the top electrode and the stopper. A_C is the area of contact. A_H is the Hamaker constant, and Λ is the inter-atomic equilibrium distance. Eq. (5.8) can also be expressed as

$$F_{LJ}(x) = \frac{C_1 A_C}{\delta^3(x)} - \frac{C_2 A_C}{\delta^9(x)} \quad (5.9)$$

and C_1, C_2 are the attractive and repulsive constants, respectively, with typical values $C_1 = 10^{-20} \text{ Nm}$, $C_2 = 10^{-80} \text{ Nm}^7$ [64]. The corresponding Lennard-Jones potential is given by

$$U_{LJ}(x) = \frac{-C_1 A_C}{2(g_o - h_s - x)^2} + \frac{C_2 A_C}{8(g_o - h_s - x)^8} \quad (5.10)$$

Since U_{LJ} is a function only of x , we can add it directly to the Hamiltonian of the hybrid actuator $H_H(x, \dot{x}, t)$. The Hamiltonian of the hybrid MEMS actuator is now modified to include the Lennard-Jones potential as

$$H_{HLJ}(x, \dot{x}, t) = H_H(x, \dot{x}, t) + U_{LJ}(x) \quad (5.11)$$

The effect of adhesion on the pull-in voltage is analyzed using the potential energy-displacement plot using Eq. (5.11) with $\dot{x} = 0$. As depicted in Figure 5.4, the static pull-in voltage ($= 0.8 \text{ V}$) is not changed due to adhesion. This is because van

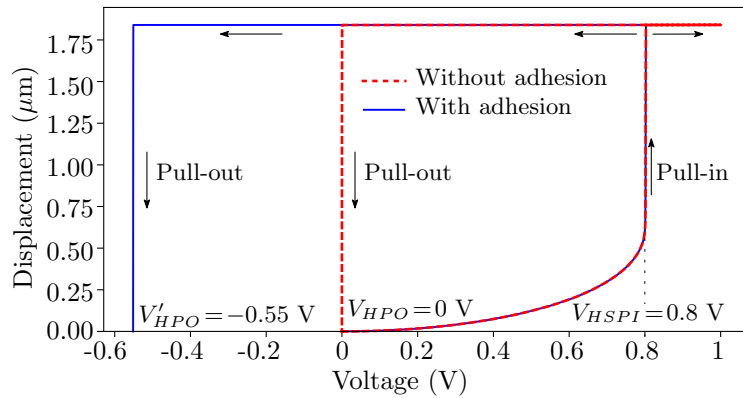


Figure 5.5: Numerical simulation of the static characteristics of the hybrid actuator without (red dashed) and with (blue solid) adhesion forces. Due to adhesion, the pull-out voltage is reduced from $V_{HPO} = 0$ V to $V'_{HPO} = -0.55$ V. However, the static pull-in voltage ($= 0.8$ V) remains unchanged.

der Waals force is a short-range force which does not change the energy landscape in regions away from the contact.

The numerical simulation of the static characteristics in Figure 5.5, based on Chapter 3, also confirms that the static pull-in voltage is unaffected due to adhesion. We have modified the simulation framework in Chapter 3 to include the effect of adhesion. Adhesion is implemented as an additional sub-circuit which models the van der Waals force (Eq. (5.9)). The numerical model of the standalone MEMS actuator now estimates the acceleration a based on the following force-balance equation

$$a = \frac{F_{elec} + F_{LJ} - F_{mech}}{m} \quad (5.12)$$

where F_{elec} , F_{LJ} and F_{mech} are the electrostatic, van der Waals and the mechanical restoring forces, respectively. The estimated acceleration is integrated to compute the velocity \dot{x} , which is again integrated to obtain the displacement x . The integration is performed by a built-in function available in the circuit simulator. The estimated velocity and displacement are given in a feedback loop to obtain the stable solution of the electrode displacement for an applied input voltage. Detailed implementation is given in Appendix, at the end of the thesis.

Note that a deep energy well, with a stable minima very close to the stopper location ($\approx g_o - h_s$) is created due to adhesion, as shown in Figure 5.4. When the

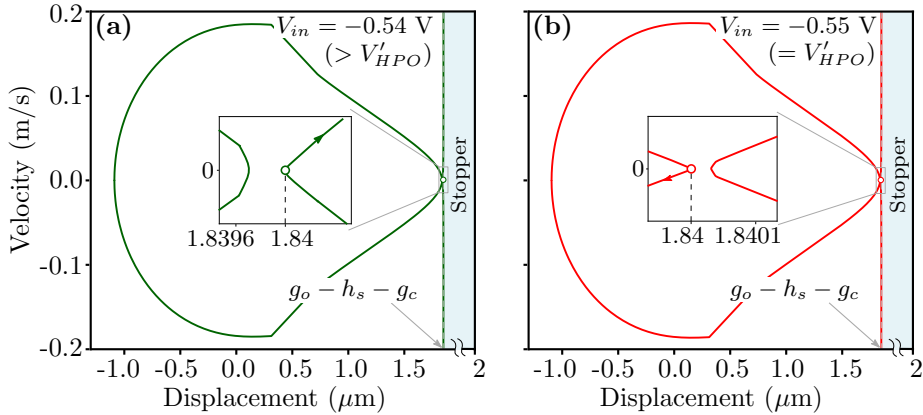


Figure 5.6: (a), (b) Analysis of pull-out in the presence of adhesion using phase-portrait.

Note that the initial displacement for pull-out analysis is $g_o - h_s - g_c$ due to surface roughness. The pull-out voltage is reduced to -0.55 V as a result of adhesion.

applied voltage exceeds the pull-in voltage, pull-in occurs and the beam comes in contact with the stopper. Due to the roughness of the contact surface, there are small asperities distributed all over the contact area [see inset in Figure 5.4]. As a result, there exists an effective gap at contact, g_c , between the two contacting surfaces. Assuming σ_t and σ_s are the standard deviations of the thickness of the top electrode and the height of the stopper respectively, we can define $g_c = \sqrt{\sigma_t^2 + \sigma_s^2}$ [91, 93]. Therefore, after pull-in, owing to the surface roughness, the top electrode settles effectively at $g_o - h_s - g_c$. The effective gap is a random variable that varies across different fabrication runs. For the chosen dimensions of the MEMS beam, we assume $g_c = 10 \text{ nm}$, based on Refs. [3, 91].

The pull-out voltage is analyzed using the phase-portrait, as shown in Figures 5.6(a), (b). As explained above, after pull-in, the top electrode settles at $g_o - h_s - g_c$. Therefore, for the analysis of pull-out using the phase portrait, the initial displacement to determine the total energy is $g_o - h_s - g_c$. Contrast this with the case without adhesion and surface roughness, wherein the initial displacement for pull-out analysis is $g_o - h_s$ [see Figures 5.3(a), (b)]. As shown in Figures 5.6(a), (b), the displacement $g_o - h_s - g_c$ is on the closed trajectory when the input is -0.55 V . Thus, adhesion reduces the pull-out voltage from $V_{HPO} = 0 \text{ V}$ (without adhesion; see Table 5.1) to $V'_{HPO} = -0.55 \text{ V}$. We also confirm this reduction in

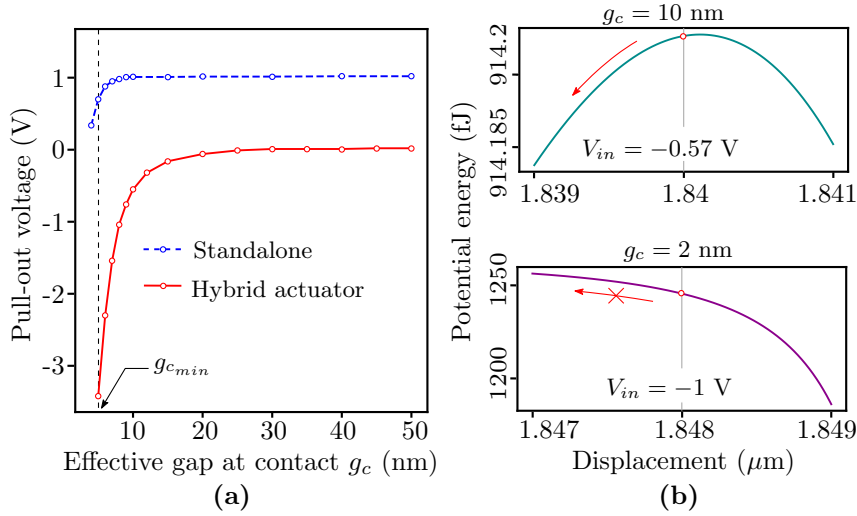


Figure 5.7: (a) Variation in the pull-out voltage with respect to the change in the effective gap at contact g_c . As effective gap increases, the pull-out voltage tends towards the electrostatically estimated (without adhesion) value. (b) Energy-displacement plots for $g_c = 10 \text{ nm}$ and 2 nm . The presence of an energy barrier prevents pull-out for $g_c = 2 \text{ nm}$ ($< g_{c_{\min}}$). Note that the \circ represents $(g_o - h_s - g_c)$ in both cases.

the pull-out voltage using the numerical simulation of the static characteristics, as shown in Figure 5.5. Thus, the pull-in voltage is unaffected and the pull-out voltage is reduced due to adhesion.

We now study the variation in the pull-out voltage with respect to the change in the effective gap at contact (g_c), as shown in Figure 5.7(a). The trend observed in the hybrid actuator is similar to the effect of adhesion on the pull-out voltage in the standalone actuator (for example, see Ref. [91]). As shown in Figure 5.7(a), the pull-out voltage tends towards the electrostatically estimated value (without adhesion) with an increase in g_c . This is because adhesion force becomes negligible for higher values of g_c . As in the case of the standalone actuator, there exists a minimum effective gap at contact ($g_{c_{\min}}$), in the hybrid actuator, below which pull-out does not occur in the presence of adhesion. For example, as shown in Figure 5.7(b), pull-out occurs for $g_c = 10 \text{ nm}$ ($> g_{c_{\min}}$) with $V_{in} = -0.57 \text{ V}$ ($< V'_{HPO}$). However, the presence of an energy barrier at $g_o - h_s - g_c = 1.848 \mu\text{m}$ for $g_c = 2 \text{ nm}$ ($< g_{c_{\min}}$) prevents pull-out. Thus, the effective gap at contact g_c and hence

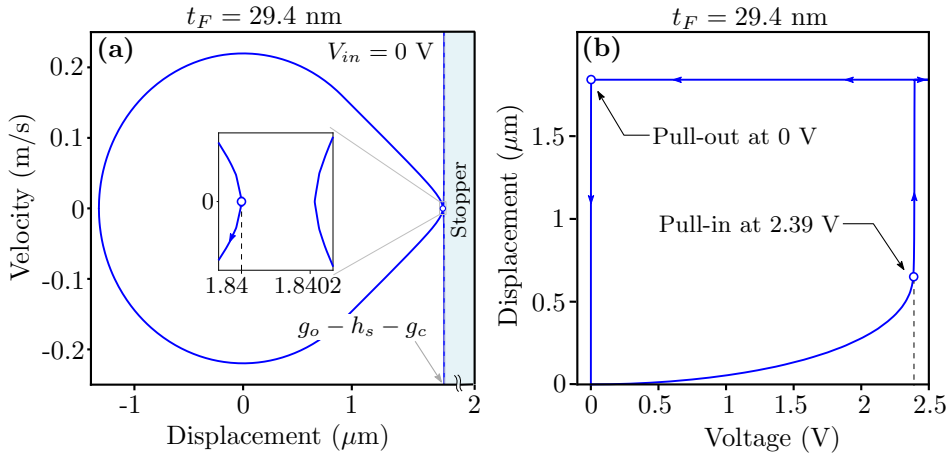


Figure 5.8: (a) Phase-portrait depicting that the pull-out voltage, in the presence of adhesion, is 0 V, achieved with a reduced ferroelectric thickness of $t_F = 29.4 \text{ nm}$. (b) Numerical simulation of the static characteristics of the hybrid actuator with $t_F = 29.4 \text{ nm}$.

the surface roughness plays a significant role in determining the pull-out behavior. For instance, pull-out can be facilitated by increasing the surface roughness [94] thereby reducing stiction.

We predict that the pull-out voltage can be brought back to 0 V, even in the presence of adhesion, by tailoring the ferroelectric thickness t_F . It has been predicted that both pull-in and pull-out voltages increase with reduction in the ferroelectric thickness (see Figure 3.6 in Chapter 3 and Ref. [60]). By looking at the slope of the potential energy-displacement plot at $g_o - h_s - g_c$, we predict that a reduction of the ferroelectric thickness to 29.4 nm eliminates the barrier for pull-out at zero applied voltage, as shown in Figures 5.8(a), (b). This is, however, accompanied with an increased pull-in voltage of 2.39 V. Nevertheless this increased pull-in voltage is still lower than the pull-in voltage of the standalone MEMS actuator (=5.32 V).

5.4 SUMMARY

To summarize, we have proposed a physics-based framework based on the energy-displacement landscape to systematically analyze the static pull-in, dynamic pull-in

and pull-out phenomena of the ferroelectric negative capacitance-hybrid [MEMS](#) actuator. Based on the proposed framework, we illustrate the low-voltage operation of the hybrid actuator for static and step inputs. The results obtained are in good agreement with analytical predictions and numerical simulations. We also include the effect of adhesion in the framework. We show that the pull-in voltage is not affected, while the pull-out voltage is reduced due to adhesion.

6

STABLE DEFLECTION IN HYBRID MEMS ACTUATOR WITH CUBIC NON-LINEAR SPRING

Electrostatic [MEMS](#) actuators suffer from two disadvantages: (a) high operating voltage and (b) pull-in instability. The hybrid actuator discussed in the previous chapters overcomes the need for high operating voltage in electrostatic [MEMS](#) actuators. However, it does not eliminate the pull-in instability.

Electrostatic [MEMS](#) actuators employ Coulombic force of attraction between a movable electrode and a fixed electrode to induce a displacement in the movable electrode. These actuators, however, suffer from pull-in instability [1]. Beyond a certain applied voltage, called the pull-in voltage, the movable electrode snaps down onto the fixed electrode. As a result, the maximum distance traveled by the movable electrode before it snaps down, termed as travel range, is limited to a fraction of the air-gap between the two electrodes. Therefore, the entire allowed range in the air-gap is not available for the stable operation of the electrostatic [MEMS](#) actuator.

Several methods have been proposed in the literature to improve the pull-in instability and thus, extend the travel range of the electrostatic [MEMS](#) actuator. For example, pull-in can be avoided by connecting a feedback capacitor or a MOS (Metal Oxide Semiconductor) capacitor operating in depletion mode, in series with the [MEMS](#) actuator [21, 95]. Pull-in can also be eliminated by using a specially designed non-linear spring that exactly counteracts the non-linear electrostatic force. For instance, an electrostatic [MEMS](#) actuator with a properly designed cam suspension can avoid pull-in [22, 96]. Here, the non-linear elastic spring is obtained from two parallel cantilevers whose length is effectively shortened by bending them over identical curved cams of a specific profile. Another technique to extend

the travel range is to use the effect of spring-stiffening [20, 97]. Replacing the planar electrodes with electrically re-configurable nano-structured electrodes [98] can also extend the travel range. This technique uses a non-planar and non-fixed geometrical structure, having an array of electrically connected cylinders and spheres. However, in the above mentioned techniques, the improved stability is achieved at the cost of increased supply voltage, as compared to the actuation voltage of the standalone MEMS actuator [20–22, 95, 98].

Our goal is to illustrate improved stability by eliminating pull-in, while operating at a lower voltage as compared to the standalone MEMS actuator. We begin with the idea of a hybrid MEMS actuator for low-voltage operation, based on Ref. [17]. This hybrid actuator is a series combination of a ferroelectric capacitor exhibiting negative capacitance and the MEMS actuator. Although the hybrid actuator in Ref. [17] is predicted to have low-voltage operation, pull-in instability is not eliminated. Moreover, it has a reduced travel range as compared to the standalone MEMS actuator [17].

In this chapter, we propose the elimination of pull-in instability in the hybrid actuator by adding a cubic non-linear spring to it¹. Cubic non-linearity in the spring can be introduced by spring-stiffening effect [20] and/or by using various non-linear micro-flexures [22, 99, 100]. We use a physics-based framework based on the energy landscape (Chapter 5) to illustrate the stability improvement. The framework uses graphical energy-displacement and voltage-displacement plots to analyze the hybrid MEMS actuator. Depending on the value of the cubic non-linear spring constant and the applied input voltage, we predict that the hybrid actuator can work in three distinct modes: (a) monostable (b) bistable and (c) always stable. The monostable mode suffers from the pull-in instability. The bistable mode mimics the operation of a standalone electrostatic bistable MEMS actuator [101], wherein, a snap-through behavior and hysteresis are observed in its static displacement-voltage characteristics. The *always-stable* mode depicts the elimination of the pull-in

¹ This work is published in Raghuram Tattamangalam Raman, Revathy Padmanabhan and Arvind Ajoy, "Stable Deflection in Ferroelectric Negative-Capacitance Hybrid MEMS Actuator with Cubic Non-Linear Spring," IEEE Trans. Electron Devices, vol. 69, no. 09, pp. 5162-5169, Sep. 2022, doi:10.1109/TED.2022.3190258

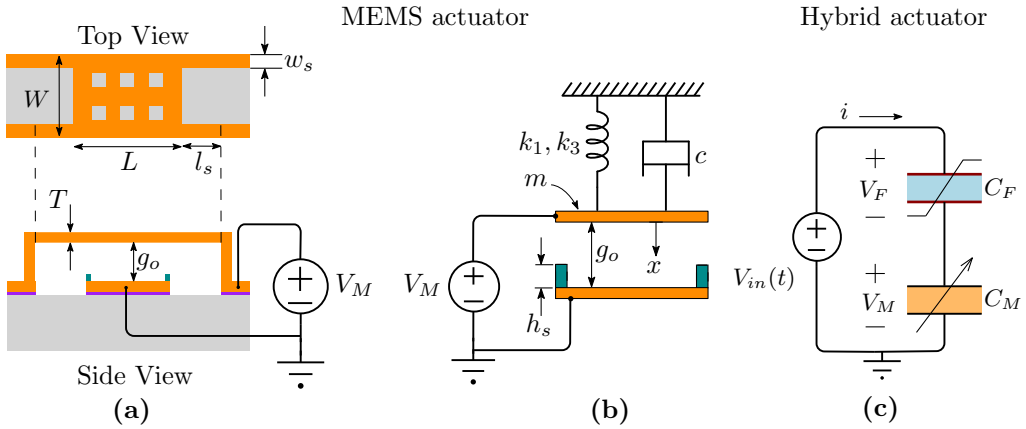


Figure 6.1: (a) Schematic representation of the standalone clamped-clamped MEMS actuator. (b) Single degree of freedom (1-DOF) model of the MEMS actuator. Note that the standalone actuator has both linear spring constant k_1 and cubic spring constant k_3 . (c) Equivalent circuit representation of the hybrid actuator with C_F and C_M denoting the ferroelectric negative capacitance and MEMS capacitance, respectively.

instability in the hybrid actuator. We show that the results obtained are in good agreement with numerical simulations. We also estimate the threshold values of the cubic non-linear spring constant that demarcate the three modes of operation. By proper choice of the cubic spring constant, such that it is close to but greater than the threshold value, we predict that the hybrid actuator can operate at a lower voltage, and without pull-in (always-stable mode), as compared to the standalone actuator.

6.1 REVIEW OF PULL-IN IN ELECTROSTATIC MEMS

The standalone MEMS actuator considered is a clamped-clamped beam with fixed-fixed flexure based on Refs. [3, 7], as shown in Figure 6.1(a). It is modeled using a single degree of freedom (1-DOF) model as shown in Figure 6.1(b). The parameters of the 1-DOF model have the same definitions and values as described in Section 2.1 in Chapter 2. Note that, however, in this chapter, we model the stiffness using a spring having a linear spring constant k_1 and a cubic non-linear spring

constant k_3 (characteristic of a Duffing spring), such that the spring force is, $F_{\text{spring}} = k_1x + k_3x^3$. Mid-plane stretching in a clamped-clamped beam can result in such a cubic non-linearity [7]. Since the pull-in phenomenon is not affected by surface forces [91], we neglect them in our analysis. The damping coefficient c does not affect the analysis as we investigate the static response.

The static response of the **MEMS** actuator is obtained by applying a slowly varying input [1, 26]. When the input voltage exceeds the pull-in voltage, the top electrode snaps down, resulting in pull-in. The maximum distance in the air-gap up to which the actuator can attain a stable equilibrium is called the travel range. For the standalone **MEMS** actuator with a linear spring ($k_3 = 0$), we have the pull-in voltage V_{PI_1} and travel range X_{PI_1} as [1]

$$V_{PI_1} = \sqrt{\frac{8k_1g_o^3}{27\epsilon_o A_M}}; X_{PI_1} = \frac{g_o}{3} \quad (6.1)$$

where g_o , A_M and ϵ_o denote the air-gap, actuation area and permittivity of free space, respectively. The travel range can be extended beyond $g_o/3$ by including a non-linear spring [20], however, with an increased pull-in voltage. For example, with a cubic non-linear spring added ($k_3 \neq 0$), the extended travel range, $X_{PI_2} = \zeta g_o$, is obtained by solving [20]

$$\zeta^3 - \frac{3}{5}\zeta^2 + \frac{3}{5}\eta\zeta - \frac{1}{5}\eta = 0 \quad (6.2)$$

where $\eta = k_1/(k_3g_o^2)$. The maximum possible travel range in this case is $0.6g_o$, which is obtained for a perfectly cubic spring with $\eta = 0$ [20]. Figure 6.2(a) depicts the static characteristics of the standalone **MEMS** actuator with linear ($k_3 = 0$) spring and cubic non-linear ($k_3 \neq 0$) spring, plotted using the parameters from Table 2.1. Based on the design rule given in Ref. [20], for the **MEMS** actuator with cubic non-linear spring, we have chosen $\eta = 0.1$. This gives a travel range, $X_{PI_2} \approx 95\%$ of $0.6g_o$ (note that $0.6g_o$ is the maximum possible travel range, achieved when $\eta = 0$). The stable (unstable) region of operation is characterized by a positive (negative) slope in its static displacement-voltage characteristics [1]. Pull-in instability is not avoided in the standalone **MEMS** with linear and cubic non-linear springs as there exists an unstable region, as depicted in Figure 6.2(a).

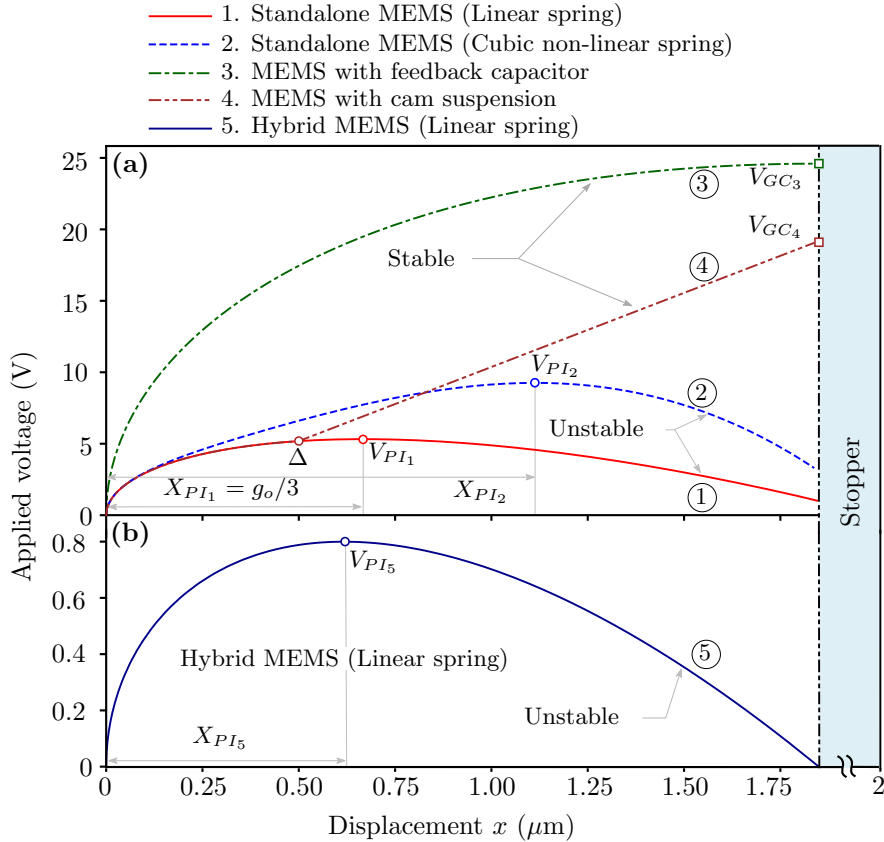


Figure 6.2: (a) Static characteristics of standalone MEMS actuator, feedback capacitor-MEMS actuator and MEMS actuator with cam suspension. Pull-in instability is present in standalone MEMS with linear and non-linear springs, while, it is eliminated in MEMS with a feedback capacitor and in MEMS with cam suspension. (b) Static characteristics of hybrid MEMS actuator with linear spring. Although the pull-in voltage is reduced, pull-in is not eliminated in this configuration.

A feedback capacitor connected in series with the MEMS actuator with linear spring ($k_3 = 0$) can avoid pull-in [21]. In this configuration, the effective electrical air-gap is increased to $g_o(1 + C_o/C_{fb})$, where C_o is the zero-bias MEMS capacitance and C_{fb} is the series feedback capacitance. By proper design of the feedback capacitor C_{fb} , the entire allowed range ($= g_o - h_s$) can be traversed by the movable electrode without pull-in [21]. In this case, the voltage required to close the gap is denoted as V_{GC_3} . Figure 6.2(a) also shows the static characteristics of the feedback capacitor-MEMS configuration. Based on the design criteria to avoid pull-in given in Refs. [21] and for the parameters listed in Table 2.1, we obtain $C_{fb} = 35.91 \text{ fF}$.

Note that the gap-closing voltage V_{GC_3} is significantly greater than the pull-in voltage of the standalone **MEMS** actuator V_{PI_1} , as shown in Figure 6.2(a).

Pull-in can also be eliminated by designing a non-linear spring that counteracts the non-linear electrostatic force [22]. This non-linear spring is realized by using a cam suspension. The design of the cam suspension is detailed in Refs. [22, 96]. The static response for this case is plotted in Figure 6.2(a). The static response follows the response of the standalone **MEMS** actuator with linear spring upto a displacement $\Delta = g_o/4$. Note that Δ should be chosen to be less than $g_o/3$. Beyond Δ , the displacement-voltage response is linear, and thus, pull-in is avoided [22]. As in the case of the **MEMS** with a feedback capacitor, the gap-closing voltage here, V_{GC_4} , is also greater than the pull-in voltage of the standalone **MEMS** actuator V_{PI_1} , as shown in Figure 6.2(a).

Figure 6.1(c) shows the equivalent circuit representation of the hybrid actuator with a ferroelectric capacitor C_F connected in series with the **MEMS** capacitor C_M [17]. The design of the hybrid actuator follows Section 2.3 in Chapter 2 (assuming a linear spring) to obtain a static pull-in voltage of 0.8 V and a pull-out voltage of 0 V. The parameters of the ferroelectric capacitor are listed in Table 2.3. With a linear spring ($k_3 = 0$), the hybrid actuator is predicted to have a reduced pull-in voltage as compared to the standalone actuator [17, 19, 60]. This is illustrated in Figure 6.2(b). A detailed analysis of this configuration is presented in Section 6.3.1. The pull-in voltage V_{PI_5} is less than the pull-in voltage V_{PI_1} of the standalone **MEMS** actuator in Figure 6.2(a). However, the travel range X_{PI_5} is reduced as compared to the standalone **MEMS** actuator and pull-in instability is not eliminated [17], as depicted in Figure 6.2(b). Table 6.1 summarizes pull-in in various **MEMS** configurations.

In this chapter, we propose the elimination of pull-in in the hybrid actuator using a cubic non-linear spring, as explained in the following sections.

Table 6.1: Comparison of various MEMS configurations

Configuration	Spring type	Spring force	Travel range	Operating voltage	Pull-in
1. Standalone MEMS [1]	Linear	k_1x	$g_o/3$	V_{PI_1}	Yes
2. Standalone MEMS [20]	Non-linear	$k_1x + k_3x^3$	$> g_o/3$	$> V_{PI_1}$	Yes
3. MEMS with feedback capacitor [21]	Linear	k_1x	Entire range	$> V_{PI_1}$	No
4. MEMS with cam suspension [22, 96]	Non-linear	$\propto \frac{x^2}{(g_o-x)^2}$	Entire range	$> V_{PI_1}$	No
5. Hybrid MEMS [17]	Linear	k_1x	$< g_o/3$	$< V_{PI_1}$	Yes
6. Hybrid MEMS (this chapter)	Non-linear	$k_1x + k_3x^3$	Entire range	$< V_{PI_1}$	No

6.2 HAMILTONIAN OF THE HYBRID ACTUATOR

The Hamiltonian (total energy) H_M of the 1-DOF electrostatic MEMS actuator, driven by a voltage source V_M , neglecting damping, is given by [20]

$$H_M(x, \dot{x}) = \frac{1}{2} m \dot{x}^2 + U_M(x) \quad (6.3)$$

where \dot{x} is the velocity. The first term on the right side denotes the kinetic energy. The total potential energy U_M , stored in the linear and cubic non-linear springs, and in the capacitor formed by the top and bottom electrodes is expressed as

$$U_M(x) = \frac{1}{2} k_1 x^2 + \frac{1}{4} k_3 x^4 - \frac{1}{2} \frac{\epsilon_0 A_M V_M^2}{(g_o - x)} \quad (6.4)$$

The energy associated with the ferroelectric capacitor is given by [17],

$$U_F(q) = -\frac{1}{2} \alpha q^2 + \frac{1}{4} \beta q^4 + \frac{1}{6} \gamma q^6 - V_F q \quad (6.5)$$

where q is the charge. The voltage across the ferroelectric V_F is given by [17]

$$V_F = -\alpha q + \beta q^3 + \gamma q^5 \quad (6.6)$$

$$\alpha = -\frac{\alpha_F t_F}{A_F}; \beta = \frac{\beta_F t_F}{A_F^3}; \gamma = \frac{\gamma_F t_F}{A_F^5} \quad (6.7)$$

where α_F , β_F and γ_F are ferroelectric anisotropy coefficients, t_F and A_F are the thickness and area of the ferroelectric respectively.

Based on our earlier work in Chapter 4, we use a mapping function between the displacement x and the charge q as

$$q = \frac{\epsilon_0 A_M V_M}{(g_o - x)} \quad (6.8)$$

This mapping function is based on the charge-voltage relationship of a parallel plate capacitor. Applying KVL in Figure 6.1(c), we have, $V_M = V_{in} - V_F$. Therefore Eq. (6.8) can be modified as

$$q = \frac{\epsilon_0 A_M [V_{in} - (-\alpha q + \beta q^3 + \gamma q^5)]}{(g_o - x)} \quad (6.9)$$

The above equation is solved to obtain the charge q as a function of applied voltage V_{in} and displacement x . This charge is then substituted in Eq. (6.5) and Eq. (6.6) to obtain the energy associated with the ferroelectric U_F , in terms of displacement x . Therefore, we obtain the Hamiltonian H_H of the hybrid actuator as

$$H_H(x, \dot{x}) = U_F(x) + H_M(x, \dot{x}) \quad (6.10)$$

The potential energy of the hybrid actuator is thus obtained as

$$U_H(x) = U_F(x) + U_M(x) \quad (6.11)$$

6.3 ANALYSIS OF THE HYBRID ACTUATOR

6.3.1 Hybrid actuator with a linear spring ($k_3 = 0$)

In this section, we analyze the static response of the hybrid actuator with a linear spring ($k_3 = 0$). The ferroelectric capacitor is designed based on the design rules in Ref. [17] (also see Section 2.3 in Chapter 2), to obtain a static pull-in voltage and pull-out voltage of 0.8 V and 0 V, respectively, in the hybrid actuator. The parameters of the ferroelectric capacitor are listed in Table 2.3.

Eq. (6.11) can be used to study the static response by plotting the potential energy-displacement curves for different applied voltages, as shown in Figure 6.3. Note that this is exactly the same as the static pull-in analysis based on energy-displacement landscape in Section 5.2.1 in Chapter 5 (see Figure 5.1). We

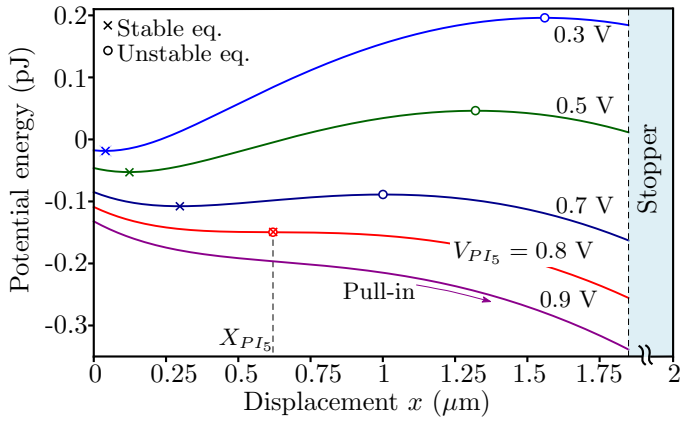


Figure 6.3: Analysis of the static response of the hybrid actuator with linear spring ($k_3 = 0$) using potential energy-displacement plot. The stable (\times) and the unstable (\circ) equilibrium displacements coincide at the static pull-in voltage. Pull-in occurs when the applied voltage exceeds the static pull-in voltage.

include this in this chapter for the sake of completeness of the analysis. For any applied voltage, less than the static pull-in voltage V_{PI5} , there are two equilibrium displacements: stable (local minima, denoted by a \times) and unstable (local maxima, denoted by a \circ). These equilibrium displacements coincide when the input voltage equals the static pull-in voltage, $V_{PI5} = 0.8$ V. The corresponding displacement represents the travel range of the hybrid actuator, $X_{PI5} = 0.62$ μm . The hybrid actuator with linear spring suffers from the pull-in instability, when the applied input exceeds V_{PI5} , as illustrated in Figure 6.3.

6.3.2 Hybrid actuator with a cubic non-linear spring ($k_3 \neq 0$)

In this section, we analyze the static response of the hybrid actuator with the inclusion of a non-linear spring with cubic non-linearity ($k_3 \neq 0$).

Based on Ref. [102], for an applied voltage, the potential energy U_M can be expressed as

$$U_M(x) = \frac{1}{2} k_1 x^2 + \frac{1}{4} k_3 x^4 + \frac{1}{2} \frac{q^2 (g_o - x)}{\epsilon_o A_M} \quad (6.12)$$

At static equilibrium, $dU_M(x)/dx = 0$. Therefore, we have,

$$k_1 x + k_3 x^3 = \frac{q^2}{2 \epsilon_o A_M} \quad (6.13)$$

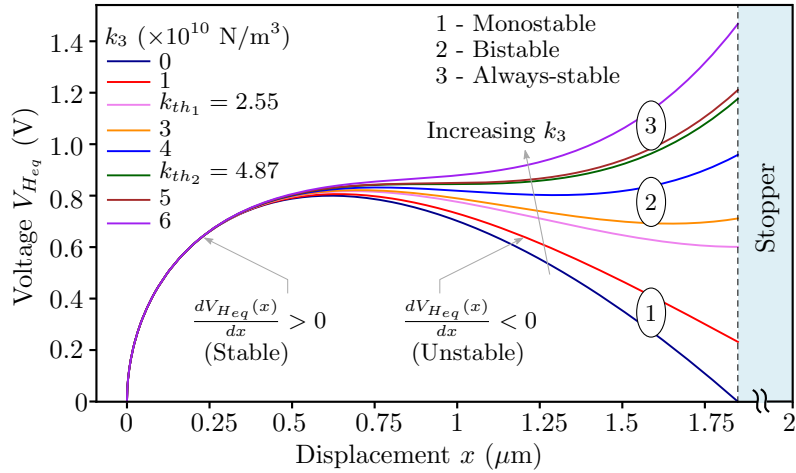


Figure 6.4: Static characteristics of the hybrid actuator for different values of the cubic non-linear spring constant k_3 . For an applied voltage, the number of stable and unstable equilibrium displacements depend on the value of k_3 , giving rise to three possible modes of operation.

Solving the above equation, we obtain the equilibrium charge Q_{eq} as

$$Q_{eq}(x) = \sqrt{2 \epsilon_0 A_M (k_1 x + k_3 x^3)} \quad (6.14)$$

The equilibrium voltage across the MEMS capacitor $V_{M_{eq}}$ is expressed as

$$V_{M_{eq}}(x) = Q_{eq}(x)/C_M = Q_{eq}(x) (g_0 - x)/(\epsilon_0 A_M) \quad (6.15)$$

Using Eq. (6.6), the equilibrium voltage across the ferroelectric capacitor $V_{F_{eq}}$ is given by

$$V_{F_{eq}}(x) = -\alpha Q_{eq}(x) + \beta Q_{eq}^3(x) + \gamma Q_{eq}^5(x) \quad (6.16)$$

Therefore, the equilibrium voltage across the hybrid actuator $V_{H_{eq}}$ is obtained as

$$V_{H_{eq}}(x) = V_{M_{eq}}(x) + V_{F_{eq}}(x) \quad (6.17)$$

Using Eq. (6.17), we plot the equilibrium voltage $V_{H_{eq}}$ as a function of the displacement x for different values of k_3 to obtain the static characteristics of the hybrid actuator, as shown in Figure 6.4. For an applied voltage, depending on the value of k_3 , we can predict three possible modes of operation – (a) monostable (b) bistable and (c) always-stable.

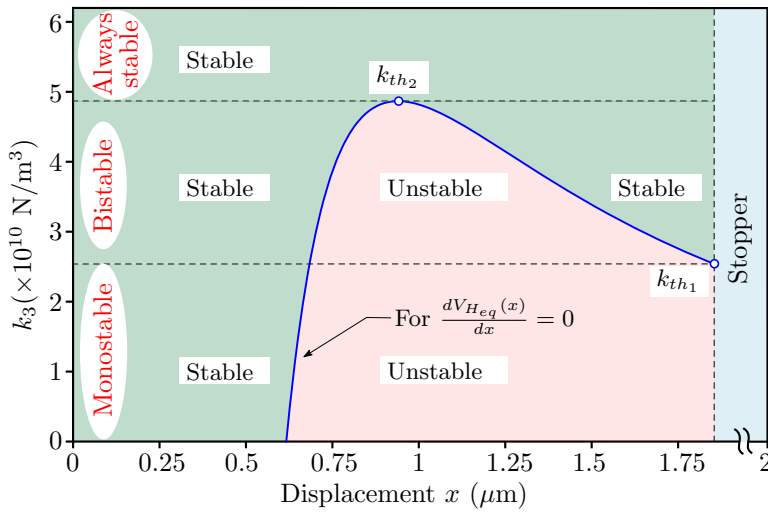


Figure 6.5: Modes of operation in the hybrid actuator based on the cubic non-linear spring constant k_3 : (i) monostable mode for $k_3 < k_{th1}$, (ii) bistable mode for $k_{th1} < k_3 < k_{th2}$, and (iii) always-stable mode for $k_3 > k_{th2}$.

We calculate the threshold values of the cubic non-linear spring constant k_3 that demarcate the different modes of operation. Eq. (6.17) is expanded as

$$V_{Heq}(x) = \frac{Q_{eq}(x)(g_o - x)}{\epsilon_o A_M} - \alpha Q_{eq}(x) + \beta Q_{eq}^3(x) + \gamma Q_{eq}^5(x) \quad (6.18)$$

We solve for k_3 , satisfying the condition $\frac{dV_{Heq}(x)}{dx} = 0 \forall x \in [0, g_o - h_s]$. The resultant solution (see 6.3.2.1 for details), as a function of displacement x , is plotted in Figure 6.5. The value of k_3 at the stopper end (at $x = g_o - h_s$) is denoted as k_{th1} . This threshold value represents the boundary between monostable and bistable modes. The maximum value of k_3 , denoted as threshold value k_{th2} , represents the boundary between the bistable and always-stable modes, as shown in Figure 6.5. Thus, monostable mode occurs for $k_3 < k_{th1}$. For $k_{th1} < k_3 < k_{th2}$, the hybrid actuator operates in bistable mode. Finally, for $k_3 > k_{th2}$, the hybrid actuator is in always-stable mode. For the chosen parameters from Table 3.1, we get $k_{th1} = 2.55 \times 10^{10} \text{ N/m}^3$ and $k_{th2} = 4.87 \times 10^{10} \text{ N/m}^3$.

6.3.2.1 Modes of operation in the hybrid actuator

The boundary between the different modes of operation in Figure 6.5 are obtained by imposing

$$\frac{dV_{H_{eq}}(x)}{dx} = 0 \quad \forall x \in [0, g_o - h_s] \quad (6.19)$$

to obtain k_3 as a function of x . This condition is equivalent to

$$\frac{dV_{H_{eq}}(x)}{dQ_{eq}(x)} = 0 \quad \forall x \in [0, g_o - h_s] \quad (6.20)$$

based on the one-to-one relationship between charge and displacement, at equilibrium, as discussed in Chapter 4. From Eq. (6.18), we get

$$\begin{aligned} \frac{dV_{H_{eq}}(x)}{dQ_{eq}(x)} &= -\alpha + 3\beta Q_{eq}^2(x) + 5\gamma Q_{eq}^4(x) \\ &\quad + \frac{Q_{eq}(x)}{\epsilon_o A_M} \left[-\frac{dx}{dQ_{eq}(x)} \right] + \frac{g_o - x}{\epsilon_o A_M} \end{aligned} \quad (6.21)$$

From Eq. (6.14), we have,

$$\frac{dQ_{eq}(x)}{dx} = \frac{\epsilon_o A_M (k_1 + 3k_3 x^2)}{\sqrt{2\epsilon_o A_M (k_1 x + k_3 x^3)}} \quad (6.22)$$

Substituting the above in Eq. (6.21) and using Eq. (6.14) to substitute for $Q_{eq}(x)$, the condition described by Eq. (6.20) becomes

$$\begin{aligned} -\alpha + 6\beta \epsilon_o A_M (k_1 x + k_3 x^3) + 5\gamma (\epsilon_o A_M (k_1 x + k_3 x^3))^2 \\ + \frac{g_o - x}{\epsilon_o A_M} - \frac{2}{\epsilon_o A_M} \frac{k_1 x + k_3 x^3}{k_1 + 3k_3 x^2} = 0 \end{aligned} \quad (6.23)$$

The above equation is solved (ignoring γ) to obtain an analytical expression for k_3 as a function of x as

$$k_3 = \frac{1}{36\beta \epsilon_o^2 A_M^2 x^5} (p_1 + \sqrt{p_2}) \quad (6.24)$$

where

$$p_1 = 3x^2 (\alpha \epsilon_o A_M - g_o) + x^3 (5 - 24k_1 \beta \epsilon_o^2 A_M^2) \quad (6.25a)$$

$$p_2 = p_1^2 + p_3 \quad (6.25b)$$

$$p_3 = -72 k_1 \beta \epsilon_o^2 A_M^2 x^5 (g_o - \alpha \epsilon_o A_M) + \dots \quad (6.25c)$$

$$216 k_1 \beta \epsilon_o^2 A_M^2 x^6 (1 - 2k_1 \beta \epsilon_o^2 A_M^2)$$

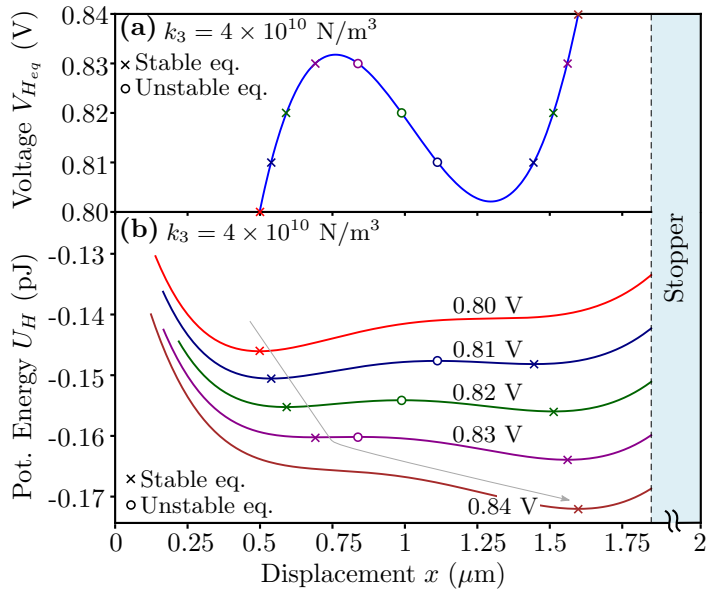


Figure 6.6: (a) Static characteristics of the hybrid actuator, depicting the bistable mode of operation. (b) Corresponding potential energy-displacement plot, depicting the snap-through from one stable equilibrium displacement to other, with increase in voltage. After snap-through, the actuator continues to operate in the stable region.

6.3.2.2 Monostable mode ($k_3 < k_{th_1}$)

This mode has one stable and one unstable equilibrium displacement for an applied voltage. In this mode, the hybrid actuator suffers from the pull-in instability, as in the case of the hybrid actuator with a linear spring. In the static characteristics plotted in Figure 6.4, the region with positive slope represents stable operation, while the region with negative slope represents an unstable region of operation. For example, for $k_3 = 1 \times 10^{10} \text{ N/m}^3$, the hybrid actuator is in the monostable mode, having both stable ($dV_{H_{eq}}(x)/dx > 0$) and unstable ($dV_{H_{eq}}(x)/dx < 0$) regions of operation. The energy-displacement landscape in this mode resembles Figure 6.3. Thus, pull-in is not eliminated in this mode of operation.

6.3.2.3 Bistable mode ($k_{th_1} < k_3 < k_{th_2}$)

This mode has two stable and one unstable equilibrium displacements and resembles the operation of a standalone electrostatic bistable MEMS actuator [101]. For

instance, the static characteristics for $k_3 = 4 \times 10^{10} \text{ N/m}^3$ is shown in Figure 6.6(a). The hybrid actuator, in this case, shows bistable operation. Note that such bistable operation is obtained without the need for any buckling or initial curvature of the clamped-clamped beam [103]. Figure 6.6(b) shows the corresponding potential energy-displacement plot, obtained using Eq. (6.11). In the bistable regime, with increase in voltage, a snap-through from one stable equilibrium displacement to other occurs, similar to the standalone electrostatic bistable MEMS actuator [103]. However, pull-in instability is avoided, because, after the snap-through, the actuator continues to operate in the stable region. This is also verified by comparing the results obtained from the energy-landscape method with the numerical simulation based on Chapter 3. We have added the cubic non-linear spring module in the simulation framework of Chapter 3, to enable the comparison. Figure 6.7 shows the static characteristics obtained using both the methods. The snap-through and hysteresis, which are the characteristic features of the bistable operation, are observed. Note that the energy-landscape approach captures both the stable (positive slope) and unstable (negative slope) regions of operation in the static characteristics, whereas, the numerical simulation captures only the stable operation of the actuator. After the snap-through, the actuator continues to settle at the stable equilibrium displacement corresponding to the applied voltage, thereby, avoiding pull-in. The bistable mode of operation is useful for applications like memories [104], switches [105] and filters [106].

6.3.2.4 Always-stable mode ($k_3 > k_{th_2}$)

Finally, for higher values of the cubic non-linear spring constant k_3 greater than k_{th_2} , the hybrid actuator has only one stable equilibrium displacement for an applied voltage, thereby, avoiding the pull-in instability (*always stable*). For, example, the static characteristics for $k_3 = 5 \times 10^{10} \text{ N/m}^3 (> k_{th_2})$ is shown in Figure 6.8(a). The corresponding potential energy-displacement plot is shown in Figure 6.8(b). For any applied voltage, there exists only one stable equilibrium displacement and hence, the hybrid actuator is always stable (without pull-in). The results obtained using the energy-landscape approach are also in agreement with the numerical

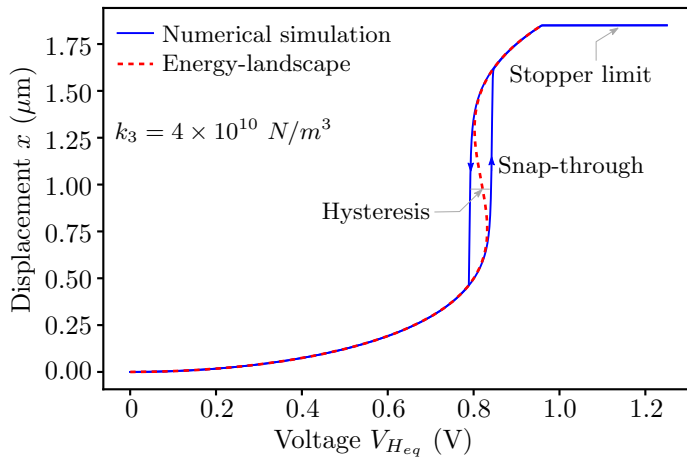


Figure 6.7: Static characteristics of the hybrid actuator obtained using the energy-landscape method and numerical simulation, depicting the bistable mode of operation. Numerical simulation captures only the stable operation, whereas, the energy-landscape method captures both the stable and unstable regions of operation.

simulation based on Chapter 3, as depicted in Figure 6.9. The cubic non-linearity in the spring force is inherently present in clamped-clamped beams [107]. This implies the possibility of avoiding pull-in in the hybrid actuator with a properly designed clamped-clamped beam with appropriate value of k_3 .

With increase in k_3 , over and above k_{th_2} , the voltage required to close the gap increases. For example, in Figure 6.4, comparing the plots with $k_3 = 5 \times 10^{10} \text{ N/m}^3$ and $k_3 = 6 \times 10^{10} \text{ N/m}^3$, a lower voltage is required to close the gap ($= g_0 - h_s = 1.85 \mu\text{m}$) in the case with $k_3 = 5 \times 10^{10} \text{ N/m}^3$. Thus, low-voltage, pull-in free operation of the hybrid actuator, as compared to the standalone MEMS actuator, can be ensured by designing k_3 close to but greater than k_{th_2} . For instance, in Figure 6.8(a), the gap-closing voltage in the hybrid actuator, $V_{GC_6} = 1.21 \text{ V}$, is less than the static pull-in voltage of the standalone MEMS actuator with linear spring (see Figure 6.2(a)), $V_{PI_1} = 5.32 \text{ V}$.

The low-voltage, pull-in free, always-stable mode can find use in various analog positioning applications such as MEMS varactors [7], micromirrors [99], optical switches [108], tunable filters [109] etc. For instance, variable analog capacitors (or varactors) realized using MEMS actuators [7] precisely control the separation between the top and bottom electrodes, based on an applied voltage. These devices

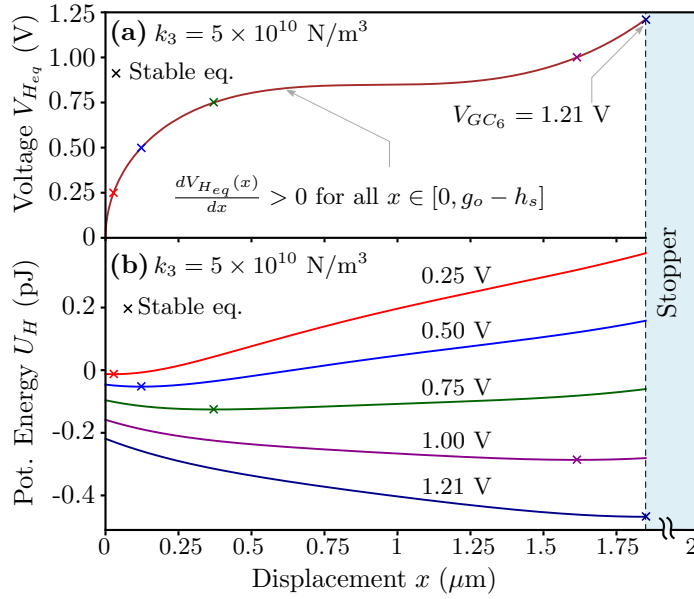


Figure 6.8: (a) Static characteristics of the hybrid actuator, depicting the always-stable mode of operation. In this mode, there exists only one stable equilibrium displacement for an applied voltage. (b) Corresponding potential energy-displacement plot, depicting the presence of stable minima for different applied voltages. The gap-closing voltage is 1.21 V.

are restricted to operate in the stable range of displacement of the movable electrode. In the case of the standalone MEMS actuator with a linear spring, the MEMS capacitance becomes $1.5 \times C_o$ when the applied voltage equals the pull-in voltage V_{PI_1} , as shown in Figure 6.10. Here, C_o is the zero-bias MEMS capacitance. When the applied voltage exceeds V_{PI_1} , pull-in occurs and therefore, the capacitance cannot be controlled. Thus, pull-in instability limits the capacitance ratio to a theoretical value of 1.5 in the standalone MEMS actuator with a linear spring. The elimination of pull-in in the proposed hybrid MEMS actuator (operating in always-stable mode) could increase the capacitance ratio beyond 1.5, due to the increase in stable displacement of the movable plate in the varactor. Furthermore, this extended capacitance tuning range could be achieved at low voltages as compared to the standalone MEMS actuator, as depicted in Figure 6.10.

Various techniques to obtain non-linear spring force are reported in literature. For instance, contact points are used to implement a non-linear spring profile [110]. Partitioned beams and springs with decreasing coil lengths are used to implement

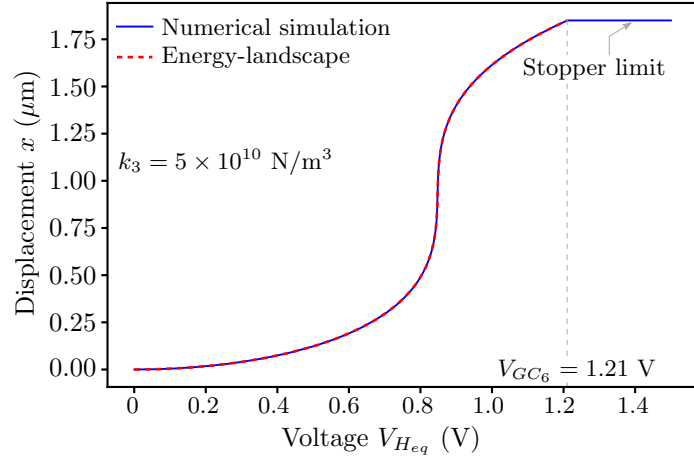


Figure 6.9: Static characteristics of the hybrid actuator obtained using the energy-landscape method and numerical simulation, depicting the always-stable mode of operation. For any applied voltage, there exists only one stable equilibrium displacement.

this technique [110]. Springs with several folds are also used to obtain the non-linearity in the spring force [111]. The non-linearity is determined by the choice of the folding angle. In Ref. [112], the gap between the anchor and the proof-mass is varied to introduce the non-linearity. Ref. [113] reports the use of H-shaped springs to obtain cubic non-linearity. In Ref. [114], tuning of the non-linear cubic spring is achieved using the spring topology variation. Ref. [115] illustrates the presence of cubic non-linearity in the spring force due to stretching in clamped-clamped beams. Further, Ref. [116] illustrates the design of non-linear springs for prescribed load-displacement functions. Thus, by using one or more such techniques, it may be possible to design a non-linear cubic spring such that the hybrid actuator can be made to operate in any of the three distinct modes (monostable, bistable or always-stable), for suitable applications.

6.4 SUMMARY

We have proposed low-voltage, pull-in free, stable operation of a ferroelectric negative-capacitance hybrid MEMS actuator with a cubic non-linear spring. We

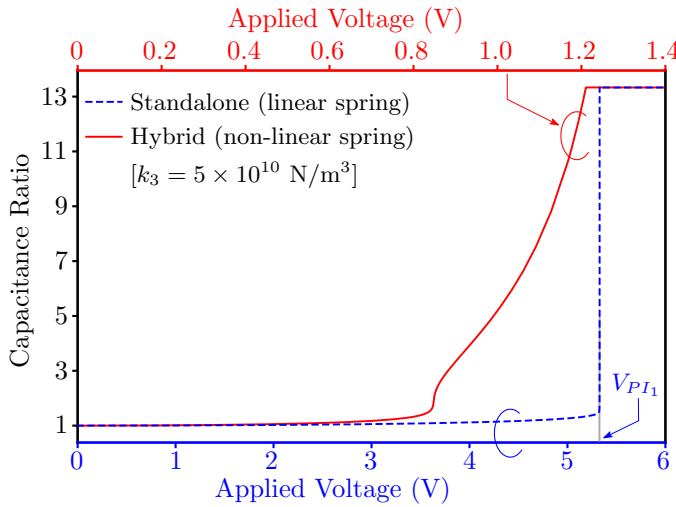


Figure 6.10: Capacitance ratio in MEMS varactor using standalone MEMS with linear spring and hybrid MEMS with cubic non-linear spring (operating in always-stable mode). Note that the capacitance ratio is increased beyond 1.5 in the hybrid MEMS varactor since pull-in is eliminated. Further, this extended capacitance tuning range is achieved at low voltages as compared to the standalone MEMS varactor.

have used a physics-based framework based on the energy-landscape to analyse the response of the hybrid actuator. The framework analyses the hybrid actuator using graphical energy-displacement and voltage-displacement plots. For an applied voltage, based on the value of the cubic non-linear spring constant k_3 , the hybrid actuator has three distinct modes of operation. We have also estimated the threshold values of the cubic non-linear spring constant k_{th_1} and k_{th_2} , that demarcate the three modes of operation. Pull-in is not eliminated in the monostable mode. The bistable mode mimics the operation of a standalone electrostatic bistable MEMS actuator, depicting snap-through and hysteresis in the static characteristics. Pull-in is eliminated in the always-stable mode, wherein there is only one stable equilibrium displacement, for any value of applied voltage. The results obtained using the energy-based framework are in agreement with the numerical simulations and analytical predictions. By proper choice of the cubic non-linear spring constant, close to but greater than k_{th_2} , low-voltage operation without pull-in can be ensured in the hybrid actuator. This work, therefore, can

aid in the design of electrostatic MEMS actuators for low-voltage applications that require an extended travel range without the pull-in instability.

CONCLUSION

We have proposed the modeling of the hybrid actuator using: (i) a [SPICE](#) based framework and (ii) an energy landscape based framework.

The [SPICE](#) based framework numerically solved the coupled non-linear differential equations that describe the hybrid actuator, thereby coupling the electromechanics of the [MEMS](#) actuator with the physics of ferroelectric. Using the proposed framework, we have illustrated the low-voltage operation of the hybrid actuator for both static and dynamic (step) inputs. We have also predicted the reduction in the energy consumption during dynamic pull-in in the hybrid actuator, even in the presence of damping.

The energy landscape based framework used a mapping function that relates the charge and the displacement. This mapping function is valid for both static and dynamic conditions. Hence, this enabled the static and dynamic analysis of the standalone and hybrid actuators, in terms of charge. Based on the charge based description, we also proposed an alternative technique to estimate the parameters of the standalone actuator. The proposed mapping function also led to the formulation of the Hamiltonian of the hybrid actuator, in terms of displacement. Using the energy-displacement framework, we have analyzed the static and dynamic response of the hybrid actuator and have illustrated the low-voltage operation. The results obtained are found to be in good agreement with the numerical simulations based on [SPICE](#) and analytical predictions. Our framework also allowed straightforward inclusion of adhesion between the contacting surfaces. We have shown that the pull-in voltage is unaffected and the pull-out voltage is reduced in the hybrid actuator, due to adhesion.

We have also proposed the elimination of pull-in instability accompanied by low-voltage operation, in the hybrid actuator by adding a non-linear spring (with cubic non-linearity) to it. Based on the value of the cubic spring constant, we have

shown that the hybrid actuator can work in three distinct modes: (i) monostable (ii) bistable and (iii) always-stable. We have also estimated the threshold values of the cubic spring constant that demarcate the aforementioned modes. Finally, we have illustrated the pull-in free and low-voltage operation of the hybrid actuator when it is operated in the always-stable mode.

The proposed modeling frameworks, therefore, can aid in the design and analysis of negative capacitance based low-voltage electrostatic MEMS actuators.

7.1 SCOPE FOR FUTURE WORKS

1. Spring softening effect: In standalone MEMS actuator, the non-linearity of the electrostatic force leads to spring softening effect [1]. The effective spring constant is given by, $k_{\text{eff}} = k - k_{\text{elec}}$, where $k = k_{\text{mech}}$, is the mechanical spring constant and $k_{\text{elec}} = \frac{\epsilon_0 \Lambda_M V_M^2}{(g_0 - \delta)^3}$, is the electrical spring constant. Here, δ is the static equilibrium displacement due to the applied voltage V_M . The effective spring constant is obtained as the curvature of the potential energy with respect to displacement, about the static equilibrium displacement. Therefore, an extension of our proposed energy landscape framework could be taken up later, to study the impact of the ferroelectric negative capacitance on the spring softening effect in the hybrid actuator.
2. Multi-domain ferroelectric: The analysis presented in this thesis assumes that the ferroelectric is homogeneous and single domain, characterized by the 1-D LK equation. In general, the ferroelectric could be made up of multiple domains. The single domain assumption could be relaxed and a more general multi-domain ferroelectric could be considered. Further, recent studies in NCFETs [117–119] show that the presence of a metal layer between the multi-domain ferroelectric and dielectric in the gate stack affects the stabilization of the negative capacitance effect. Thus, the impact of multi-domain ferroelectric on the characteristics of the hybrid actuator could be studied, wherein the ferroelectric is governed by the multi-domain LK equation [120].

3. Different **MEMS** geometries: This thesis analyzes the parallel-plate voltage driven hybrid actuators. The frameworks presented could be extended to analyze hybrid actuators based on other **MEMS** geometries such as cantilever, comb-drive and torsional actuators [1]. The **SPICE** model could be modified accordingly to incorporate the corresponding governing differential equations. In case of the energy landscape framework, a new mapping function has to be formulated for other geometries.
4. Frequency analysis: The dynamic analysis presented in this thesis characterizes the response to step inputs. The proposed frameworks could be extended to analyze the dynamic response of the hybrid actuators to harmonic excitation. This leads to the frequency analysis (displacement-frequency plots) and characterization of resonance in hybrid actuators.

A

APPENDIX

A.1 SPICE MODEL OF STANDALONE ELECTROSTATIC MEMS ACTUATOR

The [SPICE](#) model of a standalone electrostatic [MEMS](#) actuator is detailed in this section. The [SPICE](#) model consists of five modules namely Anchor, Suspension, EOM (Equation Of Motion) solver, Actuator and Adhesion. These are represented as sub-circuits J₁, J₂, J₃, J₄ and J₅ respectively in the [SPICE](#) circuit simulator, as shown in Figure A.1. The other parameters (constants) are modeled as DC voltage sources. Typical values of the [MEMS](#) parameters are shown in the model for reference. For analysis with linear spring, the cubic spring constant k₃ has to be set to zero. Likewise, for analysis without adhesion, the attractive and repulsive constants, C₁ and C₂ have to be set to zero.

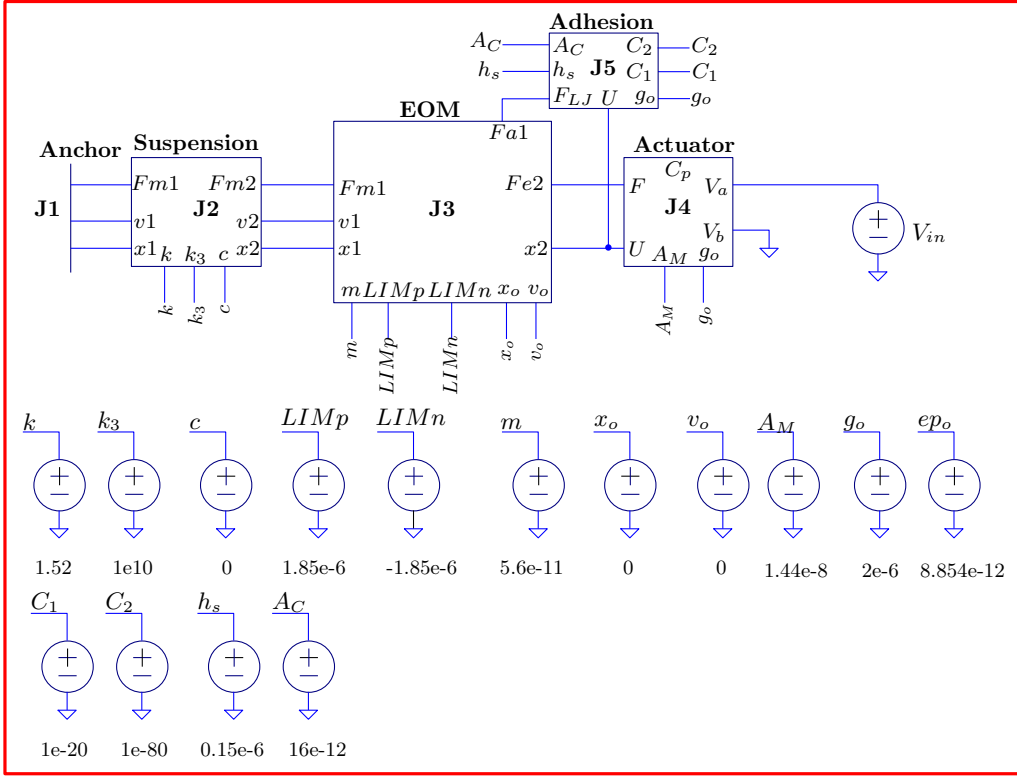


Figure A.1: SPICE model of a standalone electrostatic MEMS actuator implemented in circuit simulator. It consists of five modules: Actuator, Suspension, EOM solver, Anchor and Adhesion, implemented as sub-circuits.

A.1.1 Actuator module

The expanded schematic of the actuator module (sub-circuit J4) is shown in Figure A.2. It accepts the following parameters at the input ports: electrode displacement U , area of the electrode A_M , initial air-gap g_o and the applied input differential voltage V_a and V_b . The input ports are terminated by a 1Ω resistor to convert the signals into voltages so that they can be referenced elsewhere in the module. For example, $V(g_o)$ can be used to refer the initial air-gap g_o . The permittivity of free space ϵ_o is represented as a DC voltage source. The MEMS parallel plate capacitance C_p is calculated using an arbitrary behavioral voltage source B_3 . The actuator module finally computes the electrostatic attractive force F between the

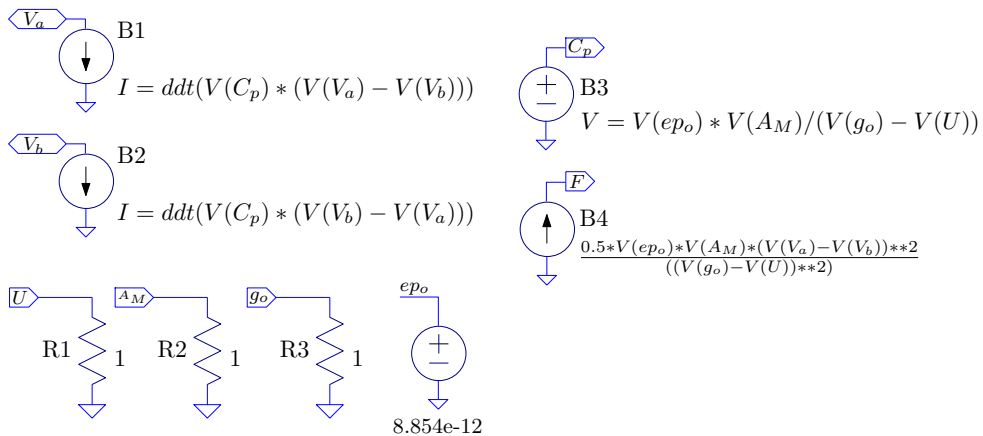


Figure A.2: SPICE sub-circuit implementation of the actuator module. This module outputs the electrostatic force of attraction between the electrodes.

two electrodes using an arbitrary behavioral current source B₄ as per the following equation.

$$F = \frac{\epsilon_o A_M (V_a - V_b)^2}{2 (g_o - U)^2} \quad (\text{A.1.1})$$

A.1.2 Suspension module

The expanded schematic of the suspension module (sub-circuit J₂) is shown in Figure A.3. This module takes the damping coefficient c , spring constant k , cubic spring constant k_3 , the anchor displacement x_1 and the anchor velocity v_1 , the spring displacement x_2 and the spring velocity v_2 as the input parameters. This module calculates the mechanical restoring force as

$$Fm1 = c \frac{dx}{dt} + k x + k_3 x^3 \quad (\text{A.1.2})$$

where x is the dynamic variable representing the displacement. The sign of this mechanical restoring force is made positive on the left-hand side and negative on the right-hand side of the module to indicate the direction of the force. The restoring force is also represented using arbitrary behavioral current sources B₁ and B₂ in the schematic.

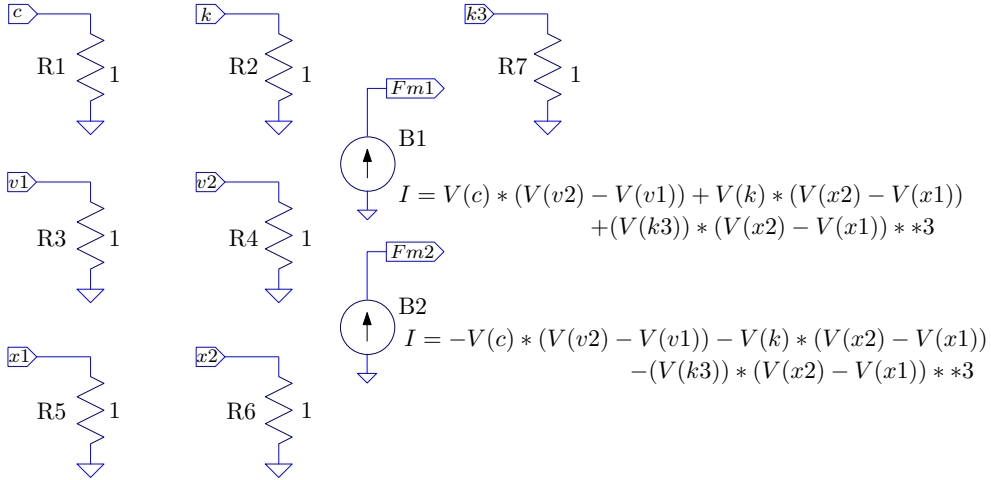


Figure A.3: SPICE sub-circuit implementation of the suspension module. This module outputs the mechanical restoring force.

A.1.3 Adhesion module

The expanded schematic of the adhesion module (sub-circuit J5) is shown in Figure A.4. This module takes the air-gap g_o , electrode displacement U , area of contact A_C , stopper height h_s , attractive and repulsive constants C_1 and C_2 , respectively as the input parameters. This module calculates the force due to adhesion, based on Lennard-Jones potential as

$$F_{LJ} = \frac{C_1 A_C}{\delta^3(x)} - \frac{C_2 A_C}{\delta^9(x)} \quad (\text{A.1.3})$$

where $\delta(x) = g_o - h_s - x$.

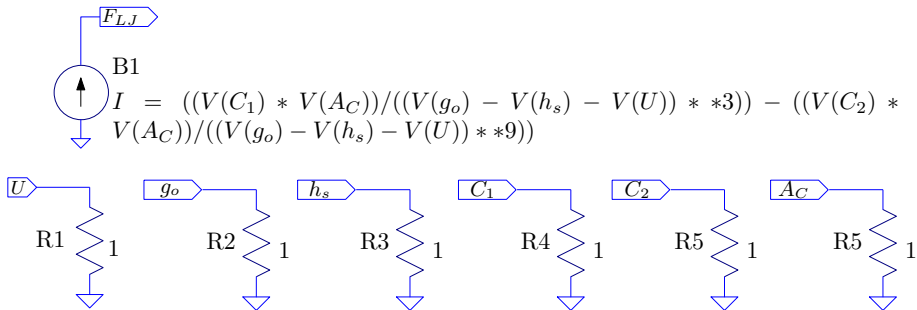


Figure A.4: SPICE sub-circuit implementation of the adhesion module. This module outputs the force due to adhesion, based on Lennard-Jones potential.

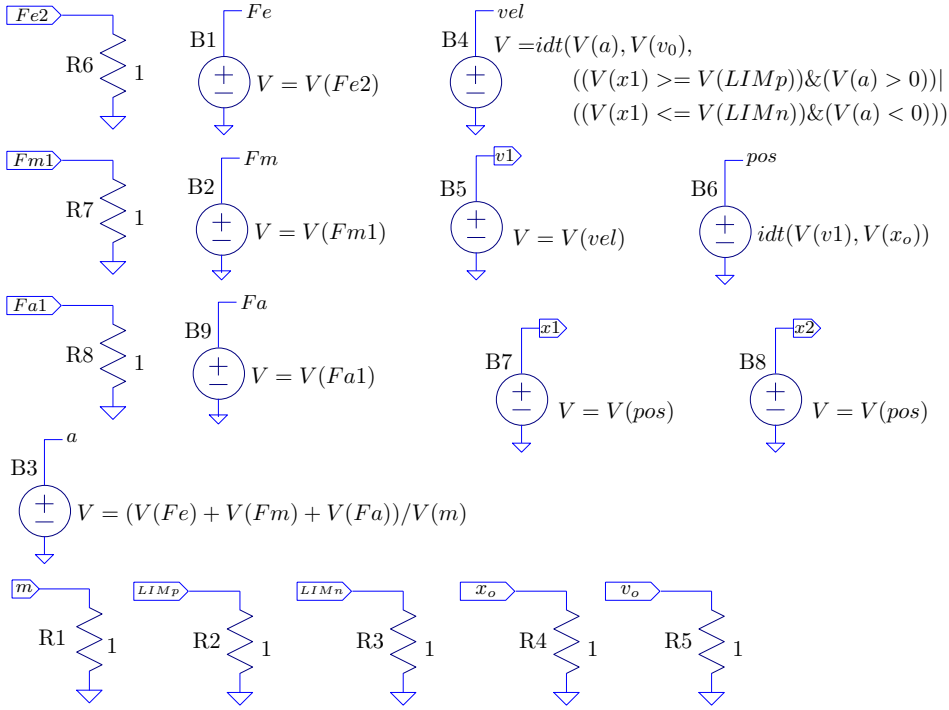


Figure A.5: SPICE sub-circuit implementation of the EOM solver module. This module computes the resultant velocity and displacement by solving the equation of motion describing the MEMS electrostatic actuator.

A.1.4 EOM solver module

The expanded schematic of the Equation Of Motion (EOM) solver module (sub-circuit J₃) is shown in Figure A.5. This module solves the equation of motion governing the MEMS actuator, for an applied input voltage V_{in} , given by

$$m \frac{d^2x}{dt^2} + c \frac{dx}{dt} + k x + k_3 x^3 = \frac{\epsilon_0 A_M V_{in}^2}{2 (g_0 - x)^2} + F_{LJ} \quad (\text{A.1.4})$$

where m is the mass and x is the dynamic variable representing the displacement. This module takes the mechanical restoring force F_{m1} , the electrostatic force F_{e2} and the adhesion force F_{a1} as the input. The acceleration a is then calculated using these three forces and the mass m . The initial displacement x_o and the initial velocity v_o are taken as zero to start the EOM solver module. The acceleration is integrated to compute the velocity vel , which is further integrated to compute the displacement pos . The integration is performed by a built-in function available in the circuit simulator. The computed velocity and displacement are fed back to

the actuator and suspension modules for subsequent calculations so as to reach the solution of the electrode displacement for the applied input voltage V_{in} . The displacement of the movable electrode is limited by the stopper. This is modeled using if-else clause available in SPICE.

A.1.5 Anchor module

The expanded schematic of the anchor module (sub-circuit J1) is shown in Figure A.6. This module is designed to terminate the output current (F_{m1}) coming from the suspension module into the electrical ground. It also provides ground potential to the displacement x and velocity v coming out from this module.

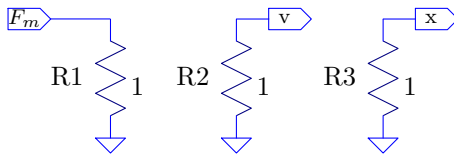


Figure A.6: SPICE sub-circuit implementation of the anchor module. This module provides the termination into the electrical ground.

A.2 SPICE NETLIST OF HYBRID MEMS ACTUATOR

```

* SPICE netlist for hybrid actuator
* Created by Raghuram Tattamangalam Raman and Arvind Ajoy
* Electrical Engineering, IIT Palakkad, Palakkad, India
* Released under Creative Commons Attribution license
* Version 3.0 Date: May 01, 2022

XX2 N004 N003 N006 N008 N007 N009 k c k3 sus
XX4 N002 x V_amp 0 S g NC_01 ppa
XX1 NC_02 N004 N006 N008 anc
VC1 c 0 0
vxil x0 0 0
vil v0 0 0

```

```

vml m 0 5.6e-11
vl1 LIMp 0 1.85e-6
vgini1 g 0 2e-6
vs1 S 0 1.44e-8
vl2 LIMn 0 -1.85e-6
VK1 k 0 1.52
vep1 ep 0 8.854e-12
VDD1 P001 0 PWL(0 0 50m 1.8) Rser=1
V99 P001 N005 0
F1 0 N011 V99 1
C1 N011 0 1
R1 N011 0 1G
E1 Q 0 N011 0 1
B1 N010 0 V=-V(alpha)*V(Q)+V(beta)*(V(Q)*V(Q)*V(Q))+  

+ V(gamma)*(V(Q)*V(Q)*V(Q)*V(Q)*V(Q))
E2 N005 V_amp N010 0 1
V1 t1 0 45.24e-9
V2 area 0 9.87e-12
V3 alphad 0 -2.88e9
V4 betad 0 3.56e11
B2 alpha 0 V=(-V(alphad)*V(t1))/V(area)
B3 beta 0 V=(V(betad)*V(t1))/(V(area)*V(area)*V(area))
B4 gamma 0 V=(V(gammad)*V(t1))/(V(area)*V(area)*V(area)*V(area))
V6 gammad 0 0
VK2 k3 0 0
XX6 N001 x g C1 C2 Acon hs adh
XX3 NC_03 N003 N002 NC_04 N007 N009 NC_05 x m LIMp LIMn x0 v0 N001 eom
V50 C1 0 1e-20
V51 C2 0 1e-80
V52 hs 0 1.5e-7
V53 Acon 0 16e-12

```

```

* block symbol definitions

.subckt sus Fm1 Fm2 v1 x1 v2 x2 k c k3
R1 0 c 1
R2 0 k 1
R3 0 v1 1
R4 0 v2 1
R5 0 x1 1
R6 0 x2 1
B1 0 Fm1 I=V(c)*(V(v2)-V(v1))+V(k)*(V(x2)-V(x1))+(V(k3))*(V(x2)-V(x1))**3
B2 0 Fm2 I=-1*V(c)*(V(v2)-V(v1))-V(k)*(V(x2)-V(x1))-(V(k3))*(V(x2)-V(x1))**3
R7 0 k3 1
.ends sus

.subckt ppa F u Vd Vb S g Cp
R1 0 u 1
B1 0 F I=(1/2)*V(ep)*V(S)*(V(Vd)-V(Vb))**2/((V(g)-V(u))**2)
R2 0 S 1
R3 0 g 1
vep1 ep 0 8.854e-12
B2 Vd 0 I=ddt(V(Cp)*(V(Vd)-V(Vb)))
B3 Vb 0 I=ddt(V(Cp)*(V(Vb)-V(Vd)))
B4 Cp 0 V=V(ep)*V(S)/(V(g)-V(u))
.ends ppa

.subckt adh F u g C1 C2 Acon hs
R1 0 u 1
B1 0 F I=((V(C1)*V(Acon))/((V(g)-V(hs)-V(u))**3))-  

+ ((V(C2)*V(Acon))/((V(g)-V(hs)-V(u))**9))
R3 0 g 1

```

```

R2 0 hs 1
R4 0 C1 1
R5 0 C2 1
R6 0 Acon 1
.ends adh

.subckt eom Fe1 Fm1 Fe2 Fm2 v1 x1 v2 x2 m LIMp LIMn x0 v0 Fa1
R1 m 0 1
R2 LIMp 0 1
R3 LIMn 0 1
R4 x0 0 1
R5 v0 0 1
R6 Fe1 0 1
R7 Fe2 0 1
R8 Fm1 0 1
R9 Fm2 0 1
B1 Fe 0 V=V(Fe1)+V(Fe2)
B2 Fm 0 V=V(Fm1)+V(Fm2)
B3 a 0 V=(V(Fe)+V(Fm)+V(Fa))/V(m)
B4 vel 0 V=idt(V(a),V(v0),((V(x1)>=V(LIMp))&(V(a)>0))|((V(x1)<=V(LIMn))&(V(a)<0)))
B5 v1 0 V=V(vel)
B6 v2 0 V=V(vel)
B7 pos 0 V=idt(V(v1),V(x0))
B8 x1 0 V=V(pos)
B9 x2 0 V=V(pos)
R10 Fa1 0 1
B10 Fa 0 V=V(Fa1)
.ends eom

.subckt anc Fe Fm v x
R1 0 Fe 1

```

```
R2 0 Fm 1  
R3 0 v 1  
R4 0 x 1  
.ends anc  
  
.tran 0 85m 0 5e-8  
.backanno  
.end
```

BIBLIOGRAPHY

- [1] Mohammad I Younis. *MEMS Linear and Nonlinear Statics and Dynamics*. Vol. 20. Boston, MA: Springer US, 2011.
- [2] K J Vinoy, G K Ananthasuresh, Rudra Pratap, and S B Krupanidhi. *Micro and Smart Devices and Systems*. Springer, 2014.
- [3] Sudhanshu Shekhar, K J Vinoy, and G K Ananthasuresh. "Surface-micromachined capacitive RF switches with low actuation voltage and steady contact." In: *J. Microelectromech. Syst.* 26.3 (2017). doi:[10.1109/JMEMS.2017.2688519](https://doi.org/10.1109/JMEMS.2017.2688519), pp. 643–652.
- [4] James J Allen. *Introduction to MEMS (MicroElectroMechanical Systems)*. Tech. rep. Sandia National Lab, Albuquerque, US, 2007.
- [5] FT-G Microgripper. <https://www.femtotools.com/previousproducts/ft-g-microgripper>. Accessed: 2022-03-13.
- [6] Abdullah Saleh Algarni, Mohd Haris Md Khir, John Ojur Dennis, Abdelaaziz Yousif Ahmed, Sami Sultan Alabsi, Saeed Salem Ba Hashwan, and Mohammed M Junaid. "A review of actuation and sensing mechanisms in MEMS-based sensor devices." In: *Nanoscale Research Lett.* 16.1 (2021). doi:[10.1186/s11671-021-03481-7](https://doi.org/10.1186/s11671-021-03481-7), pp. 1–21.
- [7] Gabriel M Rebeiz. *RF MEMS: Theory, Design, and Technology*. John Wiley & Sons, 2004.
- [8] Vikas Choudhary and Krzysztof Iniewski. *MEMS: Fundamental Technology and Applications*. CRC Press, 2016.
- [9] Mohamed Gad-el Hak. *MEMS: Applications*. CRC press, 2005.
- [10] Tai-Ran Hsu. *MEMS & Microsystems: Design and Manufacture*. McGraw-Hill, 2002.

- [11] 2018 International Roadmap for Devices and Systems (IRDS). Tech. rep. 2018.
- [12] Dominicus J IJntema and Harrie AC Tilmans. "Static and dynamic aspects of an air-gap capacitor." In: *Sens. Actuators, Phys. A* 35.2 (1992). doi:[10.1016/0924-4247\(92\)80150-2](https://doi.org/10.1016/0924-4247(92)80150-2), pp. 121–128.
- [13] Norbert Dumas, Laurent Latorre, Frederick Mailly, and Pascal Nouet. "Design of a smart CMOS high-voltage driver for electrostatic MEMS switches." In: *Symp. Design Test Integration and Packag. of MEMS/MOEMS (DTIP)*. 2010, pp. 44–47.
- [14] James A Brandt. "High voltage bias waveform generator for an RF MEMS microswitch." MA thesis. University of New Hampshire, Durham, 2008.
- [15] Jeong Oen Lee, Yong-Ha Song, Min-Wu Kim, Min-Ho Kang, Jae-Sub Oh, Hyun-Ho Yang, and Jun-Bo Yoon. "A sub-1-volt nanoelectromechanical switching device." In: *Nature Nanotech.* 8.1 (2013). doi:[10.1038/nnano.2012.208](https://doi.org/10.1038/nnano.2012.208), pp. 36–40.
- [16] Chytra Pawashe, Kevin Lin, and Kelin J Kuhn. "Scaling limits of electrostatic nanorelays." In: *IEEE Trans. Electron Devices* 60.9 (2013). doi:[10.1109/TED.2013.2273217](https://doi.org/10.1109/TED.2013.2273217), pp. 2936–2942.
- [17] Muhammad Masuduzzaman and Muhammad Ashraful Alam. "Effective nanometer airgap of NEMS devices using negative capacitance of ferroelectric materials." In: *Nano Lett.* 14.6 (2014). doi:[10.1021/nl5004416](https://doi.org/10.1021/nl5004416), pp. 3160–3165.
- [18] Sayeef Salahuddin and Supriyo Datta. "Use of negative capacitance to provide voltage amplification for low power nanoscale devices." In: *Nano Lett.* 8.2 (2008). doi:[10.1021/nl071804g](https://doi.org/10.1021/nl071804g), pp. 405–410.
- [19] Kihun Choe and Changhwan Shin. "Adjusting the operating voltage of an nanoelectromechanical relay using negative capacitance." In: *IEEE Trans. Electron Devices* 64.12 (2017). doi:[10.1109/TED.2017.2756676](https://doi.org/10.1109/TED.2017.2756676), pp. 5270–5273.

- [20] Yael Nemirovsky and Ofir Bochobza-Degani. "A methodology and model for the pull-in parameters of electrostatic actuators." In: *J. Microelectromech. Syst.* 10.4 (2001). doi:[10.1109/84.967384](https://doi.org/10.1109/84.967384), pp. 601–615.
- [21] Joseph I Seeger and Selden B Crary. "Stabilization of electrostatically actuated mechanical devices." In: *Proc. Int. Solid State Sensors and Actuators Conf. (Transducers' 97)*. Vol. 2. doi:[10.1109/SENSOR.1997.635402](https://doi.org/10.1109/SENSOR.1997.635402). IEEE. 1997, pp. 1133–1136.
- [22] Shai Shmulevich, Ben Rivlin, Inbar Hotzen, and David Elata. "A gap-closing electrostatic actuator with a linear extended range." In: *J. Microelectromech. Syst.* 22.5 (2013). doi:[10.1109/JMEMS.2013.2276027](https://doi.org/10.1109/JMEMS.2013.2276027), pp. 1109–1114.
- [23] Jacopo Iannacci, Alena Repchankova, David Macii, and Martin Niessner. "A measurement procedure of technology-related model parameters for enhanced RF-MEMS design." In: *2009 IEEE Int. Workshop on Advanced Methods for Uncertainty Estimation in Measurement*. doi:[10.1109/AMUEM.2009.5207609](https://doi.org/10.1109/AMUEM.2009.5207609). IEEE. 2009, pp. 44–49.
- [24] F Giacomzzi and Jacopo Iannacci. "RF MEMS technology for next-generation wireless communications." In: *Handbook of MEMS for Wireless and Mobile Applications*. doi:[10.1533/9780857098610.1.225](https://doi.org/10.1533/9780857098610.1.225). Elsevier, 2013, pp. 225–257.
- [25] Shilpi Pandey, Deepak Bansal, Prachi Jhanwar, Seema Verma, and KJ Rangra. "Design of Reliable Analog DMTL Phase Shifter with Improved Performance for Ku Band Applications." In: *Defence Science Journal* 65.5 (2015). doi:[10.14429/dsj.65.8377](https://doi.org/10.14429/dsj.65.8377).
- [26] Joachim Oberhammer and Goran Stemme. "Accuracy of quasi-static simulation methods as compared to full-dynamic analysis of nonlinear electrostatic MEMS actuators." In: *2007 IEEE 20th Int. Conf. MEMS*. doi:[10.1109/MEMSYS.2007.4432961](https://doi.org/10.1109/MEMSYS.2007.4432961). IEEE. 2007, pp. 187–190.
- [27] Hiroshi Toshiyoshi. "A SPICE-based multi-physics simulation technique for integrated MEMS." In: *IEEE Int. Conf. Simulation of Semiconductor Processes and Devices*. doi:[10.1109/SISPAD.2011.6035069](https://doi.org/10.1109/SISPAD.2011.6035069). 2011, pp. 239–242.

- [28] Gregory N Nielson and George Barbastathis. "Dynamic pull-in of parallel-plate and torsional electrostatic MEMS actuators." In: *J. Microelectromech. Syst.* 15.4 (2006). doi:[10.1109/JMEMS.2006.879121](https://doi.org/10.1109/JMEMS.2006.879121), pp. 811–821.
- [29] Kenji Uchino. *Ferroelectric Devices*. CRC press, 2018.
- [30] Yang Li, Yong Lian, and Ganesh S Samudra. "Quantitative analysis and prediction of experimental observations on quasi-static hysteretic metal–ferroelectric–metal–insulator–semiconductor FET and its dynamic behaviour based on Landau theory." In: *Semiconductor Science and Technology* 30.4 (2015). doi:[10.1088/0268-1242/30/4/045011](https://doi.org/10.1088/0268-1242/30/4/045011), p. 045011.
- [31] Asif Islam Khan, Korok Chatterjee, Brian Wang, Steven Drapcho, Long You, Claudio Serrao, Saidur Rahman Bakaul, Ramamoorthy Ramesh, and Sayeef Salahuddin. "Negative capacitance in a ferroelectric capacitor." In: *Nature Mater.* 14.2 (2015). doi:[10.1038/nmat4148](https://doi.org/10.1038/nmat4148), pp. 182–186.
- [32] Ali Saeidi, Teodor Rosca, Elvedin Memisevic, Igor Stolichnov, Matteo Cavalieri, Lars-Erik Wernersson, and Adrian M Ionescu. "Nanowire tunnel FET with simultaneously reduced subthermionic subthreshold swing and off-current due to negative capacitance and voltage pinning effects." In: *Nano Lett.* 20.5 (2020). doi:[10.1021/acs.nanolett.9b05356](https://doi.org/10.1021/acs.nanolett.9b05356), pp. 3255–3262.
- [33] Asif Islam Khan, Korok Chatterjee, Juan Pablo Duarte, Zhongyuan Lu, Angada Sachid, Sourabh Khandelwal, Ramamoorthy Ramesh, Chenming Hu, and Sayeef Salahuddin. "Negative capacitance in short-channel FinFETs externally connected to an epitaxial ferroelectric capacitor." In: *IEEE Electron Device Lett.* 37.1 (2015). doi:[10.1109/LED.2015.2501319](https://doi.org/10.1109/LED.2015.2501319), pp. 111–114.
- [34] Yang Li. "Negative Capacitance Ferroelectric MOSFET for Low Power Circuits: Potential and Limitations." PhD thesis. National University of Singapore, 2017. URL: <https://scholarbank.nus.edu.sg/handle/10635/136521>.
- [35] Xudong Wang, Yan Chen, Guangjian Wu, Dan Li, Luqi Tu, Shuo Sun, Hong Shen, Tie Lin, Yongguang Xiao, Minghua Tang, et al. "Two-dimensional negative capacitance transistor with polyvinylidene fluoride-based ferroelectric

- polymer gating." In: *NPJ 2D Mater. and Appl.* 1.1 (2017). doi:[10.1038/s41699-017-0040-4](https://doi.org/10.1038/s41699-017-0040-4), pp. 1–7.
- [36] Mengwei Si et al. "Steep-slope hysteresis-free negative capacitance MoS₂ transistors." In: *Nature Nanotechnol.* 13.1 (2018). doi:[10.1038/s41565-017-0010-1](https://doi.org/10.1038/s41565-017-0010-1), pp. 24–28.
- [37] Daniel JR Appleby, Nikhil K Ponon, Kelvin SK Kwa, Bin Zou, Peter K Petrov, Tianle Wang, Neil M Alford, and Anthony O'Neill. "Experimental observation of negative capacitance in ferroelectrics at room temperature." In: *Nano Lett.* 14.7 (2014). doi:[10.1021/nl5017255](https://doi.org/10.1021/nl5017255), pp. 3864–3868.
- [38] Masaharu Kobayashi and Toshiro Hiramoto. "On device design for steep-slope negative-capacitance field-effect-transistor operating at sub-0.2 V supply voltage with ferroelectric HfO₂ thin film." In: *AIP Advances* 6.2 (2016). doi:[10.1063/1.4942427](https://doi.org/10.1063/1.4942427), p. 025113.
- [39] Luqi Tu, Xudong Wang, Jianlu Wang, Xiangjian Meng, and Junhao Chu. "Ferroelectric negative capacitance field effect transistor." In: *Adv. Electron. Mater.* 4.11 (2018). doi:[10.1002/aelm.201800231](https://doi.org/10.1002/aelm.201800231), p. 1800231.
- [40] Hansol Ku and Changhwan Shin. "Transient response of negative capacitance in P(VDF_{0.75}-TrFE_{0.25}) organic ferroelectric capacitor." In: *IEEE J. Electron Devices Soc.* 5.3 (2017). doi:[10.1109/JEDS.2017.2670546](https://doi.org/10.1109/JEDS.2017.2670546), pp. 232–236.
- [41] Michael Hoffmann, Milan Pešić, Korok Chatterjee, Asif I Khan, Sayeef Salahuddin, Stefan Slesazeck, Uwe Schroeder, and Thomas Mikolajick. "Direct observation of negative capacitance in polycrystalline ferroelectric HfO₂." In: *Adv. Functional Mater.* 26.47 (2016). doi:[10.1002/adfm.201602869](https://doi.org/10.1002/adfm.201602869), pp. 8643–8649.
- [42] Pankaj Sharma, Jianchi Zhang, Kai Ni, and Suman Datta. "Time-resolved measurement of negative capacitance." In: *IEEE Electron Device Lett.* 39.2 (2017). doi:[10.1109/LED.2017.2782261](https://doi.org/10.1109/LED.2017.2782261), pp. 272–275.

- [43] Michael Hoffmann, Franz PG Fengler, Melanie Herzig, Terence Mittmann, Benjamin Max, Uwe Schroeder, Raluca Negrea, Pintilie Lucian, Stefan Slesazeck, and Thomas Mikolajick. "Unveiling the double-well energy landscape in a ferroelectric layer." In: *Nature* 565.7740 (2019). doi:[10.1038/s41586-018-0854-z](https://doi.org/10.1038/s41586-018-0854-z), pp. 464–467.
- [44] Asif Islam Khan, Debanjan Bhowmik, Pu Yu, Sung Joo Kim, Xiaoqing Pan, Ramamoorthy Ramesh, and Sayeef Salahuddin. "Experimental evidence of ferroelectric negative capacitance in nanoscale heterostructures." In: *Appl. Phys. Lett.* 99.11 (2011). doi:[10.1063/1.3634072](https://doi.org/10.1063/1.3634072), p. 113501.
- [45] Weiwei Gao, Asif Khan, Xavi Martí, Chris Nelson, Claudio Serrao, Jayakanth Ravichandran, Ramamoorthy Ramesh, and Sayeef Salahuddin. "Room-temperature negative capacitance in a ferroelectric–dielectric superlattice heterostructure." In: *Nano Lett.* 14.10 (2014). doi:[10.1021/nl502691u](https://doi.org/10.1021/nl502691u), pp. 5814–5819.
- [46] Pavlo Zubko, Jacek C Wojdeł, Marios Hadjimichael, Stéphanie Fernandez-Pena, Anaïs Sené, Igor Luk'yanchuk, Jean-Marc Triscone, and Jorge Íñiguez. "Negative capacitance in multidomain ferroelectric superlattices." In: *Nature* 534.7608 (2016). doi:[10.1038/nature17659](https://doi.org/10.1038/nature17659), pp. 524–528.
- [47] Nujhat Tasneem, Prasanna Venkatesan Ravindran, Zheng Wang, Jorge Gomez, Jae Hur, Shimeng Yu, Suman Datta, and Asif Islam Khan. "Differential charge boost in hysteretic ferroelectric–dielectric heterostructure capacitors at steady state." In: *Appl. Phys. Lett.* 118.12 (2021). doi:[10.1063/5.0035880](https://doi.org/10.1063/5.0035880), p. 122901.
- [48] Ali Saeidi, Farzan Jazaeri, Igor Stolichnov, Gia V Luong, Qing-Tai Zhao, Siegfried Mantl, and Adrian M Ionescu. "Effect of hysteretic and non-hysteretic negative capacitance on tunnel FETs DC performance." In: *Nanotechnol.* 29.9 (2018). doi:[10.1088/1361-6528/aaa590](https://doi.org/10.1088/1361-6528/aaa590), p. 095202.
- [49] Asif I Khan, Michael Hoffmann, Korok Chatterjee, Zhongyuan Lu, Rui-juan Xu, Claudio Serrao, Samuel Smith, Lane W Martin, Chenming Hu, Ramamoorthy Ramesh, et al. "Differential voltage amplification from fer-

- roelectric negative capacitance." In: *Appl. Phys. Lett.* 111.25 (2017). doi:[10.1063/1.5006958](#), p. 253501.
- [50] Eunah Ko, Jae Woo Lee, and Changhwan Shin. "Negative capacitance FinFET with sub-20-mV/decade subthreshold slope and minimal hysteresis of 0.48 V." In: *IEEE Electron Device Lett.* 38.4 (2017). doi:[10.1109/LED.2017.2672967](#), pp. 418–421.
- [51] Hyunwoo Choi and Changhwan Shin. "Negative Capacitance Transistor with Two-Dimensional Channel Material (Molybdenum disulfide, MoS₂)."
In: *physica status solidi (a)* 216.16 (2019). doi:[10.1002/pssa.201900177](#), p. 1900177.
- [52] Jaesung Jo and Changhwan Shin. "Negative capacitance field effect transistor with hysteresis-free sub-60-mV/decade switching." In: *IEEE Electron Device Lett.* 37.3 (2016). doi:[10.1109/LED.2016.2523681](#), pp. 245–248.
- [53] M Hoffmann, B Max, T Mittmann, U Schroeder, S Slesazeck, and T Mikolajick. "Demonstration of high-speed hysteresis-free negative capacitance in ferroelectric Hf_{0.5}Zr_{0.5}O₂." In: *2018 IEEE IEDM*. doi:[10.1109/IEDM.2018.8614677](#). IEEE. 2018.
- [54] Masaharu Kobayashi, Nozomu Ueyama, Kyungmin Jang, and Toshiro Hiramoto. "Experimental study on polarization-limited operation speed of negative capacitance FET with ferroelectric HfO₂." In: *2016 IEEE IEDM*. doi:[10.1109/IEDM.2016.7838402](#). IEEE. 2016.
- [55] T Mikolajick, S Slesazeck, H Mulaosmanovic, MH Park, S Fichtner, PD Lomenzo, M Hoffmann, and U Schroeder. "Next generation ferroelectric materials for semiconductor process integration and their applications." In: *J. Appl. Phys.* 129.10 (2021). doi:[10.1063/5.0037617](#), p. 100901.
- [56] Giovanni A Salvatore, Alexandru Rusu, and Adrian M Ionescu. "Experimental confirmation of temperature dependent negative capacitance in ferroelectric field effect transistor." In: *Appl. Phys. Lett.* 100.16 (2012). doi:[10.1063/1.4704179](#), p. 163504.

- [57] Gregory N Nielson, Roy H Olsson, Gregory Robert Bogart, Paul R Resnick, Olga B Spahn, C Tigges, GRANT Grossetete, and George Barbastathis. "Dynamic pull-in and switching for sub-pull-in voltage electrostatic actuation." In: *Proc. 14th Int. Conf. Solid-State Sens., Actuators, Microsyst. (TRANSDUCERS)*. doi:[10.1109/SENSOR.2007.4300166](https://doi.org/10.1109/SENSOR.2007.4300166). 2007, pp. 455–459.
- [58] Ki Bang Lee. *Principles of Microelectromechanical Systems*. Hoboken, NJ, USA: John Wiley & Sons, 2011.
- [59] Vitaly Leus and David Elata. "On the dynamic response of electrostatic MEMS switches." In: *J. Microelectromech. Syst.* 17.1 (2008). doi:[10.1109/JMEMS.2007.908752](https://doi.org/10.1109/JMEMS.2007.908752), pp. 236–243.
- [60] Kihun Choe and Changhwan Shin. "Ferroelectric-gated nanoelectromechanical nonvolatile memory cell." In: *IEEE Trans. Electron Devices* 66.1 (2018). doi:[10.1109/TED.2018.2881201](https://doi.org/10.1109/TED.2018.2881201), pp. 407–412.
- [61] Kihun Choe and Changhwan Shin. "Impact of negative capacitance on the energy-delay property of an electromechanical relay." In: *Jpn. J. Appl. Phys.* 58.5 (2019). doi:[10.7567/1347-4065/ab0ee7](https://doi.org/10.7567/1347-4065/ab0ee7), p. 051003.
- [62] Chankeun Yoon, Kihun Choe, and Changhwan Shin. "Energy-Delay Sensitivity Analysis of a Nanoelectromechanical Relay With the Negative Capacitance of a Ferroelectric Capacitor." In: *IEEE J. Electron Devices Soc.* 8 (2020). doi:[10.1109/JEDS.2020.2983197](https://doi.org/10.1109/JEDS.2020.2983197), pp. 365–372.
- [63] Andre Vladimirescu. *The SPICE Book*. John Wiley & Sons, Inc., 1994.
- [64] Alessandro Granaldi and Paolo Decuzzi. "The dynamic response of resistive microswitches: switching time and bouncing." In: *J. Micromech. Microeng.* 16.7 (2006). doi:[10.1088/0960-1317/16/7/002](https://doi.org/10.1088/0960-1317/16/7/002), p. 1108.
- [65] H Toshiyoshi, T Konishi, K Machida, and K Masu. "A Multi-physics Simulation Technique for Integrated MEMS." In: *2012 IEDM*. doi:[10.1109/IEDM.2012.6478989](https://doi.org/10.1109/IEDM.2012.6478989). IEEE, 2012.
- [66] Yang Li, Kui Yao, and Ganesh S Samudra. "Delay and power evaluation of negative capacitance ferroelectric MOSFET based on SPICE model." In:

- IEEE Trans. Electron Devices* 64.5 (2017). doi:[10.1109/TED.2017.2674020](https://doi.org/10.1109/TED.2017.2674020), pp. 2403–2408.
- [67] Milan Pešić, Christopher Künneth, Michael Hoffmann, Halid Mulaosmanovic, Stefan Müller, Evelyn T Breyer, Uwe Schroeder, Alfred Kersch, Thomas Mikolajick, and Stefan Slesazeck. “A computational study of hafnia-based ferroelectric memories: from ab initio via physical modeling to circuit models of ferroelectric device.” In: *J. Comput. Electron.* 16.4 (2017). doi:[10.1007/s10825-017-1053-0](https://doi.org/10.1007/s10825-017-1053-0), pp. 1236–1256.
- [68] Raghuram Tattamangalam Raman and Arvind Ajoy. *FERROELECTRIC NEGCAP HYBRID MEMS SPICE MODEL*. Available at <http://dx.doi.org/10.21227/9vpy-8658>. 2020.
- [69] Jaesung Jo, Asif Islam Khan, Karam Cho, Sangheon Oh, Sayeef Salahuddin, and Changhwan Shin. “Capacitance matching effects in negative capacitance field effect transistor.” In: *2016 IEEE Silicon Nanoelectronics Workshop (SNW)*. doi:[10.1109/SNW.2016.7578038](https://doi.org/10.1109/SNW.2016.7578038). IEEE. 2016, pp. 174–175.
- [70] Harshit Agarwal, Pragya Kushwaha, Yen-Kai Lin, Ming-Yen Kao, Yu-Hung Liao, Avirup Dasgupta, Sayeef Salahuddin, and Chenming Hu. “Proposal for capacitance matching in negative capacitance field-effect transistors.” In: *IEEE Electron Device Lett.* 40.3 (2019). doi:[10.1109/LED.2019.2891540](https://doi.org/10.1109/LED.2019.2891540), pp. 463–466.
- [71] Ali Saeidi, Farzan Jazaeri, Francesco Bellando, Igor Stolichnov, Christian C Enz, and Adrian M Ionescu. “Negative capacitance field effect transistors; capacitance matching and non-hysteretic operation.” In: *2017 ESSDERC*. doi:[10.1109/ESSDERC.2017.8066596](https://doi.org/10.1109/ESSDERC.2017.8066596). IEEE. 2017, pp. 78–81.
- [72] Manuel Domínguez, David López, David Molinero, and Joan Pons-Nin. “Dielectric charging control for electrostatic MEMS switches.” In: *Proc. SPIE*. Vol. 7679. doi:[10.1117/12.853177](https://doi.org/10.1117/12.853177). 2010, pp. 1–11.
- [73] Woo Young Choi, Taro Osabe, and Tsu-Jae King Liu. “Nano-Electro-Mechanical nonvolatile memory (NEMory) cell design and scaling.” In:

- IEEE Trans. Electron Devices* 55.12 (2008). doi:[10.1109/TED.2008.2006540](https://doi.org/10.1109/TED.2008.2006540), pp. 3482–3488.
- [74] Jason V Clark. “Calibrating Force and Displacement in the Face of Property Variation.” In: *MEMS and Nanotechnology*. Vol. 2. doi:[10.1007/978-1-4419-8825-6_10](https://doi.org/10.1007/978-1-4419-8825-6_10). Springer, 2011, pp. 67–74.
 - [75] S Shekhar, K J Vinoy, and G K Ananthasuresh. “Switching and release dynamics of an electrostatically actuated MEMS switch under the influence of squeeze-film damping.” In: *TechConnect Briefs* 2 (2012), pp. 625–628.
 - [76] Luis M Castaner, A Rodriguez, J Pons, and Stephan D Senturia. “Pull-in time–energy product of electrostatic actuators: comparison of experiments with simulation.” In: *Sens. Actuators, Phys. A* 83.1–3 (2000). doi:[10.1016/S0924-4247\(99\)00394-5](https://doi.org/10.1016/S0924-4247(99)00394-5), pp. 263–269.
 - [77] Luis M Castaner and Stephan D Senturia. “Speed-Energy Optimization of Electrostatic Actuators Based on Pull-in.” In: *J. Microelectromech. Syst.* 8.3 (1999). doi:[10.1109/84.788633](https://doi.org/10.1109/84.788633), pp. 290–298.
 - [78] A Fargas Marques, Ramon Costa Castelló, and A M Shkel. *Modelling the electrostatic actuation of MEMS: state of the art 2005*. Tech. rep. Universitat Politècnica de Catalunya, Barcelona, Spain, 2005.
 - [79] A Fargas Marques and A M Shkel. “On electrostatic actuation beyond snapping condition.” In: *Proc. IEEE SENSORS*. doi:[10.1109/ICSENS.2005.1597770](https://doi.org/10.1109/ICSENS.2005.1597770). IEEE, 2005, pp. 600–603.
 - [80] A Fargas Marques, Jasmina Casals-Terre, and A M Shkel. “Resonant pull-in condition in parallel-plate electrostatic actuators.” In: *J. Microelectromech. Syst.* 16.5 (2007). doi:[10.1109/JMEMS.2007.900893](https://doi.org/10.1109/JMEMS.2007.900893), pp. 1044–1053.
 - [81] A Fargas Marques. “Energy efficient control of electrostatically actuated MEMS.” PhD thesis. Universitat Politècnica de Catalunya, 2016.
 - [82] Mac Elwyn Van Valkenburg. “Network analysis.” In: 3rd ed. Prentice-Hall of India, 2004. Chap. 5, pp. 99–117.

- [83] Jasmina Casals-Terré, Marco A Llamas, David Girbau, Lluís Pradell, Antonio Lázaro, Flavio Giacomozi, and Sabrina Colpo. "Analytical energy model for the dynamic behavior of RF MEMS switches under increased actuation voltage." In: *J. Microelectromech. Syst.* 23.6 (2014). doi:[10.1109/JMEMS.2014.2314752](https://doi.org/10.1109/JMEMS.2014.2314752), pp. 1428–1439.
- [84] Somashekara Bhat and Enakshi Bhattacharya. "Parameter extraction from simple electrical measurements on surface micromachined cantilevers." In: *J. Micro/Nanolith. MEMS MOEMS* 6.4 (2007). doi:[10.1117/1.2794291](https://doi.org/10.1117/1.2794291), p. 043013.
- [85] Souvik Basu, Anil Prabhakar, and Enakshi Bhattacharya. "Estimation of stiction force from electrical and optical measurements on cantilever beams." In: *J. Microelectromech. Syst.* 16.5 (2007). doi:[10.1109/JMEMS.2007.893513](https://doi.org/10.1109/JMEMS.2007.893513), pp. 1254–1262.
- [86] Yuh-Chung Hu and Wei-Hsiang Tu. "Nonlinear and linearized algorithms for the Young's modulus extraction of thin films through the capacitance-voltage measurement of microstructures." In: *J. Appl. Phys.* 98.10 (2005). doi:[10.1063/1.2133898](https://doi.org/10.1063/1.2133898), p. 104504.
- [87] Peter M Osterberg and Stephen D Senturia. "M-TEST: a test chip for MEMS material property measurement using electrostatically actuated test structures." In: *J. Microelectromech. Syst.* 6.2 (1997). doi:[10.1109/84.585788](https://doi.org/10.1109/84.585788), pp. 107–118.
- [88] Jason Vaughn Clark, David Garmire, Matt Last, James Demmel, and Sanjay Govindjee. "Practical techniques for measuring MEMS properties." In: *Proc. NSTI Nanotechnology Conference and Trade Show*. 2004, pp. 402–405.
- [89] William Sharpe Jr. "Mechanical Properties of MEMS Materials." In: *The MEMS Handbook*. CRC press, 2001. Chap. 3, pp. 1–33.
- [90] Paolo Decuzzi, GP Demelio, G Pascazio, and V Zaza. "Bouncing dynamics of resistive microswitches with an adhesive tip." In: *J. Appl. Phys.* 100.2 (2006). doi:[10.1063/1.2214348](https://doi.org/10.1063/1.2214348), p. 024313.

- [91] S Chakraborty, A Bhattacharya, and TK Bhattacharyya. "Experimental analysis of pull-out voltage of electrostatically actuated microcantilever beam based on contact-stiction model." In: *Micro & Nano Lett.* 6.1 (2011). doi:[10.1049/mnl.2010.0125](https://doi.org/10.1049/mnl.2010.0125), pp. 43–47.
- [92] Frank W DelRio, Maarten P de Boer, James A Knapp, E David Reedy, Peggy J Clews, and Martin L Dunn. "The role of van der Waals forces in adhesion of micromachined surfaces." In: *Nature Mater.* 4.8 (2005). doi:[10.1038/nmat1431](https://doi.org/10.1038/nmat1431), pp. 629–634.
- [93] A Hariri, JW Zu, and R Ben Mrad. "Modeling of dry stiction in Micro Electro-Mechanical Systems (MEMS)." In: *J. Micromech. Microeng.* 16.7 (2006). doi:[10.1088/0960-1317/16/7/012](https://doi.org/10.1088/0960-1317/16/7/012), p. 1195.
- [94] Niels Tas, Tonny Sonnenberg, Henri Jansen, Rob Legtenberg, and Miko Elwenspoek. "Stiction in surface micromachining." In: *J. Micromech. Microeng.* 6.4 (1996). doi:[10.1088/0960-1317/6/4/005](https://doi.org/10.1088/0960-1317/6/4/005), p. 385.
- [95] Edward K Chan and Robert W Dutton. "Electrostatic micromechanical actuator with extended range of travel." In: *J. Microelectromech. Syst.* 9.3 (2000). doi:[10.1109/84.870058](https://doi.org/10.1109/84.870058), pp. 321–328.
- [96] Ben Rivlin and David Elata. "Design of nonlinear springs for attaining a linear response in gap-closing electrostatic actuators." In: *Int. J. Solids and Structures* 49.26 (2012). doi:[10.1016/j.ijsolstr.2012.08.014](https://doi.org/10.1016/j.ijsolstr.2012.08.014), pp. 3816–3822.
- [97] Elmer S Hung and Stephen D Senturia. "Extending the travel range of analog-tuned electrostatic actuators." In: *J. Microelectromech. Syst.* 8.4 (1999). doi:[10.1109/84.809065](https://doi.org/10.1109/84.809065), pp. 497–505.
- [98] Ankit Jain and Muhammad Ashraful Alam. "Extending and tuning the travel range of microelectromechanical actuators using electrically reconfigurable nano-structured electrodes." In: *J. Microelectromech. Syst.* 22.5 (2013). doi:[10.1109/JMEMS.2013.2266614](https://doi.org/10.1109/JMEMS.2013.2266614), pp. 1001–1003.

- [99] David M Burns and Victor M Bright. "Nonlinear flexures for stable deflection of an electrostatically actuated micromirror." In: *Microelectronic Structures and MEMS for Opt. Process. III*. Vol. 3226. doi:[10.1117/12.284560](https://doi.org/10.1117/12.284560). Int. Soc. Optics and Photonics. 1997, pp. 125–136.
- [100] Xiaojian Xiang, Xuhan Dai, Kai Wang, Zhuoqing Yang, Yunna Sun, and Guifu Ding. "A customized nonlinear micro-flexure for extending the stable travel range of MEMS electrostatic actuator." In: *J. Microelectromech. Syst.* 28.2 (2019). doi:[10.1109/JMEMS.2019.2894669](https://doi.org/10.1109/JMEMS.2019.2894669), pp. 199–208.
- [101] Slava Krylov, Bojan R Ilic, David Schreiber, Shimon Seretensky, and Harold Craighead. "The pull-in behavior of electrostatically actuated bistable microstructures." In: *J. Micromech. Microeng.* 18.5 (2008). doi:[10.1088/0960-1317/18/5/055026](https://doi.org/10.1088/0960-1317/18/5/055026), p. 055026.
- [102] David Elata. *Modeling the Electromechanical Response of Electrostatic Actuators*. Vol. 4. Springer Science & Business Media, 2007.
- [103] Jasmina Casals-Terre, Andreu Fargas-Marques, and Andrei M Shkel. "Snap-action bistable micromechanisms actuated by nonlinear resonance." In: *J. Microelectromech. Syst.* 17.5 (2008). doi:[10.1109/JMEMS.2008.2003054](https://doi.org/10.1109/JMEMS.2008.2003054), pp. 1082–1093.
- [104] B Charlot, W Sun, K Yamashita, H Fujita, and H Toshiyoshi. "Bistable nanowire for micromechanical memory." In: *J. Micromech. Microeng.* 18.4 (2008). doi:[10.1088/0960-1317/18/4/045005](https://doi.org/10.1088/0960-1317/18/4/045005), p. 045005.
- [105] Ilya V Uvarov, Victor V Naumov, Olga M Koroleva, Elena I Vaganova, and Ildar I Amirov. "A low actuation voltage bistable MEMS switch: design, fabrication and preliminary testing." In: *Int. Conf. Micro-and Nano-Electronics*. Vol. 10224. doi:[10.1117/12.2266439](https://doi.org/10.1117/12.2266439). Int. Soc. Optics and Photonics. 2016, 102241A.
- [106] Hassen M Ouakad and Mohammad I Younis. "On using the dynamic snap-through motion of MEMS initially curved microbeams for filtering applications." In: *J. Sound and Vibration* 333.2 (2014). doi:[10.1016/j.jsv.2013.09.024](https://doi.org/10.1016/j.jsv.2013.09.024), pp. 555–568.

- [107] EK Chan, EC Kan, RW Dutton, and PM Pinsky. "Nonlinear dynamic modeling of micromachined microwave switches." In: *IEEE MTT-S Int. Microwave Symposium Digest*. Vol. 3. doi:[10.1109/MWSYM.1997.596617](https://doi.org/10.1109/MWSYM.1997.596617). IEEE. 1997, pp. 1511–1514.
- [108] Bruno Borovic, Cai Hong, Ai Qun Liu, Lihua Xie, and Frank L Lewis. "Control of a MEMS optical switch." In: *IEEE Conf. Decision and Control (CDC)*. Vol. 3. doi:[10.1109/CDC.2004.1428930](https://doi.org/10.1109/CDC.2004.1428930). IEEE. 2004, pp. 3039–3044.
- [109] Jason S Milne, John M Dell, Adrian J Keating, and Lorenzo Faraone. "Widely tunable MEMS-based Fabry–Perot filter." In: *J. Microelectromech. Syst.* 18.4 (2009). doi:[10.1109/JMEMS.2009.2024793](https://doi.org/10.1109/JMEMS.2009.2024793), pp. 905–913.
- [110] Chris Cortopassi and Ongi Englander. "Nonlinear springs for increasing the maximum stable deflection of MEMS electrostatic gap closing actuators." In: *University of Berkeley, Berkeley* (2010). URL: <http://www-bsac.eecs.berkeley.edu/~pister/245/project/CortopassiEnglander.pdf>.
- [111] Mohamed Amri, Philippe Basset, Dimitri Galayko, Francesco Cottone, Einar Halvorsen, S Duy Nguyen, Fehmi Najar, and Tarik Bourouina. "Stiffness control of a nonlinear mechanical folded beam for wideband vibration energy harvesters." In: *Technisches Messen* 85.9 (2018). doi:[10.1515/teme-2017-0087](https://doi.org/10.1515/teme-2017-0087), pp. 553–564.
- [112] Shaikhmdrubayiat Rubayiat Tousif. "MEMS Wideband Energy Harvesting Using Nonlinear Springs and Mechanical Stoppers." PhD thesis. The University of Texas at Arlington, 2019. URL: <https://rc.library.uta.edu/uta-ir/handle/10106/28154>.
- [113] Sebastien Boisseau, Ghislain Despesse, and Bouhadjar Ahmed Seddik. "Nonlinear H-shaped springs to improve efficiency of vibration energy harvesters." In: *J. Appl. Mechanics* 80.6 (2013). doi:[10.1115/1.4023961](https://doi.org/10.1115/1.4023961).
- [114] Xuhan Dai, Xiaodan Miao, Linghe Sui, Hailin Zhou, Xiaolin Zhao, and Guifu Ding. "Tuning of nonlinear vibration via topology variation and its application in energy harvesting." In: *Appl. Phys. Lett.* 100.3 (2012). doi:[10.1063/1.3676661](https://doi.org/10.1063/1.3676661), p. 031902.

- [115] Arman Hajati. "Ultra Wide-Bandwidth Micro Energy Harvester." PhD thesis. Massachusetts Institute of Technology, 2010. URL: <https://dspace.mit.edu/handle/1721.1/63072>.
- [116] Christine Vehar Jutte and Sridhar Kota. "Design of nonlinear springs for prescribed load-displacement functions." In: *J. Mech. Des.* 130 (2008). doi:[10.1115/1.2936928](https://doi.org/10.1115/1.2936928).
- [117] J Gomez, S Dutta, K Ni, JA Smith, B Grisafe, A Khan, and S Datta. "Hysteresis-free negative capacitance in the multi-domain scenario for logic applications." In: *2019 IEEE IEDM*. doi:[10.1109/IEDM19573.2019.8993638](https://doi.org/10.1109/IEDM19573.2019.8993638). IEEE. 2019.
- [118] Jorge Tomás Gómez Mir. "Functional oxide-based electronics for logic, memory, and RF applications." PhD thesis. Pontificia Universidad Católica de Chile and University of Notre Dame, 2021. URL: <https://repositorio.uc.cl/xmlui/handle/11534/62908>.
- [119] Carlotta Gastaldi, Matteo Cavalieri, Ali Saeidi, Eamon O'Connor, Francesco Bellando, Igor Stolichnov, and Adrian M Ionescu. "Negative Capacitance in HfO₂ Gate Stack Structures With and Without Metal Interlayer." In: *IEEE Trans. Electron Devices* 69.5 (2022). doi:[10.1109/TED.2022.3157579](https://doi.org/10.1109/TED.2022.3157579), pp. 2680–2685.
- [120] Zhi Cheng Yuan, Shahriar Rizwan, Michael Wong, Kyle Holland, Sam Anderson, Terence B Hook, Diego Kienle, Serag Gadelrab, Prasad S Gundem, and Mani Vaidyanathan. "Switching-speed limitations of ferroelectric negative-capacitance FETs." In: *IEEE Trans. Electron Devices* 63.10 (2016). doi:[10.1109/TED.2016.2602209](https://doi.org/10.1109/TED.2016.2602209), pp. 4046–4052.